Plasma Channel and Z-Pinch Dynamics for Heavy Ion Transport

by

David Miguel Ponce-Márquez

B.S. (University of California, Berkeley) 1994
M.A. (University of California, Berkeley) 1998

A dissertation submitted in partial satisfaction of the
requirements for the degree of
Doctor of Philosophy

in

Physics

in the

GRADUATE DIVISION
of the
UNIVERSITY of CALIFORNIA at BERKELEY

Committee in charge:

Dr. Simon S. Yu, Co-Chair
Professor Roger W. Falcone, Co-Chair
Professor Jonathan Wurtele
Professor Per Peterson

Fall 2002

The dissertation of David Miguel Ponce-Márquez is approved:

_____

Co-Chair   Date

_____

Co-Chair   Date

_____

Date

_____

Date

University of California at Berkeley

Fall 2002

Plasma Channel and Z-Pinch Dynamics for Heavy Ion Transport

Copyright Fall 2002

by

David Miguel Ponce-Márquez

Abstract

Plasma Channel and Z-Pinch Dynamics for Heavy Ion Transport

by

David Miguel Ponce-Márquez

Doctor of Philosophy in Physics

University of California at Berkeley

Dr. Simon S. Yu, Co-Chair

Professor Roger W. Falcone, Co-Chair

A self stabilized, free standing, z-pinch plasma channel has been proposed to deliver the high intensity heavy ion beam from the end of a driver to the fuel target in a heavy ion inertial fusion power plant. The z-pinch relaxes emittance and energy spread requirements requiring a lower cost driver. A z-pinch transport would reduce the number of beam entry port holes to the target chamber from over a hundred to four as compared to neutralized ballistic focusing thus reducing the driver hardware exposure to neutron flux. Experiments where a double pulse discharge technique is used, z-pinch plasma channels with enhanced stability are achieved. Typical parameters are $7\,kV$ pre-pulse discharge and $30\,kV$ main bank discharge with $50\,kA$ of channel current in a $7\,torr$ background gas atmosphere. This work is an experimental study of these plasma channels examining the relevant physics necessary to understand and model such plasmas. Laser diagnostics measured the dynamical properties

of neutrals and plasma. Schlieren and phase contrast techniques probe the pre-pulse gas dynamics and infrared interferometry and faraday effect polarimetry are used on the z-pinch to study its electron density and current distribution. Stability and repeatability of the z-pinch depend on the initial conditions set by the pre-pulse. Results show that the z-pinch channel is wall stabilized by an on-axis gas density depression created by the pre-pulse through hydrodynamic expansion where the ratio of the initial gas density to the final gas density is $> 10/1$. The low on-axis density favors avalanching along the desired path for the main bank discharge. Pinch time is around $2\,\mu$s from the main bank discharge initiation with a FWHM of $\approx 2\,$cm. Results also show that typical main bank discharge plasma densities reach $10^{17}\,\mathrm{cm}^{-3}$ peak on axis for a $30\,$kV, $7\,$torr gas nitrogen discharge. Current rise time is limited by the circuit-channel inductance with the highest contribution to the impedance due to the plasma. There is no direct evidence of surface currents due to high frequency skin effects and magnetic field experiments indicate that $> 70\%$ of the current carried by the channel is enclosed within FWHM of the channel. Code-experiment benchmark comparisons show that simulations capture the main mechanisms of the channel evolution, but complete atomic models need to be incorporated.

Dr. Simon S. Yu
Dissertation Committee Co-Chair

Professor Roger W. Falcone
Dissertation Committee Co-Chair

To the loving memory of my father,

José Ponce Gómez,

your integrity drew the path for me to follow,

and to my mother,

Mercedes Márquez,

your fortitude, tenacity, and infinite love led us through very though times.

Contents

List of Figures

List of Tables

Acknowledgements

I have been very fortunate to meet countless people throughout my academic life that have inspired me, challenged me, supported me, antagonized me, enlightened me, but most important, believed in me. I am very grateful to all of them. I am full of joy to have reached this milestone in my life and would like to share this joy. To all of the believers, this work is the product of all of you. Thank you!

I wish that I could properly acknowledge everyone, but I realize that the probability is high that I will not find the proper words or simply that I will neglect someone. I deeply apologize for such omissions, but to those that I overlooked, my gratitude is sincerely felt toward you.

To my family:

I thank my children, Diana and David Michael, from which I drew my main inspiration. Their love and pride for me always reminded me of the enormous obligation and responsibility that I owed to them. I hope that my modest accomplishments serve as inspiration and a guide to them. Dreams do come true if you believe in them and you persevere on their quest.

I thank my wife Carmen for all of her patience through all these years. Taking care of the children and always worrying for their welfare wasn't always easy. You showed me that disagreement is not always a bad thing and that in life there are always higher reasons for us to work together.

I can't thank enough the invisible helping hand of my mother and brothers. Mercedes, although I never showed it, you have my deepest love, respect, and admiration. You

have been the rock upon which I have found strength. José, your kindness and unselfishness will always be appreciated. Thanks. Enrique, I want to thank you for being our mother's companion during hard times. I hope and wish that you remember that you always will have a especial place in our hearts.

I thank Ramona Alcalá, for all of her trust and good wishes. God bless you!

I thank Alma Rosa Morado for her unconditional friendship and help and for being the sister that I never had.

I give thanks to Alicia Morado and Manfred Young for opening the door of their home and their heart to me and my family.

I give thanks to Jesse Gaviño for his continued interest in science and always finding a challenging question to confront me with. May your curiosity never dwindle.

I thank Lizzeth Fermin and Liliana Gaviño for making the kids feel at home while away from home. Knowing that Michael and Diana were in good company during those long summers kept my mind at ease.

To my committee:

I thank my dissertation committee for their valuable support and advice.

I want to extend my gratitude to Simon Yu for taking me under his tutelage while displaying admirable conviction and believe on the plasma channel project. He made a simple study into a dissertation project. I am grateful for his advice, guidance, and all of his patience. He showed me that accomplishments are done through careful planing, hard work, and, most of all, discipline.

I thank Roger Falcone for all of the good advice he provided me. He always kept

his door open, even in his busiest time as department chair. He listen to all his students with great attention, even if the consultation was physics unrelated. As a physics adviser, you were a superb one. Roger, your mentorship is deeply appreciated.

I thank Jonathan Wurtele and Per Peterson for accepting and taking the time of being in my dissertation committee. Their advice and feedback will always be appreciated.

To my *Alma Mater*:

Thanks to the UC Berkeley physics department. They have been an extended family and the facilities provided for a home away from home.

I thank my mentor Marjorie Shapiro for being the champion of my cause and a voice of encouragement. She always lent ears to listen and always showed me that there was hope even in the darkest moments.

I thank Professor J.D. Jackson for all of his teachings. The entering physics class of 1994 was very fortunate to have him as our electricity and magnetism course instructor.

I thank Professor E. Commins for his superb and impeccable teachings where I learned the beauty and elegance of physics.

I thank Professor A. Portis for finding a physicist where there was none. I now see how curiosity, inquisition, and non-conformity are the trades of a good scientist.

I thank Professor B. Price for his warm welcome to the department program and his good wishes. I appreciate your advice on not to underestimate the difficulty of the road ahead and for making possible and available all of the student life support systems needed to succeed.

I thank Professor D. Budker and Professor Daniel Chemla for providing me with

the valuable tools needed in optics research. The insight that can't be found in books can only be learned from experts such as you.

I thank Dr. Colette Patt for all of her help and advice. She was the instrument through which many students have grown and flourished in science, students that otherwise would not. I am one of those students.

I thank Dr. Carla Trujillo for persuading me to follow my true dream and not conform with the practical outlet.

I thank Antoinette Torres for making sure that I knew that I had a fighting chance of attending and making it through, in my opinion, the best school on earth.

I thank Dr. Matteo Genna, teacher extraordinaire. Prelims would have been impossible without his help.

I am for ever grateful to Anne Takizawa, Donna Sakima, and Claudia Trujillo for all of their help. They are the lifeline to all physics graduate and undergraduate students. Your service to the student community is invaluable and is very much appreciated.

To the LBNL staff:

I thank Dr. T. Fessenden and Dr. M. Vella for showing me the intricate ropes of running the channel experiment. I also thank them for their practical views on research, physics, and life.

I thank the Heavy Ion Fusion group staff for all the support provided. Thanks are due to Dr. R. Bangerter, Dr. E. Lee, Dr. J. Barnard, Dr. C. Celata, S. Buckley, L. Heimbucher, and P. MontannaBronte. I will miss you all.

I thank Christoph Niemann for his friendship, most valuable discussions, and opin-

ions on physics and spectroscopy, and for introducing me to the world of RedHat. May the force of Linux be with you.

I thank Kevin Vandersloot and Lance Kim for their valuable work on CYCLOPS. The theoretical comparisons on this manuscript wouldn't had happen without them.

I thank Michiel DeHoon, Edwin Chacon, Steve MacLaren, Scott Armel-Funkhouser, and Caron Jantzen for the discussions and support as graduate student colleagues and friends. The building 54 seminars will be missed.

I can not thank enough Dr. Tetsu Tokunaga. His modesty and humble self have set a great example for me to follow. The passion he displays on his work and dedication, yet his desire to find scientific truth and not personal fame, makes him a hero in my book.

I thank Dr. Anthony Young for making possible for me to have my first working experience with plasmas, lasers and introducing me to all of the endeavors of scientific work.

I thank Swapan Chattopadayay, Wim Leemans, and Joy Kono for the opportunity to participate in the Center for Beam Physics. The experience that I gained in the center has proven invaluable.

I thank Jim Daugherty, Leon "Archie" Archambault, Ralph Hipple, Bill Giorso and all of the people in building 58 for all of their help with the hardware nitty-gritty. Be assured that science would not exist as we know it today without people like you.

To my friends:

I thank David Locke, Jeff and Sonnie Moehlis, Douglas Finkbeiner, Roy Therrien, Kevin Mitchell, Eric Chang, Richa Govil, Susan Wheeler, Carl Schroeder, and Dan Pickard for sharing, along with me, the Berkeley experience. Many sleepless nights came and went

pondering about homework problems, running an experiment, just talking about physics, or inventing some new game to have an excuse to delay the suffering over the long homework sets. Such conditions forged lifetime friendships.

I thank Fernando Estrada-Garcia and Antonio "finito" Castillo for their early teachings and encouragement.

I thank all of my old high school friends, especially, Antonio Hernandez-Castillo, Luis Benito Ruiz Bogarin, Jose Alatorre, Rebeca Montero, Carmen Galvan, Marco Herrera, Manuel Ley, Mijangos Salgado, and the rest of the gang. I remember fondly all of the good times that we had.

I thank Alberto Cardenas for all of his help on a especially critical time. Although our friendship was brief, it was one of the sincerest.

Writing these acknowledgment lines have made me think and remember through most of my life. I realize that I have gone through my share of good and bad times. It has been exciting to say the least. I look forward to serve, and as every good scientist, wish to make this world a better place to live, not just for us, but for our children and their children. Thanks to all of you I can make my small contribution. I'll strive to honor all of you with the fruit of my work, since, after all, me being at this juncture in life is a result of all of your combined efforts and best wishes.

David M. Ponce

Berkeley, California

June, 2002

Chapter 1

Introduction

1.1 Motivation

This work presents an experimental study of z-pinch plasma channels in the parameter regime suitable for transport of intense beams of charged particles. Typical discharge currents are in the order of $\sim 50\,\text{kA}$. These channels have a direct application to the transport of heavy ion beams used for inertial confinement fusion (ICF) energy production. In particular, these channels would serve as an integral part of the final focus system that delivers the ICF ion beams to the fusion target.

The main line approach of studies in HIF final focus and transport assume ballistic neutralized focusing where the beam passes through a set of focusing magnetic quadrupole lenses followed by a drift section where the beam is neutralized by a plasma. Neutralized ballistic focusing is very sensitive to beam current and beam shape, so a tight parameter space dictates the accelerator design [20]. Plasma channel focus and transport relaxes these requirements and offers additional benefits for target chamber beam transport [72].

Emittance and beam energy spread requirements imposed on the driver accelerator are significantly relaxed. The equilibrium solution to equation 1.15 in the adiabatic approximation is [82]

$$\frac{\varepsilon}{a} = ka = 72 \left[\left(\frac{Z}{64}\right) \left(\frac{I}{50}\right) \left(\frac{0.2}{\beta}\right) \left(\frac{200}{A}\right) \right]^{1/2} \text{mr} \qquad (1.1)$$

where ε is the normalized edge emittance, Z the atomic number refered to highly stripped lead ions, I the channel current in kA refered to a 50 kA particle current, $\beta = v/c$, and A the atomic mass of the ion species refered to lead. A 50 kA discharge channel will accept a 72π mm-mr beam emittance for a lead ion beam of comparable particle current. This emittance is much larger than the typical emittance values needed for neutralized ballistic focusing. As we will see later in this chapter, in contrast, once the beam is in the plasma channel the beam is focused and delivered to the target maintaining the channel entry beam spot size.

Additional benefits of the plasma channel include increased final focus quadrupole and plasma netralizing drift hardware to target standoff distance and the possibility to reduce the number and size of the FLiBe target pocket openings needed for target illumination entrance. Neutralized ballistic focusing will require over a hundred of port holes with an approximate diameter of 10 cm as compared to only four port holes of about 6 cm in the alternate plasma channel scheme. This will reduce significantly the exposure and damage of the superconducting focusing magnets and other accelerator hardware to the energetic neutron flux produce by the fusion reaction.

While the plasma channel beam transport approach offers significant benefits, this technique is viewed as an alternate approach that has a larger number of unknowns that

need to be investigated before it can be considered as a viable solution to the transport problem. First of all, consistent channel production needs to be demonstrated and explained. Second, MHD instabilities need to be mitigated at least to the point, timewise, where the channel allows for beam transport. Its needed to be understood why and how this channel stabilization occurs. Lastly, it needs to be determined and understood all of the channel-beam interactions.

In this study I will examine the results of laser diagnostic experiments performed on these z-pinch plasma channels produced at LBNL. The diagnostics will focus on the dynamics of the gas and plasma during the channel's evolution. Since stable and reproducible channels have been empirically demonstrated and are easily produced, I will attempt to de-mystify them and understand the mechanisms behind them. I will also show how these results can be used to validate computer codes used to simulate the channels. The part that I will not address are the beam-channel interactions.

Although these plasma channels have a direct application to fusion energy research, the approach of this work is to understand the underlying basic physics of these channels and cast it in such a way that it serves as a base to the development to other possible applications outside ICF.

1.2   Brief Review of Fusion Research and its Direction

The production of electrical energy through the harnessing of the power produced in a nuclear fusion reaction has been one of the most difficult scientific and technological endeavors that human kind has undertaken. Conquering such a goal will not only provide

with a safe, clean, unlimited source of energy, but it will also help implement policies toward the curtailing of green house gases in the atmosphere as well as cutting down on other non-desirable environmental effects associated with conventional energy sources. Although the rewards are big, the road to success has many, too many scientific and technological pitfalls. Early on it was realized that light nuclei had the potential to fuse together to form a heavier nucleus an release energy during the process. Figure 1.1 shows a typical tritium-deuterium reaction. The one obstacle that the fusion reaction of light nuclei has to overcome is the Coulomb repulsion of the positively charged nuclei. Fusion energy does occur readily in nature as it does in stars, in particular our sun, where gravity overcomes the electrostatic repulsive forces and confines the reacting plasma for a long time, thus allowing the light nuclei to fuse together. Unfortunately, as far as fusion is concerned, gravity is not of much help here on Earth. Hence, if we seek to produce controlled energy production through fusion, we need to develop schemes to confine the light nuclei as gravity does in the large celestial bodies.

To produce fusion energy from a suitable plasma, one must satisfy as a minimum Lawson's criterion [34]. Lawson's criterion is based on the premise that the total useful energy contained within a reacting plasma has to be greater or equal to the net energy loss during the plasma confinement time. This energy loss resides in the thermal energy of the plasma and free-free bremsstrahlung radiation. Lawson expressed this idea in terms of the product $n\tau$:

$$n\tau \geq \frac{3k_B T}{\left[\frac{\eta}{1-\eta} \frac{\gamma \langle \sigma v \rangle Q}{4} - \alpha T^{1/2}\right]} \tag{1.2}$$

where n is particle number density, τ the confinement time, η the efficiency of energy
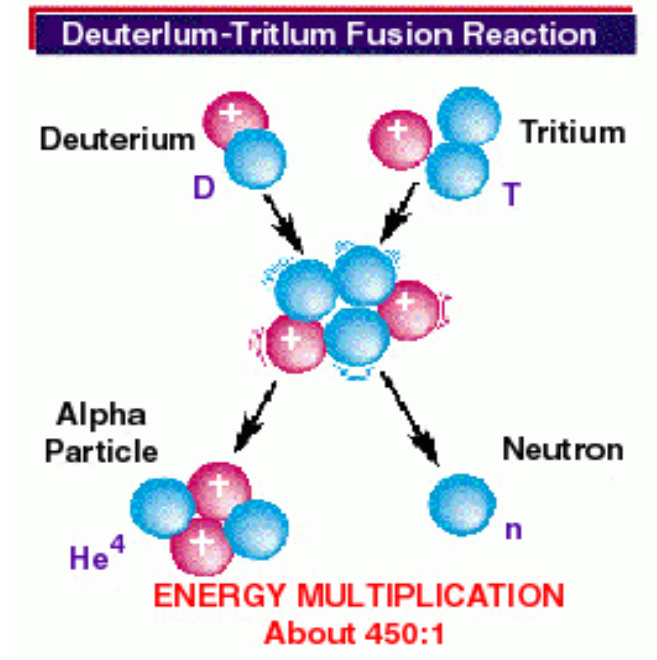
Figure 1.1: Diagram illustrating a tritium-deuterium reaction. This particular reaction has a net energy release of 17.6 MeV.

production through fusion, γ an integer factor determined by the reactants, $\langle \sigma v \rangle$ the nuclear reaction rate, Q the energy released per reaction, α a lumped bremsstrahlung coefficient, T the plasma temperature, and k_B the Boltzmann constant. From equation (1.2) one can see that to achieve fusion one can have a reacting plasma with a moderate density confined for a long time or a plasma with a very high density confined for a very short time, provided that one fixes the reacting temperature and the reaction type.

Two major techniques have been proposed to satisfy Lawson's criterion for the purposes of commercial energy production: magnetic confinement and inertial confinement [24]. In the first approach, magnetic confinement, or magnetic fusion energy (MFE), one relies on large machines to produce a strong magnetic field to confine a moderately dense, but very hot plasma for a relatively long time. When one speaks of magnetic fusion energy

power plants, one immediately pictures large Tokamaks such as the one in the Princeton Plasma Laboratory in New Jersey or the DIII-D at General Atomics in San Diego, California. Figure 1.2 illustrates the DIII-D concept. MFE is the oldest area of fusion research, dating back to the early 1950's, and has accounted until recently for the largest share of funding extended by the U.S. Department of Energy. It is until now, with MFE not being able to deliver results within critical deadlines, that other forms of fusion research are being considered more seriously.

In inertial confinement, or inertial confinement fusion (ICF), the fusion reaction is achieved by compressing a fuel target, via very high intensity laser or ion beams, to very high densities over those of solid hydrogen in a very short confinement time. From the practical point of view, the ICF concept has been demonstrated through the detonation of modern thermonuclear weapons. The challenge lies in controlling the energy release in a useful and constructive form. An example of research of ICF using laser to produce the target implosion is the National Ignition Facility (NIF) located in the Lawrence Livermore National Laboratory (LLNL). An schematic of NIF and the old NOVA target chamber are shown in figure 1.3. Fusion energy production using ion beams requires the following infrastructure: ion sources and injectors, ion accelerator driver, combining and focusing elements, target chamber, and target factory [6]. Several point designs for an HIF power plant have been put forward by international scientific committees. The infrastructure and components of an ICF power plant are discussed in detail in such reports. Such designs include HIBALL II, and HYLIFE II [42]. Figure 1.4 show the chamber concept of HYLIFE II.

These designs provide the basic working parameter values that the different compo-

a.– Tokamak conceptual schematic
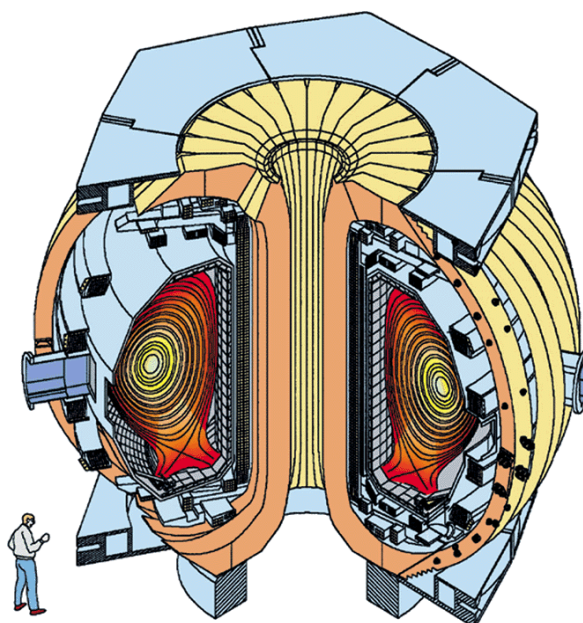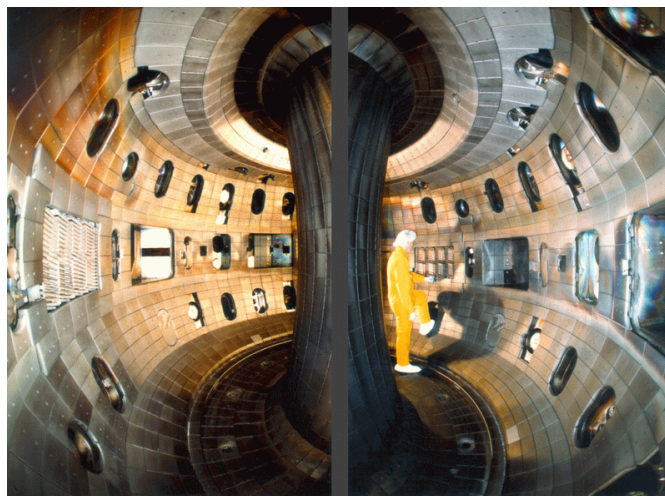
b.– Inside the DIII–D tokamak

Figure 1.2: Diagram illustrating: a) Tokamak concept, b) Inside the DIII-D tokamak (courtesy of General Atomics, San Diego, California).
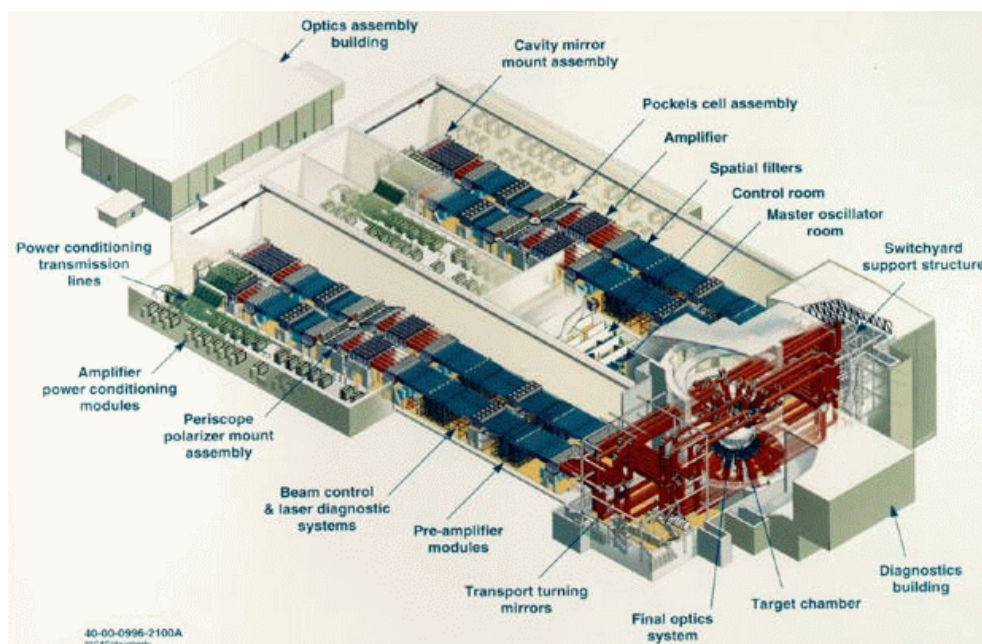
Arquitectural Concept of the National Ignition Facility (NIF, LLNL)
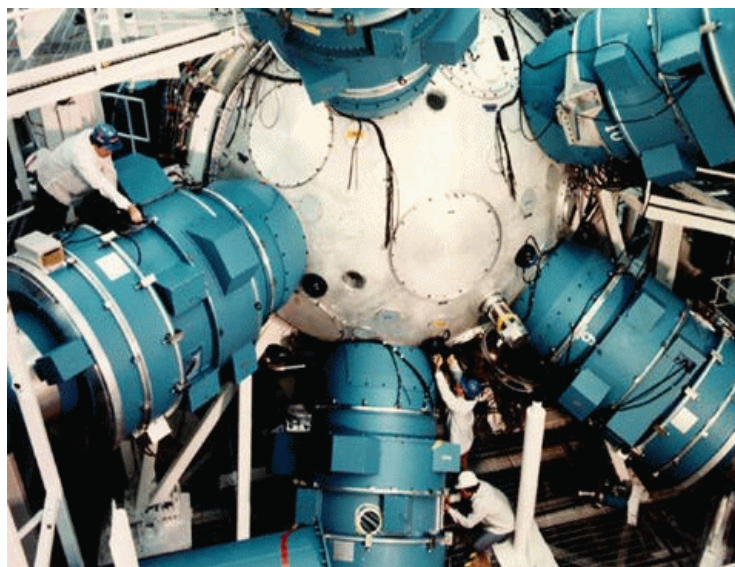
Ignition Chamber of NOVA (precursor to NIF, LLNL)

Figure 1.3: Diagram illustrating laser ICF: Top, NIF concept; bottom, NOVA target chamber (courtesy of LLNL).
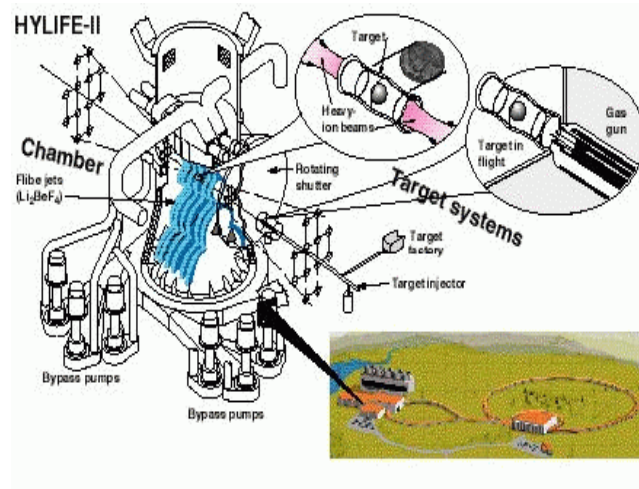
Schematic showing HYLIFE II Chamber with heavy ion beam entry port
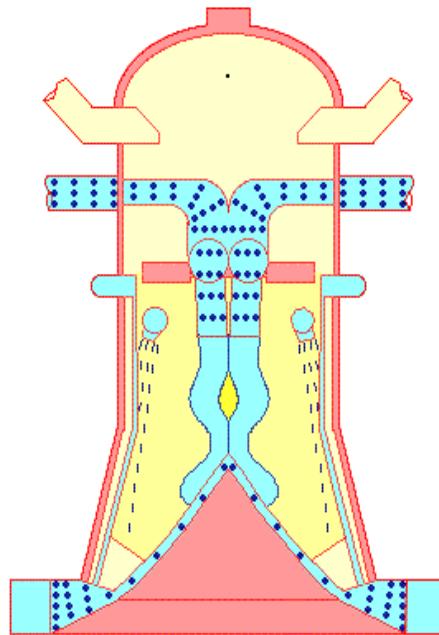
Cartoon detail of chamber showing oscillating FLiBe jets used to enclose target

Figure 1.4: Diagram illustrating target chamber concepts in HYLIFE II: Top, ion beam passage into target chamber under the ballistic focus scheme; bottom, molten FLiBe pocket enclosing target (courtesy of UC Berkeley).

nents of the system should deliver, such as beam energy, beam current, number of beams, and beam emmitance, just to mention a few. A conceptual picture of a power plant is shown in figure 1.7a. Within the combining and focusing elements is the final focus and beam chamber transport section. Presently, as of the writing of this work, there are two major techniques for final focus and chamber transport: ballistic focusing [39] and plasma focusing [82]. The main research emphasis within HIF has gone to ballistic focusing and transport, and although it is the simplest approach, it presents the difficulty of not meeting final beam spot size as well as the stringent transverse emmitance requirements that high yield target designs impose without using some sort of plasma space-charge neutralization technique or increasing the beam energy through a larger accelerator driver [39] [7] [4]. The alternative technique is to use and rely on a plasma's electromagnetic properties to transport the ion beam. As far as plasma transport schemes go, one can break down further the different plasma techniques such as self-pinch [80] [54] and pre-formed channels [9] [73] [82]. This work studies the pre-formed z-pinch plasma channel. Figure 1.7b shows a detail concept of a pre-formed plasma channel beam final focus and transport. The idea is to create a plasma z-pinch column between the end of the accelerator's final focus magnets and the fusion target. The beam will be transported via the plasma's magnetic field. An immediate advantage that the plasma channel transport offers is the ease of multi-beam combining, thus only having to deal with transporting two beams to the target. On the down side, the plasma channel technique can only accommodate indirect drive targets, this is, a target in which the fuel is encased inside a holhraum. Figure 1.5 show the conceptual details and size of the hohlraum target. Extensive research has been done at the Lawrence

Livermore National Laboratory (LLNL) on the target physics. This research has led to many target designs. Figure 1.6 show a cartoon of the hybrid target concept. The hybrid target is an optimized design that incorporates many features of other target designs that is suitable to be used in large spot size beam machines. I will talk more about the hybrid target in the next section.

1.3 Basic Physics of a Z-Pinch and its Application to HIF

The transport and focusing of a charged particle beam relies in counteracting the transverse beam expansion caused by the particle's transverse thermal energy and the space-charge repulsive forces. Traditional accelerator technology utilizes magnetic and/or electrostatic elements, such as quadrupoles set in a periodic arrangement called a lattice to focus and transport the charged particle beam to its target [17]. With the advent of new challenges, such as much higher energies in collider accelerators [26] or, in the case of HIF, the use of traditional focusing magnets close to the target chamber where exposure of accelerator components to the neutron flux released during reaction compromises the final focus hardware, redirected attention has resulted in a closer look at beam transport and focusing using plasmas.

For the particular application of ion beam transport using a plasma z-pinch, one would rely on the well known MHD equilibrium condition of the z-pinch, equations (1.3) and (1.4), for the establishment of the confining azimuthal magnetic fields along a cylindrical plasma column with a diameter of approximately 1 cm [32] [44]:

$$\sum F_r = -\nabla P + \frac{1}{c} \vec{J} \times \vec{B} = 0 \tag{1.3}$$
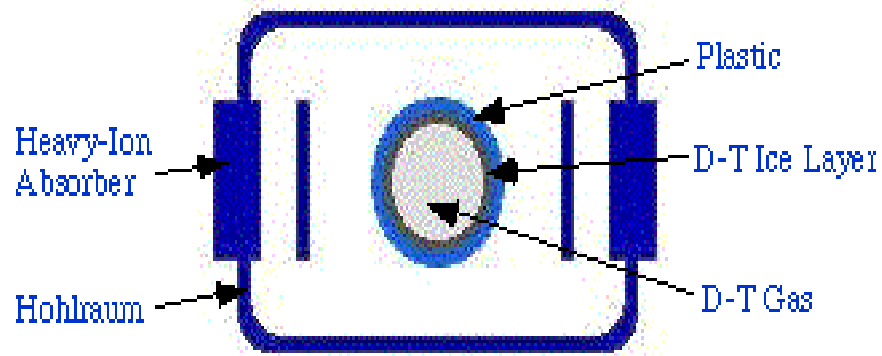
Heavy Ion Hohlraum Conceptualization
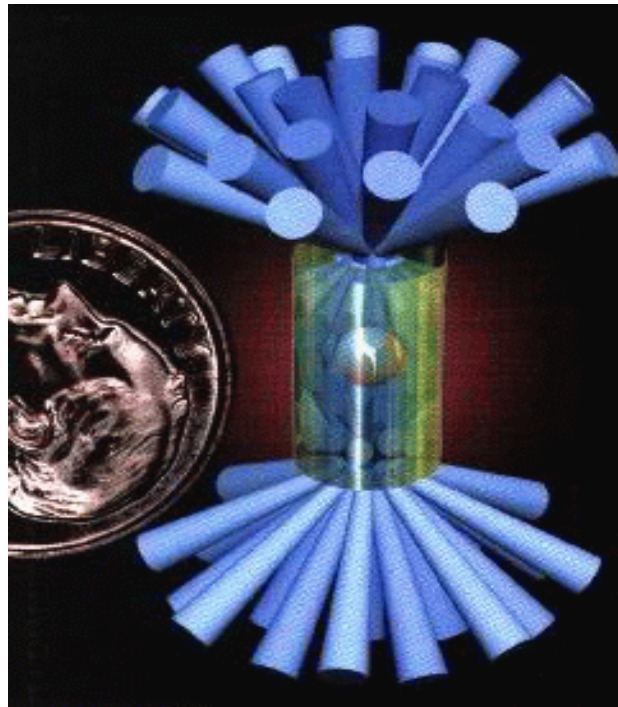
Holhraum size and Illumination Region (artist rendition)

Figure 1.5: Diagram illustrating ICF hohlraum concept and size: Top, hohlraum components; bottom, hohlraum size and beam illumination incidence (courtesy of LLNL).
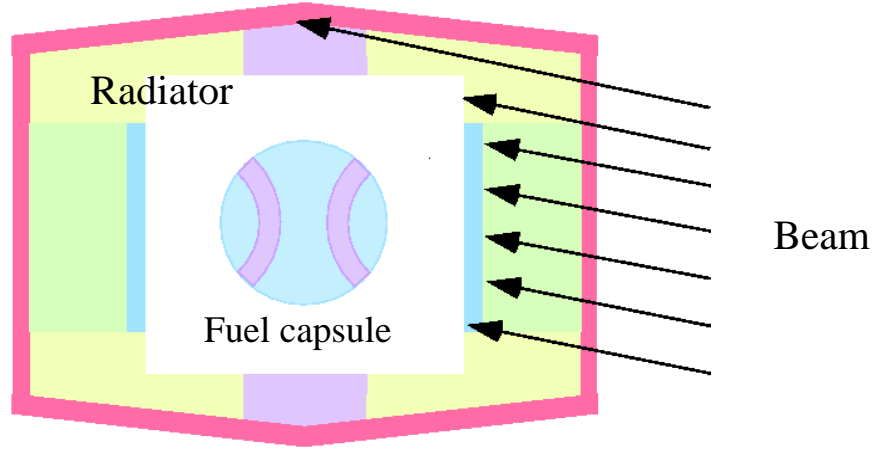
Figure 1.6: Diagram illustrating ICF hybrid target hohlraum concept (courtesy of LLNL).

$$\nabla \left[P + \frac{B^2}{8\pi} \right] = 0 \tag{1.4}$$

An illustration of this technique is shown in figure 1.8. One can create a plasma column with a channel current comparable to the beam current to be transported. The channel's pinch diameter and pinch time would be dependent on the gas species within the chamber enclosing the channel, the gas fill pressure, and the channel's discharge current. This current would be limited by the overall pulser power supply and channel inductance. In a typical design, one would expect to transport a $50\,\mathrm{kA}$ beam with a pulse length of about $8\,\mathrm{ns}$ [42] [82].

The plasma channel conductivity is a key factor determining the feasibility of this technique. In order to effectively transport a charged particle beam, the plasma channel

**An Inertial Fusion Power Plant
Based on a Heavy-Ion Induction Linear Accelerator**
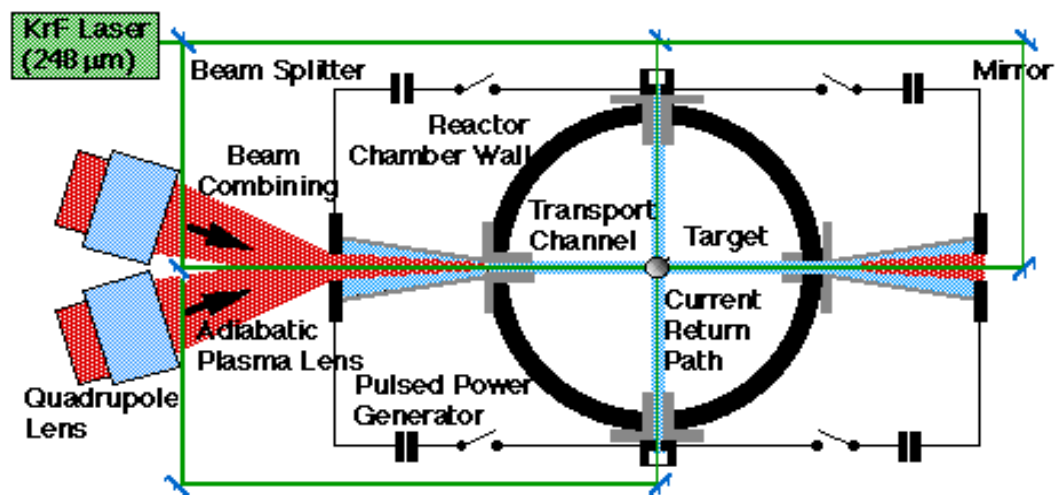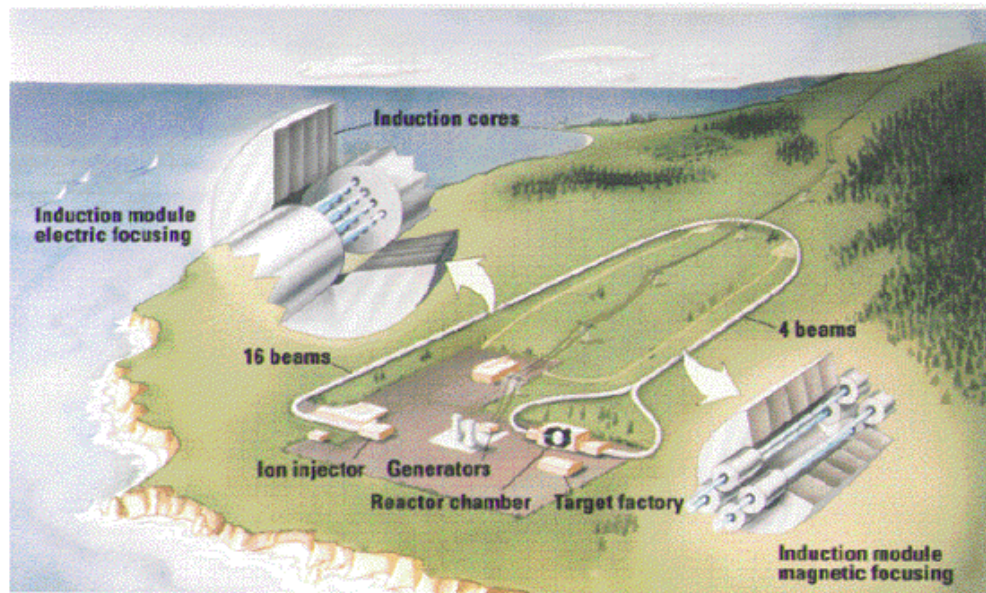
Figure 1.7: Diagram illustrating: a) An HIF power plant concept, b) Conceptual detail of the target chamber utilizing pre-formed plasma channels for beam transport.

Ion Beam

Ion Beam

Plasma Z- pinch

Ion Beam

B(θ)- field
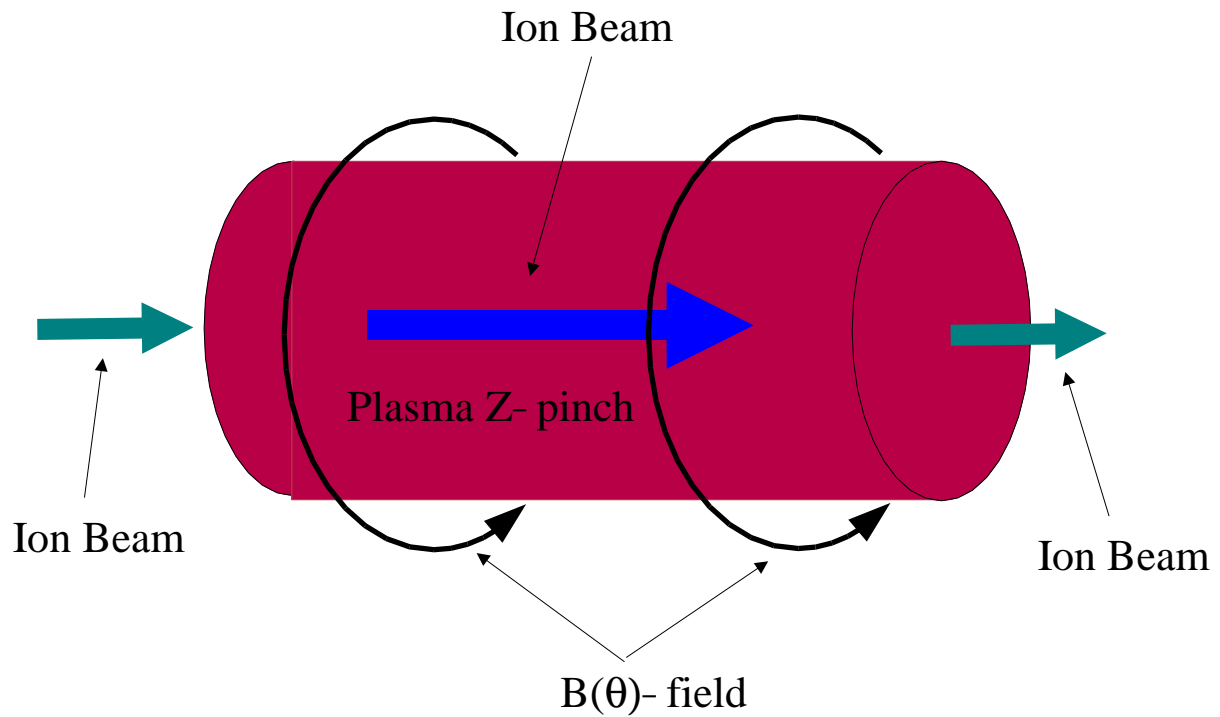
Figure 1.8: Diagram illustrating the fundamental physics for plasma channel beam transport: Upon the establishment of the equilibrium z-pinch condition, the plasma magnetic field is set up for beam transport and plasma electron density stands to neutralize the beam's space charge.

must provide for fast space-charge neutralization and long enough magnetic confinement. From Maxwell's equations one can derive characteristic times for both space-charge neutralization and magnetic diffusion. The beam's space-charge neutralization characteristic time can be determined by combining Gauss' law, Ohm's law, and the continuity equation:

$$\frac{\partial \vec{E}}{\partial t} + 4\pi\sigma\vec{E} = 0 \tag{1.5}$$

$$\tau_E = \frac{1}{4\pi\sigma} \tag{1.6}$$

we see that space charge neutralization time is inversely proportional to the plasma conductivity. For the magnetic diffusivity, we combine Faraday's, Ampere's, and Ohm's laws to obtain

$$\frac{\partial \vec{B}}{\partial t} - \frac{c^2}{4\pi\sigma}\nabla^2\vec{B} = 0 \tag{1.7}$$

$$\tau_M = \frac{4\pi\sigma L^2}{c^2} \tag{1.8}$$

where L is a characteristic length of the plasma channel. We see that the magnetic diffusion time is proportional to the conductivity. Both equations (1.5) and (1.7) were derived assuming that the bulk of the plasma is static [44]. From the aforementioned equations, we can see that the beam would be effectively space-charge neutralized if the channel exhibits Spitzer conductivity, given by:

$$\sigma = \frac{1}{\eta} = \frac{(k_B T_e)^{\frac{3}{2}}}{\pi e^2 m^{\frac{1}{2}} \ln\Lambda} \tag{1.9}$$

hence under the condition of high ionization fraction, the plasma would eliminate transverse repulsive forces while at the same time its confining azimuthal magnetic field would not

diffuse significantly during beam transport. This is,

$$\tau_E << \tau_{beam} << \tau_M \tag{1.10}$$

Specifically, for a 10 eV plasma, $\sigma \sim 3 \times 10^{14}$ s^{-1} and we obtain $\tau_E \sim 10^{-16}$ s, $\tau_{beam} \sim 10^{-8}$ s, and $\tau_M \sim 10^{-6}$ s consistent with inequality (1.10).

In terms of beam transport capacity, the plasma channel relaxes many sensitivity constraints on the accelerator driver, such as the transverse beam emittance requirements (which would have a direct impact on the ion source-injector system), beam energy spread, and ion charge state, thus enabling for a lower cost driver. To see this, let us look at a simplified model for the z-pinch. Here, one would assume that the channel has a uniform current density $J(r)$ for a given channel current I:

$$J(r) = \begin{cases} \frac{I}{\pi R^2} & \text{for } r \leq R \\ 0 & \text{for } r > R \end{cases} \tag{1.11}$$

where r is the radial coordinate and R is the pinch radius. From Ampere's law, the induced azimuthal magnetic field $B_\theta(r)$ is given by:

$$B_\theta(r) = \begin{cases} 2\frac{I}{cR^2}r & \text{for } r \leq R \\ 2\frac{I}{cr} & \text{for } r > R \end{cases} \tag{1.12}$$

An incoming ion making it into the plasma channel will feel a radial force due to the azimuthal magnetic field. Applying Newton's second law to an incoming test ion (or any test charged particle for that matter) with velocity $\vec{v}_z$ into the channel, we obtain:

$$\frac{d^2\vec{r}}{dt^2} = \frac{Ze}{mc}\vec{v}_z \times \vec{B}_\theta \tag{1.13}$$

or

$$\frac{d^2r}{dt^2} = -2\frac{Ze}{m}\beta\frac{I}{cR^2}r \tag{1.14}$$

for particles within the channel. Here Z is the particle charge state, m the particle mass, and $\beta = v/c$. If we now parameterize the equation using the particle's orbit z-coordinate along the plasma channel and using the fact that $v = dz/dt$ we obtain:

$$\frac{d^2r}{dz^2} + k^2(z)\, r = 0 \tag{1.15}$$

where

$$k^2(z) \equiv 2\, \frac{eZ(z)}{R^2(z)}\, \frac{I}{\beta m c^3} \tag{1.16}$$

Equation (1.16) emphasizes that both Z and R are functions of the particle axial position along the channel. Equation (1.15) is known as Hill's equation and in accelerator theory describes the betatron oscillations transversed by a particle in a focusing lattice [17]. Hence the magnetic field of the plasma channel maintains the ion beam within its radius. One is interested in determining how sensitive is the excursion of the betatron oscillations due to variations in the beam's energy, momentum, and ion charge state. Hill's equation has the general solution:

$$r(z) = A\, w(z) e^{i(\psi(z)+\delta)} \tag{1.17}$$

where A and δ are constants of integration, and $\psi(z)$ is a periodic function with the same periodicity as k.

Upon substituting equation (1.17) into equation (1.15) and having the coefficients to the harmonic terms vanish independently, we obtain the differential equations for which both $w(z)$ and $\psi(z)$ need to satisfy:

$$\psi' = \frac{1}{w^2} \tag{1.18}$$

and

$$w'' + k^2 w - \frac{1}{w^3} = 0 \tag{1.19}$$

In the absence of instabilities the plasma channel's radial variation will be much smaller compared to its overall length, it is safe to use the adiabatic approximation. So for

$$\frac{1}{k^2}\frac{dk}{dz} << 1 \tag{1.20}$$

we have that $w'' \approx 0$, then we can write

$$r(z) = \frac{C}{\sqrt{k}}\, e^{\, i \int k\, dz} \tag{1.21}$$

where C is a constant.

We can find what the maximum particle excursion would be. Let $a^2 = |r|^2$, then

$$a^2 = |r(z)|^2 = \frac{\varepsilon}{k} \tag{1.22}$$

where $\varepsilon = C^2$ is the emittance. In reality, ε is a measure of the RMS phase space area in both the $x - x'$ and the $y - y'$ planes.

From here we can determine the fractional variation of the amplitude $\delta r/r$ as it relates to that of the fractional variation of the oscillation wavenumber $\delta k/k$:

$$\frac{\delta r}{r} = \frac{1}{2}\frac{\delta k}{k} \tag{1.23}$$

From equation (1.16) and $E/c^2 = (1/2)m\beta^2$ we obtain the relations:

$$\frac{\delta k}{k} = \frac{1}{2}\frac{\delta \beta}{\beta} = \frac{1}{4}\frac{\delta E}{E} \tag{1.24}$$

from which one can explain how the emittance, momentum, and energy spread requirements of the driver are relaxed. In other words, once the beam is delivered to the plasma channel, the beam spot size at the target is determined by the channel's diameter. Hence it is important to have the beam move through the channel at its MHD equilibrium time.

It is important to note that these are natural limitations to consider. Since the current rise is inductively limited, there is a minimum radius that the channel can reach. In our experiment, the minimum pinch diameter is $\approx 1\,\mathrm{cm}$. This diameter limits the type of target that can be used [7] [5], thus affecting the gain and the net energy yield. Certainly it is out of the question a target that requires a $2\,\mathrm{mm}$ spot size if the channel provides a $1\,\mathrm{cm}$ conduit. On the other hand, there are target designs that can be used effectively with the plasma channel. For example the hybrid target shown in figure 1.6 is an optimized target that accepts an ion beam with a spot diameter of about $1\,\mathrm{cm}$ with a gain of 55 from a $6.7\,\mathrm{MJ}$ of beam energy [14]. The important issue to keep in mind, as far as the plasma channel used for beam transport is concerned, is that the only assumptions made up to now are stable channels with uniform current density.

One of the problems inherent to MHD equilibrium is its stability [32] [44]. In particular, z-pinches are prone to be unstable in a series of distinct modes when the equilibrium has perturbations of the form $A(z)e^{im\theta}$, where $A(z)$ is an amplitude displacement variation small compared to the pinch radius, m is an integer, and θ is the channel's azimuthal angle [44]. The $m = 0$ mode is known as the sausage instability, and the $m = 1$ as the kink instability, being these the most likely to occur. While it is impossible to eliminate these instabilities, it is feasible to significantly reduce the growth rate of them. Jackson [32] suggests that stabilization can be achieved by the action of an outer conductor wall enclosing the z-pinch [32]. Experiments at the Naval Research Laboratory have demonstrated long stable z-pinches with a stabilizing solid wall that provides a path for the return currents [28]. Manheimer [40] has put forth a theory indicating the conditions for a gas stabilized

discharge in which the equilibrium condition of the z-pinch would be free of instabilities for a time long enough to allow the transport of a charged particle beam. They show that the inertial effects of a gas density gradient surrounding the z-pinch is to reduce the MHD instability growth rate by a factor of $(\rho_p/\rho_g)^{1/2}$, where ρ_p is the density of the pinch and ρ_g is the density of the surrounding gas. Explicitly, the growth rate Γ is given by:

$$\Gamma \approx k v_{Ap} \left\{ \left(\frac{\rho_p}{\rho_g} \right)^{1/2} \left[1 + k r_p \left(\frac{P_p}{P_g} \right)^{1/2} \right] \right\} \tag{1.25}$$

where the subscripts p indicate pinch parameters, g gas parameters, k the instability mode wavenumber, $v_{Ap}^2 \equiv B_0/\mu_0 \rho_p$, and r_p the pinch radius and P the pressure. The growth rate for a pinch in vacuum is:

$$\Gamma \approx k v_{Ap} \left[-\ln \left(\frac{1}{2} k r_p \right) - \gamma_E \right] \tag{1.26}$$

where $\gamma_E = 0.5772 \cdots$ is Euler's constant. Manheimer further does a case analysis for lightning where the discharge conditions are quite similar to the discharges described in this experiment. They show that for the density ratio $\rho_g/\rho_p \gg 1$ the growth rate can be smaller by at least an order of magnitude compared to that of vacuum putting the growth rate for our discharges on the order of 10^{-3} s with $k r_p < 1$ and $m = 1$ mode instability which are the conditions that present the largest growth rates. It seems that the instability problem might have already been overcome experimentally. The plasma channel experiment at the Lawrence Berkeley National Laboratory (LBNL) has demonstrated stable 40 cm long plasma channel z-pinches carrying a current in excess of 50 kA through the use of a double pulse discharge technique in which the first discharge sets the stabilizing conditions for the second discharge in which the z-pinch occurs.

1.4   Goals of this Work

As mentioned in section 1.1, the immediate objective of this work is to present an experimental study and analysis of the dynamic phenomena of the LBNL z-pinch. This is important since it lays a basis for comparison and validation of simulation codes that can be used on extrapolated values of the relevant parameter space. In order for the z-pinch plasma channel to be useful as ion beam transport, the channel needs to be stable, present the right plasma conductivity, and have an appropriate current density distribution. Attempts are made to make a direct measurement of these parameters. When this is not possible, an indirect approach is used. This study focuses on the channel production. Beam-channel interactions are left outside the scope of this work. From the general point of view, the aim is also to make this thesis a suitable starting point for future z-pinch transport research. To this, a brief historical survey is presented in chapter 2. The experimental set up is discussed in chapter 3, in which technical and practical details are discussed for the benefit of those trying to reproduce these results. These details are the direct result of working day in and day out with the hardware. Chapter 4 describes the diagnostics used to measure the plasma parameters. I analyze the results obtained and give a phenomenological description of them in chapter 5. In chapter 6, I discuss the theoretical implications and the efforts to simulate the experiment. The finer details and academic background are covered in the appendix section.

Chapter 2

Previous Work on the Z-Pinch

In the following sections I will present a brief survey of the recent efforts done that are relevant to this study. In particular, I will highlight those results that complement the findings of this dissertation.

2.1 Initial Work on the Plasma Z-Pinch

The formal study of plasmas dates back to Tonks and Langmuir in the first quarter of the twentieth century [74]. Self-focusing of electron streams in gases were reported in 1934 [8] and the pinch effect was reported in 1957 [13]. These studies have branched out to many subfields. One of these subfields is the study of plasmas in the regime of negligible collision frequency called magnetohydrodynamics (MHD). MHD theory predicts the possibility of conditions called as MHD equilibrium with the most notable examples being the theta-pinch and the z-pinch [13] [44] [15] [32]. It was immediately realized that these equilibrium conditions had various practical applications, especially for fusion energy

plasma confinement. Further study revealed that MHD equilibrium is inherently unstable [32] [13]. Due to this, advances in the practical applications of both z-pinch and theta-pinch phenomena has been slow, but resurgence has taken place in the last decade with the pressing need, amongst others, for alternative sources of energy.

2.2 Work at Sandia National Laboratory

The work done at Sandia National Laboratory (SNL) conducted by J. N. Olsen [23] [48] [49][51] has been mostly an effort directed on the utilization of laser initiated z-pinch plasma channel for light ion fusion (LIF). In their experiments they produced a channel with a single electrical discharge in a chamber with an ammonia atmosphere of up to 20 torr. The ionizing laser was a CO_2 laser tunned at one of the ammonia molecule resonances. The SNL effort was altogether successful in producing a free standing stable channel over one meter with a maximum peak current of 35 kA. LIF applications required 40 kA and the SNL experiments would make consistent channels in the 27 kA range [49]. Once the current exceeded the value of 35 kA the channel exhibited MHD instabilities rendering the channel useless for LIF transport since beam currents far exceeded the MHD instability free channel current. Light ion propagation experiments were conducted successfully demonstrating ion transport in a wire initiated plasma channel carrying ~ 40 kA [50].

2.3 Work at Naval Research Laboratory

The work performed at the Naval Research Laboratory (NRL) was also originally directed to support the LIF effort. Extensive studies on pre-formed z-pinch channels were

performed on wire guided and free standing but most notably experiments with wall stabilized channels which are reported by Hinshelwood [28]. Stabilization occurs via low mass insulated current return tube that offers an external wall to the channel. This stabilization approach is also discussed briefly by Jackson [32]. Hinshelwood's study looked at the electrical behavior of discharges with various gas species, pressures, lengths and currents.

From the side of the HIF effort, the transport emphasis was on self-pinched transport. Self-pinch transport was observed for a series of experiments performend on GAMBLE II for a 1 MeV 100 kA proton beam [54].

2.4 Work at Gesellschaft für Schwerionenforschung

The work conducted at Gesellschaft für Schwerionenforschung (GSI) in Darmstadt, Germany, have been related to the ongoing effort at LBNL. There has been a very strong collaboration that has complemented each other's institutions research significantly. At GSI their studies have revolved around the understanding of free standing z-discharges produced in ammonia, similar to the ones produced at SNL, but with the pre-pulse technique. A complete report of these studies and references are found in Niemann's PhD dissertation [45]. In addition to plasma channel characterization studies, ion beam transport experiments have been carried out. Although the beam propagated through these channels is not intense enough to represent a beam produced by a HIF driver, the results yield by these experiments confirm and substantiate the transport and focusing properties of the free standing plasma channel [16] [9].

2.5   Work at Lawrence Berkeley National Laboratory

The focus of the LBNL research has been in developing a HIF driver with the capability of delivering, in one of many scenarios, a 6.5 MJ Pb ion beam composed of a 3 GeV, 30 ns pre-pulse beam with 2.1 MJ followed by 4 GeV, 8 ns main pulse with 4.4 MJ. One of the scenarios for final focus as mentioned in chapter 1, is through a plasma channel transport. It was realized by this time, based on the SNL and NRL experiments that a wall stabilizing effect was needed to successfully increase the channel current to achieve parameter conditions needed for beam transport. It was proposed by Yu and Tauschwitz to use a pre-pulse discharge to create a preferential breakdown path for the main bank z-discharge [73]. Initial experiments done by Tauschwitz at LBNL showed that a stable 44 cm plasma channel carrying 55 kA could be produced using this double pulse technique [73].

Initial studies to characterize and understand the LBNL plasma channel started with Fessenden and Vella [20]. Their principal interest was to determine the unexplained effect of the increased stability in Tauschwitz channel and to find any practical difficulties that would render the channel completely incompatible in an ion beam final focus and transport application. There overall study found no incompatibilities. The study also included channel-target interactions [20]. Given these results, it was decided that a more formal study was needed to further the understanding of the channel dynamics. Initial simulation studies were initiated by R. Peterson at the University of Wisconsin using the BUCKY computer code [59]. The hydrodynamic results described the channel evolution well in a qualitative manner, but the code did not incorporate an electron avalanche model.

Electron avalanching seemed to be an important part of the physics that needed to be incorporated into the simulation code.

Chapter 3

Experimental Setup

The following chapter describes the z pinch plasma channel experimental hardware set up. It can be described as a small pulsed power station with the flexibility of incorporating a set of diverse diagnostics. The channel production technique is also described in this chapter.

3.1   Apparatus

The target chamber in an ICF power plant would have approximately 6 m in diameter and the interior would be under a background partial pressure of FLiBe vapor. Ideally one would perform experiments in a full scale apparatus with the appropriate conditions, but obviously this would be costly and to some extent impractical. As proof of principle and physical characterization, the plasma channels at LBNL are produced in a small scale setup. While parameters such as total inductance are different for different configurations and sizes, this scaled experiment will provide with a starting point to extrapolate to full

Plasma Channel Z–pinch Double Pulse Discharge Technique Timeline
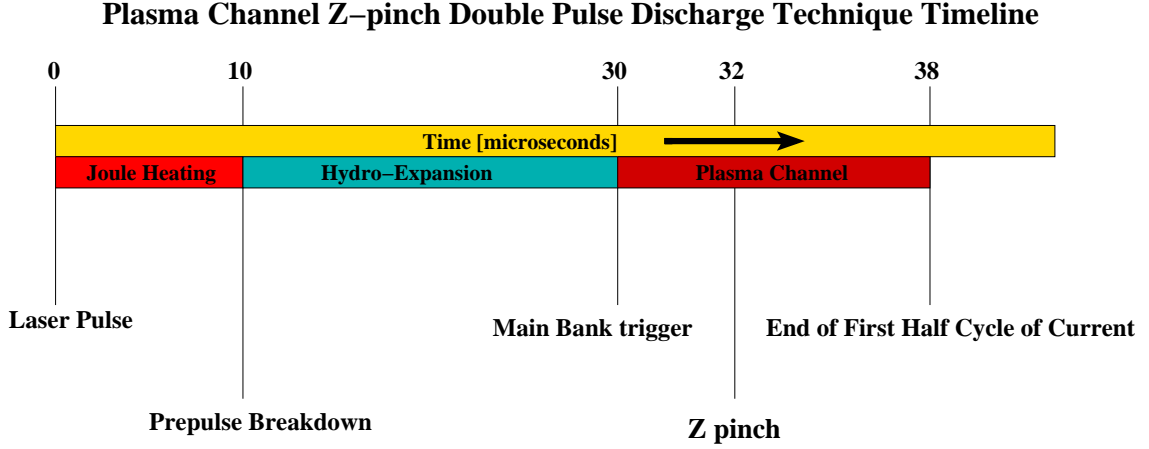
Figure 3.1: Time line of events in the double pulse technique for z-pinch plasma channel production.

scale. In this chapter, I will first describe the hardware where the channels are produced, then I will proceed to describe the production process. The channels are laser beam initiated and the laser provides for initial gas pre-ionization. After the laser passes through the experiment chamber, a pre-pulse capacitor is triggered by the initial laser pulse. A second discharge, the main bank discharge, is then produced $\sim 20\,\mu$s to $30\,\mu$s after the pre-pulse capacitor has fired. During this time is when the z-pinch occurs. A time line of events is presented in figure 3.1 and a schematic and basic phenomenology are presented in figure 3.2.

3.1.1   The Chamber

The apparatus consists of a rectangular aluminum chamber mounted on an optical table. Figure 3.3 shows a picture of the chamber. The chamber is fitted with two copper electrodes separated a distance of $44\,$cm and surrounded by Plexiglass cylindrical shrouds meant to isolate the electrodes from the chamber walls and increase the dielectric path
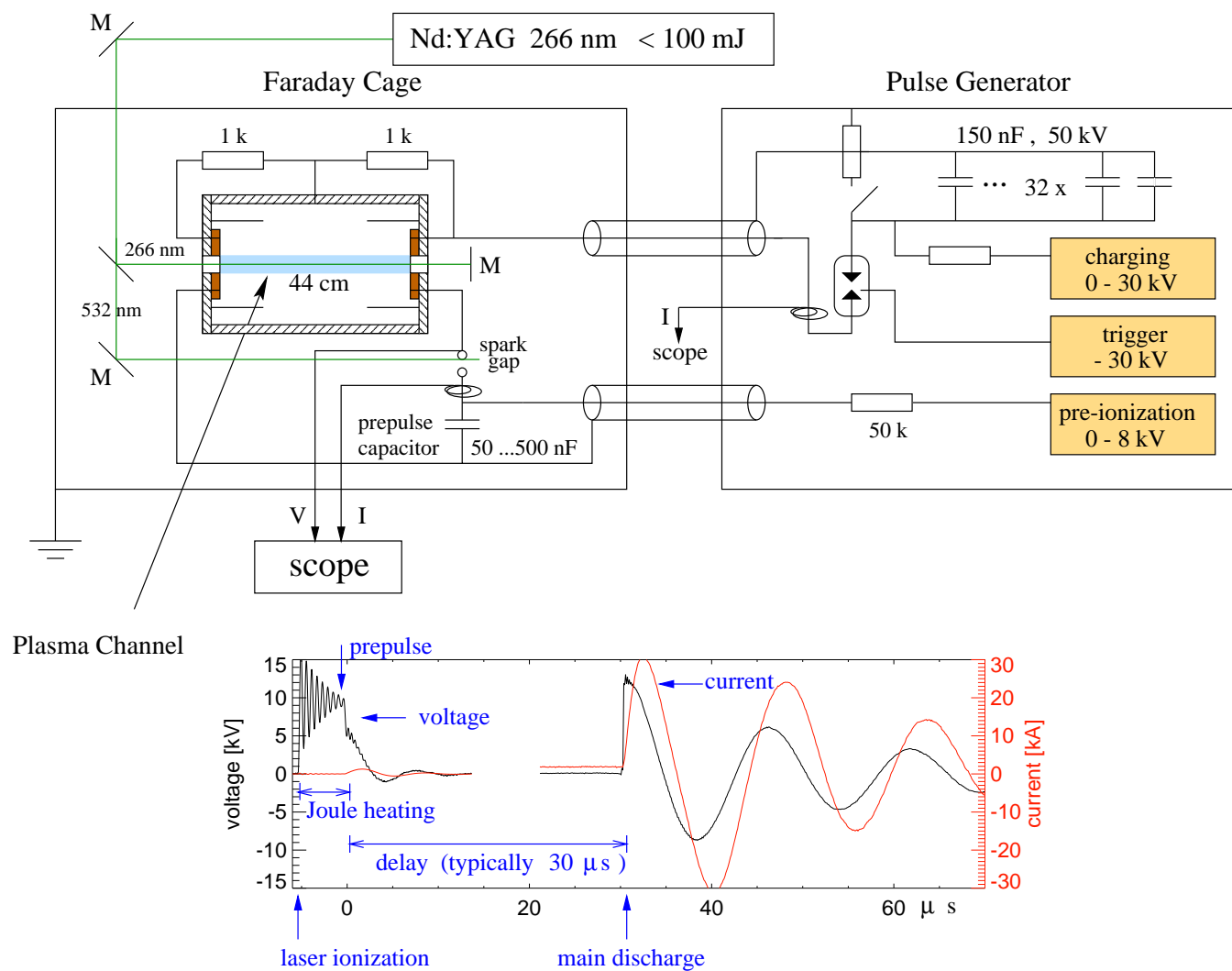
Figure 3.2: LBNL plasma channel experiment schematic: (a) Basic schematic of the experimental setup; (b) phenomenology of pre-pulse and main bank discharges
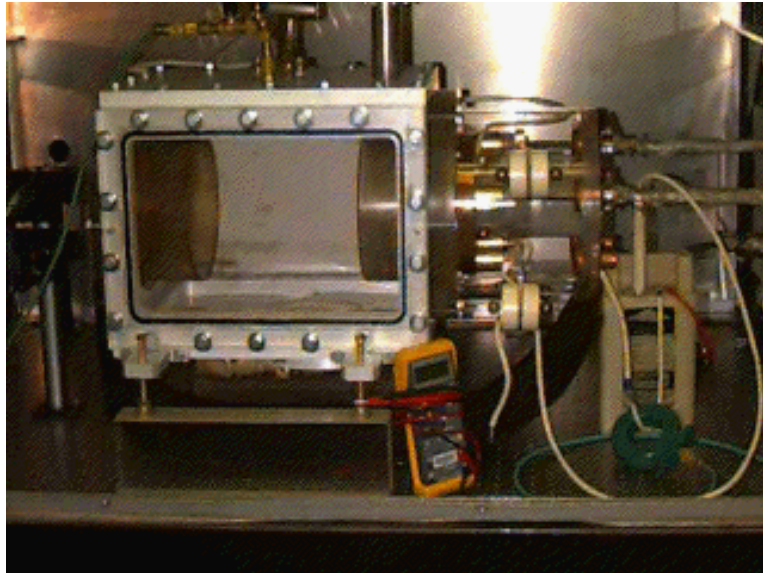
Figure 3.3: Picture of the experimental chamber. The white object on the right is the pre-pulse capacitor

length. The chamber has five removable covers. One side cover is made of 1/2 inch Plexiglass with the purpose of having a large window to determine by simple unaided observation if a successful channel was produced. All six sides are fitted with 2 inch diameter optical grade view ports with an effective 45 mm clear aperture diameter. The two windows along the length of the chamber provide entry ports for the initial ionization laser while the remaining four are diagnostic ports. The port windows can be replaced to accommodate the particular diagnostic wavelengths which range from ultraviolet frequencies requiring fused silica windows to infrared where zinc selenide optics are required for probing.

3.1.2 The Laser

The discharge is initiated with a laser pulse. A Spectra-Physics DCR-4 frequency quadrupled Nd:YAG is used in the present setup. A Lambda-Physik krypton-fluoride

excimer laser has also been used successfully. The ultraviolet component of the beam, $\sim 100\,\text{mJ}$, $10\,\text{ns}$ pulse at $\lambda = 266\,\text{nm}$ in a double pass arrangement, is sent through the chamber and used to produce the initial gas pre-ionization. The laser beam is focused to the chamber's midpoint with a focal spot of $\sim 100\,\mu\text{m}$. The average spot size through the effective length of the chamber is of approximately $1\,\text{mm}$. In order to achieve initial gas ionization with relatively small laser fluence, a partial pressure fill of benzene is used due to its relative large absorption cross section to UV photons. The principles of photoionization and the effects of benzene will be discussed later in this chapter. The second harmonic component is used to trigger the pre-pulse capacitor, while the fundamental is sent to a beam dump.

3.1.3 The Power Pulsers

Electrically, one of the chamber's electrodes is solidly connected to ground while the other is connected to two capacitive pulsers, namely, the pre-pulse capacitor and the main capacitor bank as shown in figure 3.2(a). The chamber sits at a potential in between ground and the applied high voltage as determined by a two $1\,\text{k}\Omega$ resistor voltage divider. The pre-pulse capacitor sits next to the chamber and it is triggered by the second harmonic beam of the ionizing Nd:YAG laser beam via a brass ball pair spark gap. The pre-pulse $50\,\text{kV}$ capacitor can be readily exchanged with units ranging from $0.05\,\mu\text{F}$ to $0.5\,\mu\text{F}$ to provide for pre-pulse energy scans. The chamber and the pre-pulse capacitor are enclosed by an isolation faraday cage. The main capacitor bank pulser is a separate stand alone unit composed of two Glassman variable DC high voltage power supplies, an electronically triggered spark gap, safety interlock mechanisms, and thirty two $50\,\text{kV}$, $150\,\text{nF}$ capacitors connected in

parallel. The pulser is connected to the chamber's high voltage electrode through a pair of high current shielded coaxial cables. Of the power supplies, one is dedicated to the pre-pulse circuit and the other to the main bank. Pre-pulse current measurements are performed through a rogoski coil located between the pre-pulse capacitor and the electrode and voltage measurements are done with a calibrated voltage divider connected directly between the electrode and ground. Main bank measurements are done inside the pulser unit with an independent in house manufactured rogoski coil to measure current right after the main bank spark gap and a voltage divider connected to the main bank spark gap plate and ground.

3.1.4 Timing

Since optimum stable laser energy output occurs when the laser operates at $10\,\mathrm{Hz}$, the laser is triggered by a Stanford Systems delay generator set up as a master clock. A channel is produced by manually actuating an optical shutter that blocks the second harmonic beam from the Nd:YAG laser, thus preventing the capacitor of being triggered at the same rate as the laser operation rate. The timing scheme is shown is figure 3.4. Since the $10\,\mathrm{Hz}$ laser repetition rate is high for single shot studies, a synchronization box is used to mark the coincidence time of laser pulse and pre-pulse breakdown. The synchronization box takes the $10\,\mathrm{Hz}$ signal and the pre-pulse voltage picked up from a voltage divider, then transforms them into TTL pulses that are sent into a logical AND gate. This makes it possible to trigger the main bank and diagnostics accordingly. Delayed signals from the Stanford unit are used to trigger other diagnostics.
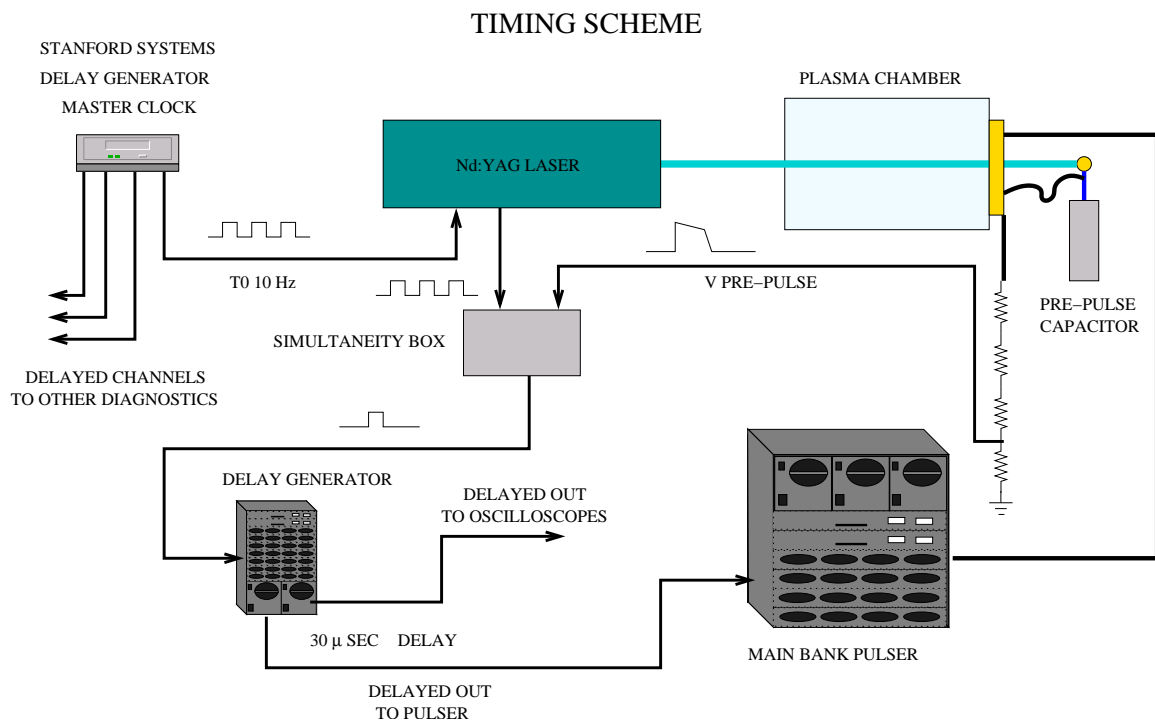
Figure 3.4: Timing scheme set up for the double pulse technique. The main bank pulser and channel diagnostics are triggered if and only if there is coincidence between the ionizing laser and applied pre-pulse voltage, i.e, a pre-pulse channel was produced.

3.2 Z-Pinch Plasma Channel Production

The original idea to produce the z-pinch was to pass a laser beam through the chamber and immediately trigger the main bank pulser. This proved to be a very inefficient method for channel production since more often than not, voltage breakdown would occur to the chamber walls. As a result, it was proposed to create a smaller discharge preceding the main bank discharge. The purpose was to add consistency and repeatability to channel production. It wasn't realized at the time that this technique would prove beneficial to the plasma channel in more ways than one.

3.2.1 The Double Pulse Technique

The phenomenology of the plasma channel is shown in figure 3.2 (b). Typical initial conditions are a 7 torr nitrogen gas fill, 7 kV pre-pulse capacitor charge potential, and 15 kV to 30 kV main bank charge voltage. The initial event (t_0) is the passage of the ionizing laser beam through center longitudinal axis of the chamber to produce seed electrons. The laser beam-to-gas interaction alone is not enough to produce the electrons necessary for the joule heating process and promote the conditions for breakdown. A partial fill of benzene vapor, typically between 0.5 torr and 2.0 torr, is added to enhance the UV absorption cross section. Once the UV laser beam ionizes the nitrogen-benzene fill, the pre-pulse voltage is applied. This heats the gas through electron-ion collisions, thus expanding the inner axial core. Figure 3.5 shows the current and voltage waveforms during the joule heating process. Joule heating takes place in a time frame of about $5\,\mu s$ to $15\,\mu s$. When the proper ratio of electric field to gas pressure is reached, avalanche ionization occurs. This is
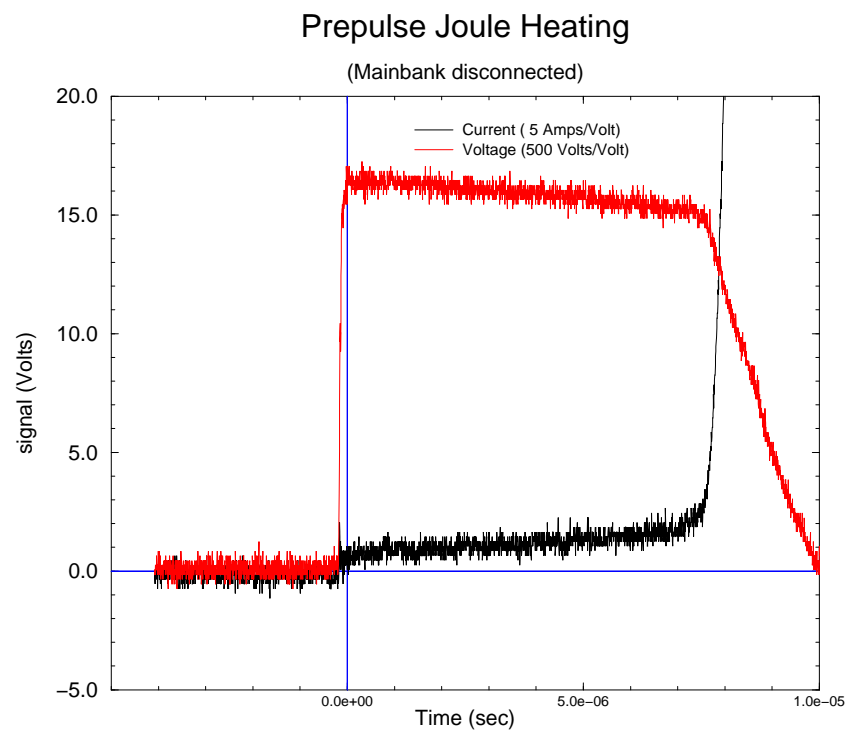
Figure 3.5: Pre-pulse voltage and current waveforms showing the period for joule heating
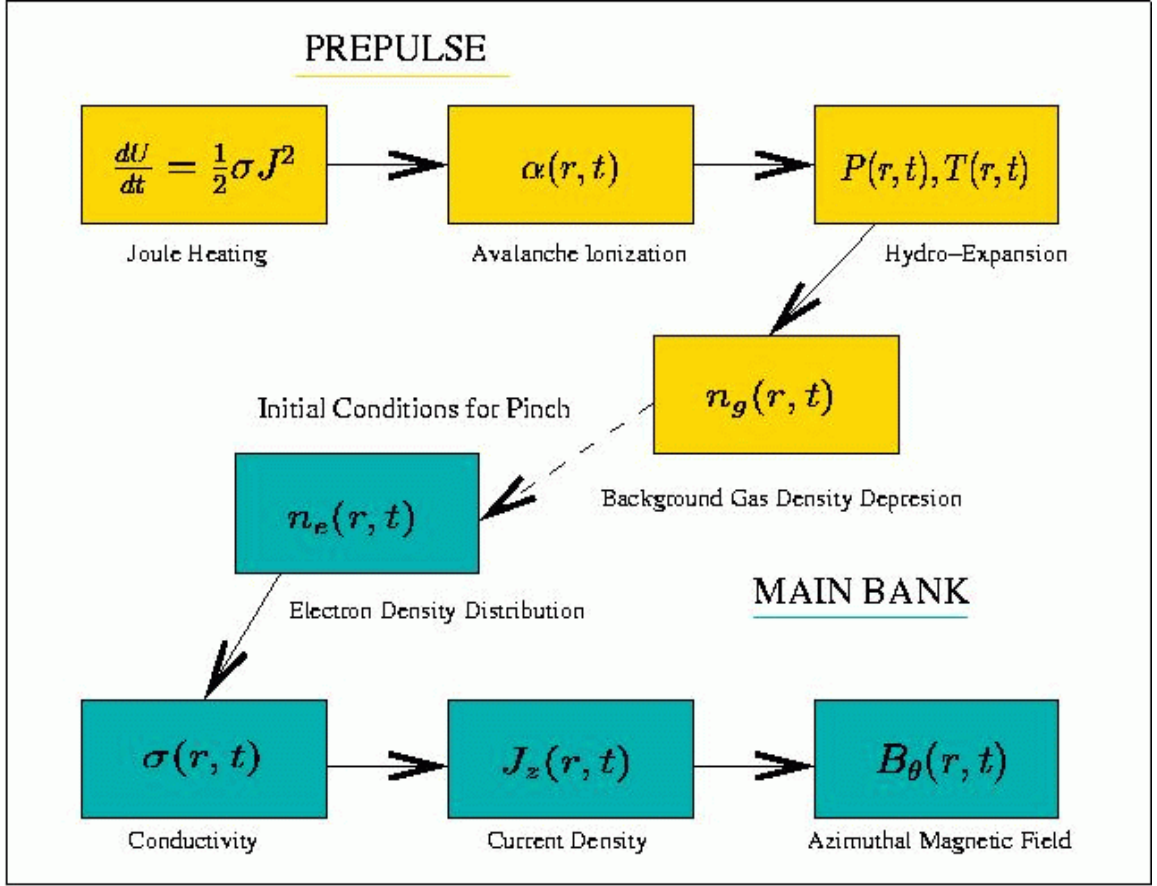
Figure 3.6: Diagram illustrating the double pulse process and critical parameters. Upon initial laser ionization, the electric field between the electrodes promotes joule heating on axis to produce pre-pulse breakdown. The pre-pulse sets the initial conditions for the main bank z-pinch discharge.

the pre-pulse breakdown stage. The pre-pulse capacitor energy gets dumped in $\sim 2\,\mu$s. This fast energy deposition produces a rapid heating and expands the inner material outward creating an outward shock wave. This in turn creates a gas density depression on axis which facilitates the initiation and stabilization of the main bank z-pinch. The pre-pulse sets the initial conditions for the plasma channel. Main bank trigger is set up to go off $30\,\mu$s after application of the pre-pulse voltage on the chamber electrode. The Main bank trigger timing can be set arbitrarily with nanosecond precision, thus making it easy to synchronize it to

an accelerator. Figure 3.6 shows the critical parameters for the double discharge process. The gas density depression left by the pre-pulse serves as the preferred electric breakdown path for the plasma channel z-pinch. How the pre-pulse affects the main bank discharge is part of the object of this study.

3.2.2 Electrical Characteristics of the System

It is necessary to determine the electrical characteristics of the electrical system in order to differentiate them from the ones intrinsic to the plasma channel. Also as a result of this, one can take the parameters physically measured and use them as initial checks for the simulation codes. By applying a short circuit between the chamber electrodes, one is effectively left with an RLC circuit for which one needs to solve for the resistance and the inductance. The short is made with a brass rod that fits between the electrodes. The equation that describes the circuit, in terms of the current I, is

$$\frac{d^2I}{dt^2} + \beta\frac{dI}{dt} + \omega_0^2 I = 0 \tag{3.1}$$

where $\beta \equiv R/L$ and $\omega_0^2 \equiv 1/LC$. The very well known solution to this ordinary second order differential equation is

$$I(t) = I_0\, e^{-\alpha t} \sin \omega' t \tag{3.2}$$

where we set $\alpha \equiv \beta/2$, $\omega' \equiv \sqrt{\omega_0^2 - \alpha^2}$, and the initial condition of $I(0) = 0$. With the known capacitance, from the current waveforms one measures the decay constant α and the oscillation frequency ω' to solve for the resistance R and the inductance L. Measurements, shown in figure 3.7, were made for both the pre-pulse and the main bank, with the resultant values for R and L shown in table 3.1.
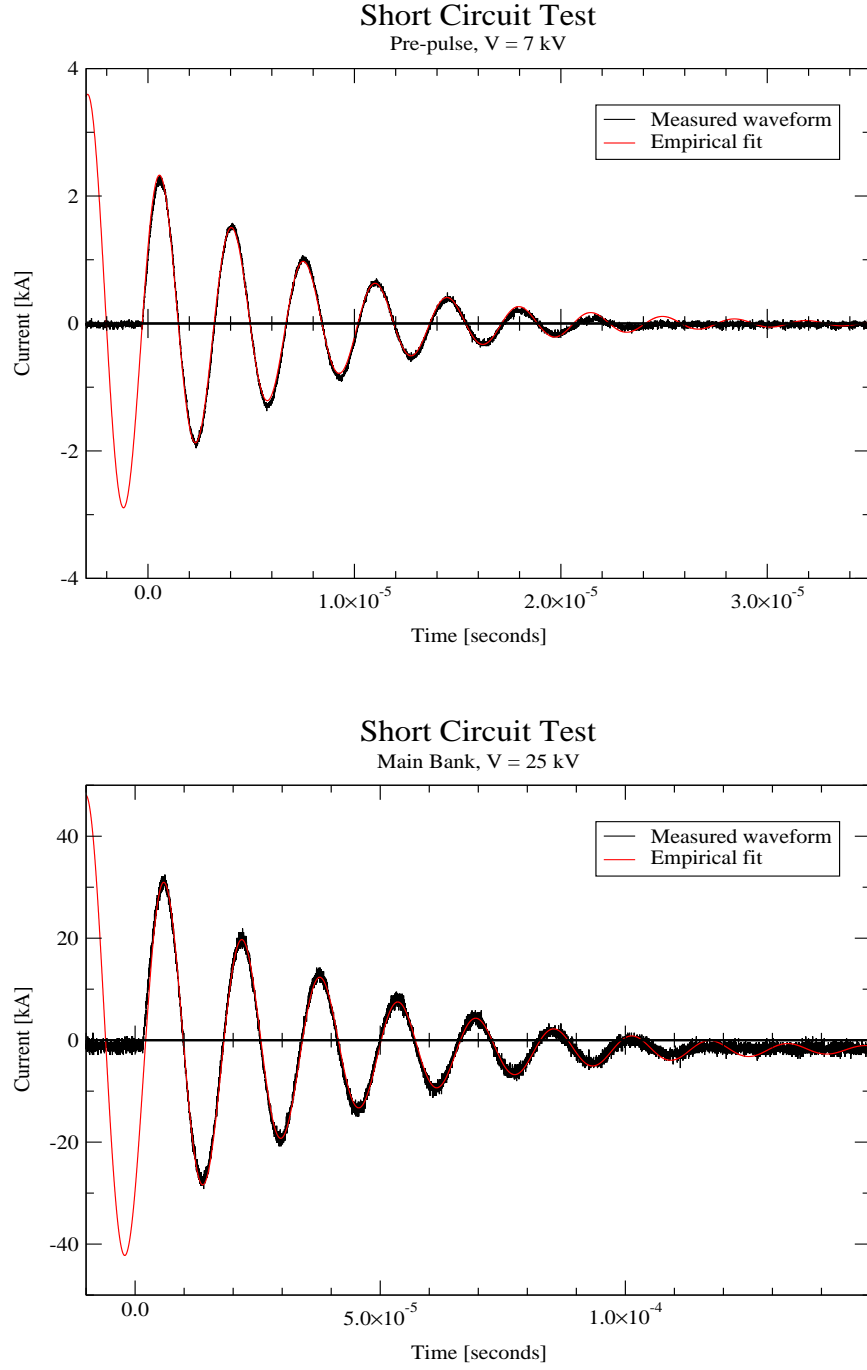
Figure 3.7: Short circuit current waveforms for the pre-pulse and the main bank. For the pre-pulse the fit is accomplished with $\alpha = 1.25 \times 10^5$ s^{-1} and $\omega' = 1.804817 \times 10^6$ radian/s. For the main bank, $\alpha = 2.64 \times 10^4$ s^{-1} and $\omega' = 3.95 \times 10^5$ radian/s.

Parameter	C	R	L
Pre-Pulse $\alpha = 1.25 \times 10^5 \, \mathrm{s}^{-1}$, $\omega' = 1.804817 \times 10^6$ radian/s	$0.15 \, \mu\mathrm{F}$	$0.50911 \, \Omega$	$2.036 \, \mu\mathrm{H}$
Main Bank $\alpha = 2.64 \times 10^4 \, \mathrm{s}^{-1}$, $\omega' = 3.95 \times 10^5$ radian/s	$4.80 \, \mu\mathrm{F}$	$7.013 \times 10^{-2} \, \Omega$	$1.329 \, \mu\mathrm{H}$

Table 3.1: Values of R and L for the pre-pulse and main bank circuits calculated from the short circuit test.

3.2.3 Gas Laser Ionization Process

Sullivan [70] in his work notes two distinct regimes in which photoionization of atoms and molecules can occur: Tunneling ionization and multiphoton ionization. The criterion which distinguishes between the two is know as the Keldysh parameter γ

$$\gamma = \left(\frac{E_i}{2U_p} \right)^{1/2} \tag{3.3}$$

where E_i is the ionization threshold of the atomic level and U_p the electron quiver or ponderomotive energy. $U_p \propto I/\omega^2$, I being the intensity and ω the frequency of the incident laser field. When $\gamma >> 1$, e.i. ω large, the ionization is multiphoton dominated. Conversely, when $\gamma << 1$ the ionization occurs preferentially through the tunneling process. An alternate way of considering this issue is to compare the ratio of the laser electric field to that of the atom or molecule binding the electrons. If this ratio is small, one is justified to utilize perturbation theory to the atomic Hamiltonian and compute energy shifts to the stationary solutions of the unperturbed Hamiltonian. This allows for the possible creation of virtual states that facilitate transitions to the continuum, hence we have multiphoton

ionization. The opposite can be said for the tunneling case where the large laser electric field distorts the atomic Coulomb potential well [67]. A complete theoretical study on multiphoton ionization is given by Bruzzese et al. [11].

The above point is of importance since has direct bearing in the selection of the type and size of the ionizing laser to be used in future experiments and possibly the target chamber in a power plant. In my experiment the ionization is through the multiphoton absorption process in benzene, but if a decision is made to utilize a high peak power ultrafast laser to utilize the tunneling ionization process, careful consideration needs to be made of the associated effects [70]. One has to do a calculation of the power requirements under both multiphoton and tunneling ionization in what would be the prevalent atmosphere in the target chamber, which some have suggested to be xenon gas and the partial vapor pressure of FLiBe [82].

3.2.4   Benzene and its Implications

Initial laser preionization presented a problem. The photoionization UV cross sections for nitrogen gas are very small to effectively create a significant electron population to start the joule heating process. For this it is necessary to use a medium with a relatively large photoionization cross section. Laser photoionization of large organic molecules have been studied and have been shown to be suitable sources for the creation of electrons [81] [26]. We chose benzene as the initial laser ionization source medium due to its relative large multiphoton absorption cross section and its relatively large vapor pressure. While certainly a helpful aid for the pre-pulse, and ultimately the z-pinch channel production, benzene has significant disadvantages. Benzene, to a great extent, changes the physical-

chemical processes of nitrogen during the plasma channel production. It interferes with the free electron's lifetime. Electrons produced from benzene are quickly recombined in the presence of a buffer gas such as nitrogen, hence making the nitrogen atom-molecule recombination rates important and non-negligible as far as modeling is concerned. Also during channel production, benzene breaks down and leave copious amounts of free carbon that adhere to to the chamber walls. The carbon deposits change the electrical resistance of the chamber's dielectric shields modifying the conditions under which the plasma channel evolves. A series of tests and measurements were made to characterize the presence of benzene in the experiment. All of these experiments were carried out with the pre-pulse capacitor shorted out, DC power supply set at $2\,\mathrm{kV}$ constant, and certainty the there was negligible current in the absence of the ionizing laser beam. Figure 3.8 shows the current decay waveforms for the resistive period right after laser ionization. The initial electron population produced by the ionization increases, as expected, with benzene partial pressure, but also the current decay is much more steeper suggesting that electron recombination gets enhanced with increased benzene pressure. One can see these effects better if we cast the phenomenology of figure 3.8 in a different form. Figure 3.9 shows how $N_e \propto N_{benzene}$. Electron population for two photon ionization is given by [26] [81]

$$N_e = \alpha \, \frac{\Delta t I^2}{h\nu} \, N_{benzene} \tag{3.4}$$

where I is the laser intensity, Δt the half width of the laser pulse, $h\nu$ the photon energy of the laser, and α the two photon ionization coefficient. As explained by Woodworth [81], α can encompass two photon ionization regardless if ionization occurs by the resonant absorption of two photons or step ionization where the first photon excites the molecule
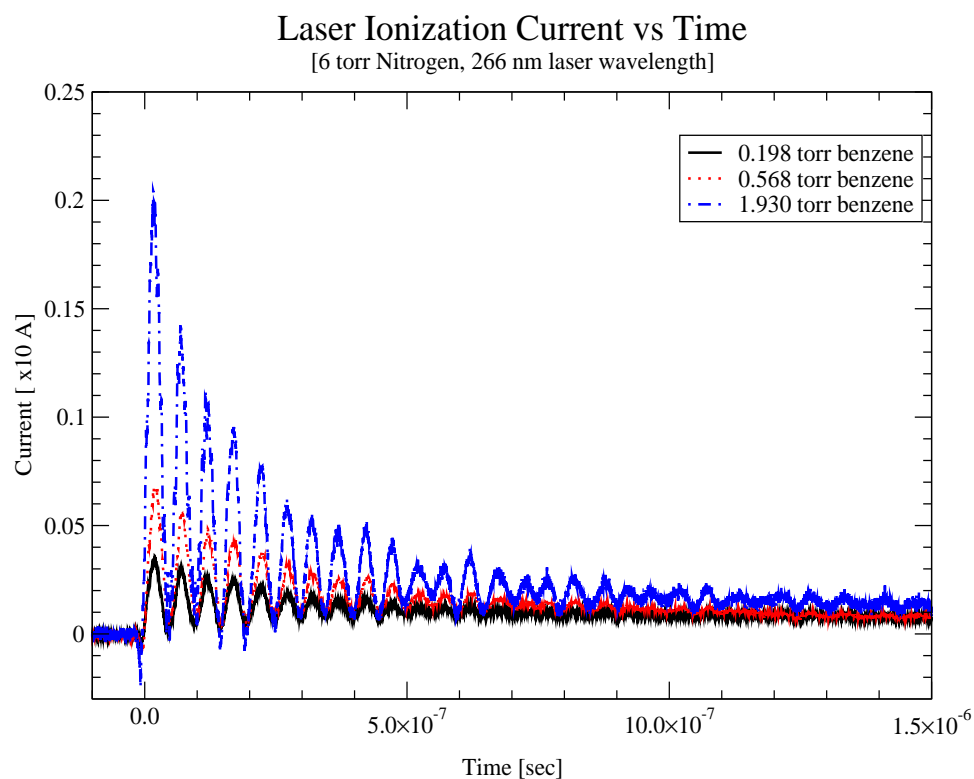
Figure 3.8: Current decay waveforms initiated by laser ionization of benzene as a function of time with benzene concentration as a parameter. This represents an indirect measurement of ionized electron population. The applied voltage was 2 kV and the chamber was cleaned to high vacuum standards to assure that there was no parasite resistance created by carbon residues.
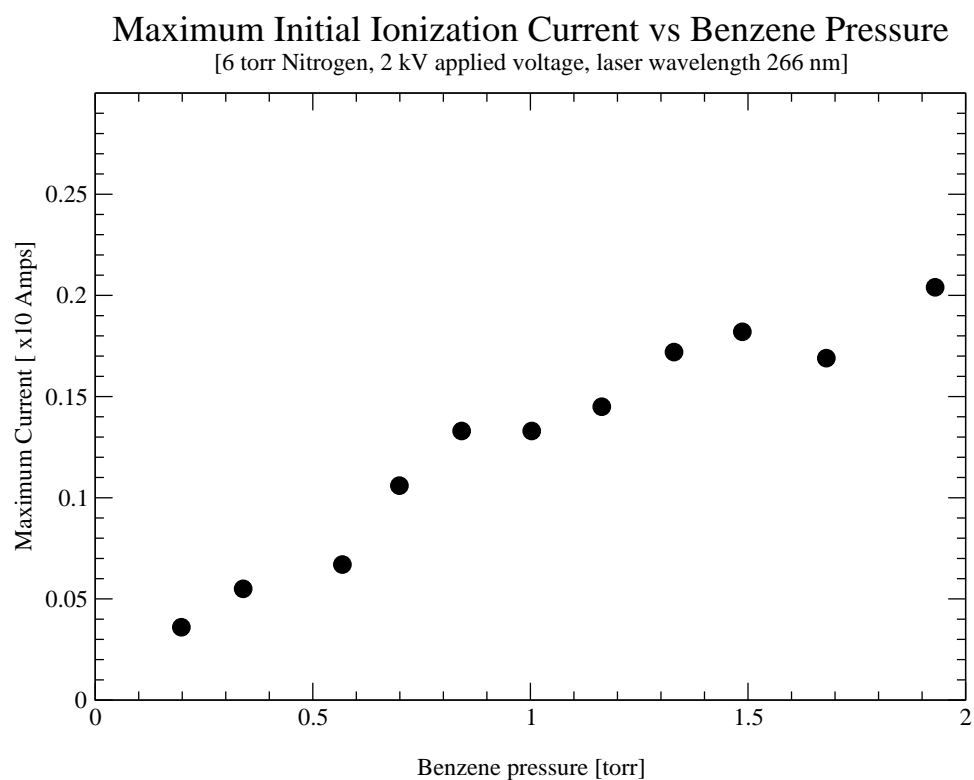
Figure 3.9: Maximum initial current initiated by laser ionization of benzene as a function of benzene concentration. This represents an indirect measurement of the electron population for the initial laser ionization.

Current Decay vs Benzene Partial Pressure

[6 torr Nitrogen, 2 kV applied voltage, 266 nm laser wavelength]
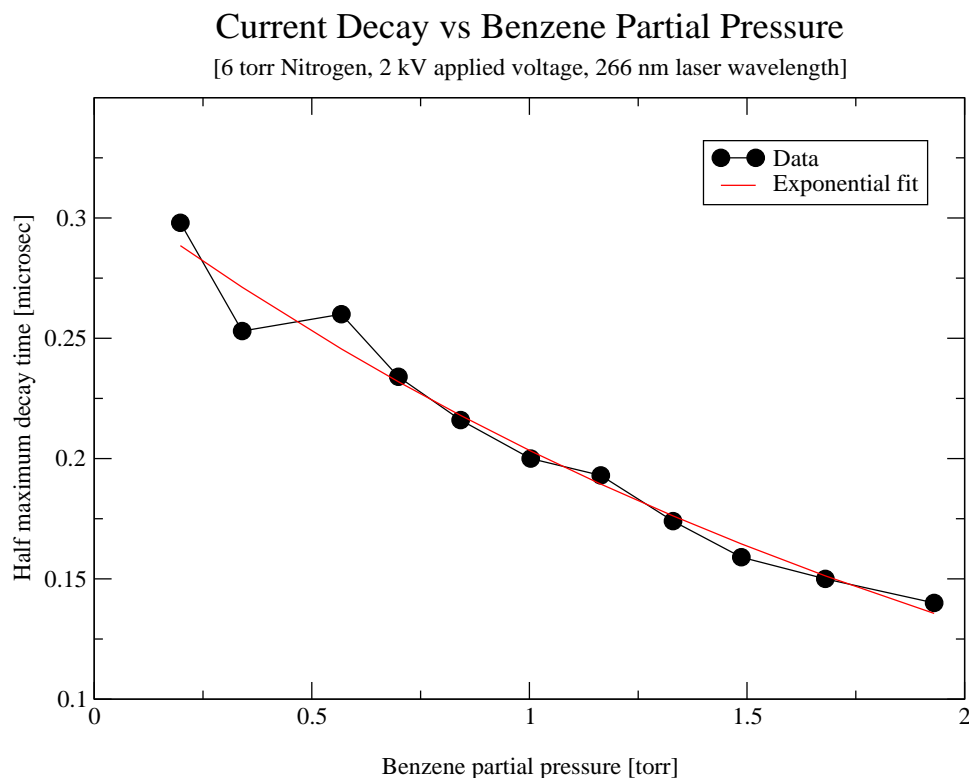
Figure 3.10: Decay time of the current initiated by laser ionization of benzene to half its maximum value as a function of benzene concentration. This represents an indirect measurement of electron recombination for the initial laser ionization.

and then the second photon ionizes the molecule non-resonantly. The effects of enhanced recombination can be seen in figure 3.10 and figure 3.11. Figure 3.11 shows the breakdown time as a function of benzene fill. The joule heating process lasts longer for small amounts of benzene. One cannot attribute this phenomenology directly to quenching effects since a more careful and controlled study needs to be done, but certainly there is a correlation between the lifetime of the number of carriers and benzene partial pressure.

The effects of benzene go beyond the initial laser ionization phase. Figure 3.12 show neon gas pre-pulse current waveforms for several benzene fills. Again quenching and recombination effects increase with benzene partial pressure. Ideally, given all the previous
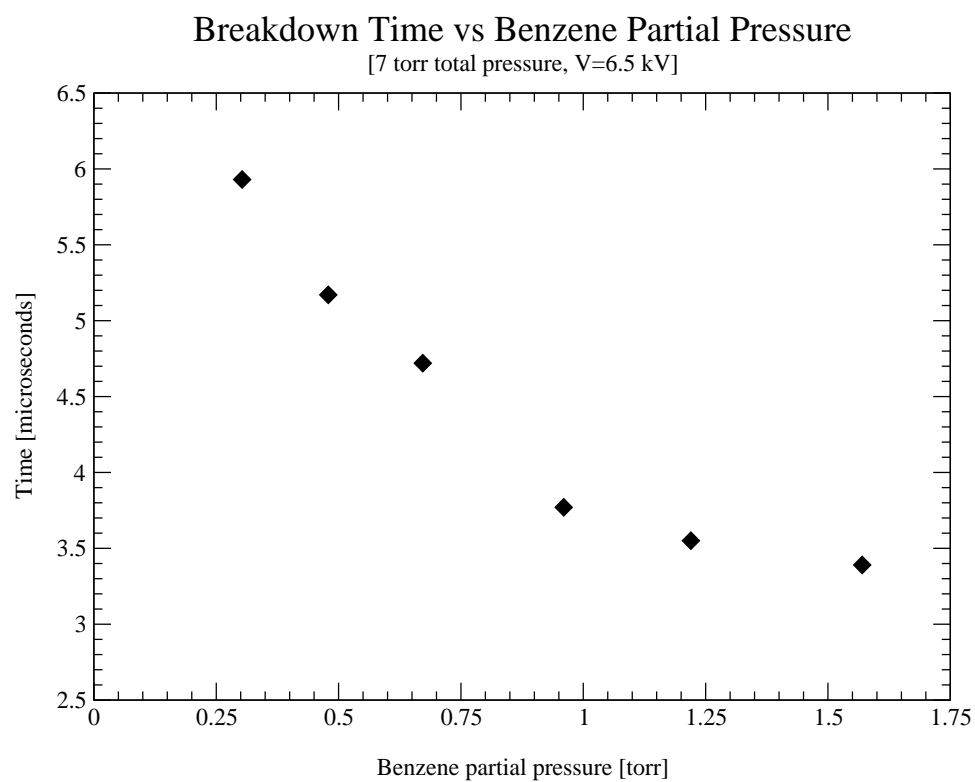
Figure 3.11: Time elapsed between ionizing laser pulse passage (joule heating period) and avalanche breakdown as a function of benzene concentration. Pre-pulse capacitor energy deposition rate depends on this initial period.
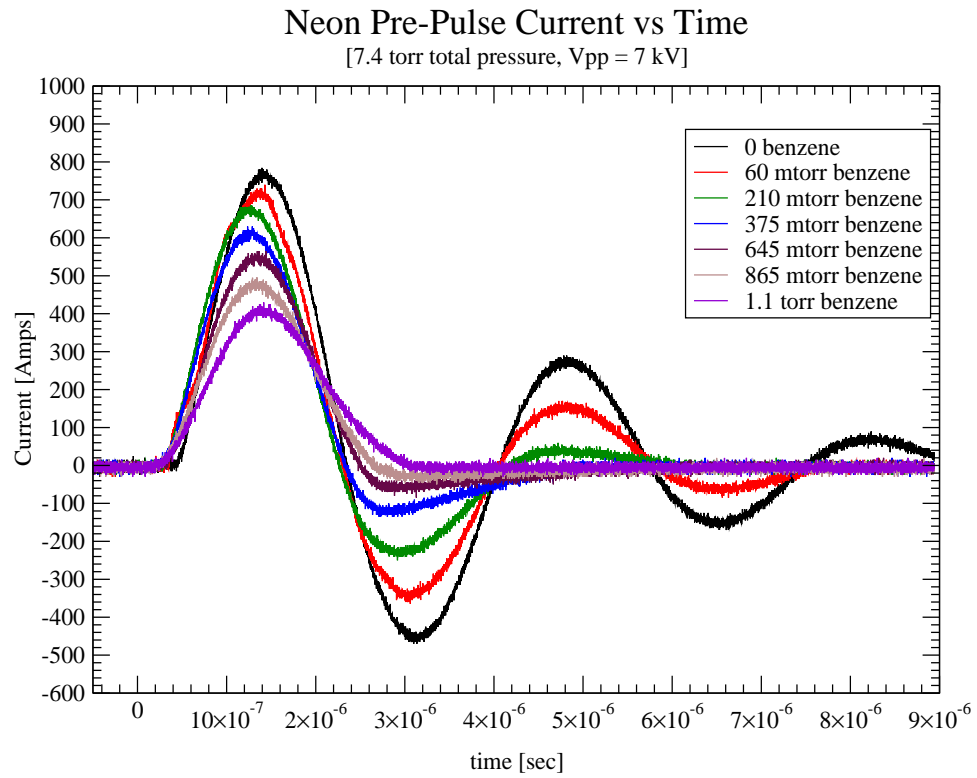
Figure 3.12: Effect of benzene on the current waveforms for a neon gas fill pre-pulse discharge. After breakdown, the pre-pulse current dampens faster as benzene pressure increases.

data, one would operate in the low benzene regime, say between $0.25\,\text{torr}$ to $0.50\,\text{torr}$. Nevertheless, since there is significant carbon chamber contamination with every main bank channel produced, there is a reduction in the chamber's voltage breakdown tolerance. To overcome this effect one needs to increase the amount of benzene since these are competing effects and current will flow in the path of least resistance. This becomes a vicious circle. The more benzene added, the more carbon produced. This reaches a point where it is close to impossible to produce anymore channels. At this point one has to tear down the chamber and remove all carbon deposits. A better and cleaner experiment would be carried out with a monoatomic gas with no additives. This set up would simplify the underlying physics significantly and would provide for simpler experimental interpretation. Hence the idea of using a high power laser in a noble gas. The approach used at GIS, CO_2 laser beam tunned to a resonant frequency of ammonia is also good. In this case there is no shot-to-shot degradation of channel production and no buffer gas effects [71]. This would provide for a clean experiment that would provide for easy physical interpretation of the phenomena occurring during channel production. On the other hand, this simple study on benzene sheds some light into the possible complications that a mixture of xenon-FLiBe may introduce. A plasma channel study on xenon-FLiBe would be well worth doing.

Chapter 4

Diagnostics

The diagnostics used to probe and measure the plasma channel rely on the optical properties of the channel itself. Namely, the probe is an electromagnetic wave launched onto the plasma channel. This electromagnetic wave is typically in the optical frequency region of the spectrum. These techniques have been used and developed before [52] [38] [27] [38] [31], but now with the introduction of new technological improvements in digital imaging techniques, sensitivities can be pushed to new limits. A review of the physics of electromagnetic wave propagation in plasmas is given in appendix A.

4.1 Schlieren and Phase Contrast Imaging

It is expected that the rapid energy deposition during the pre-pulse discharge will produce a long lived ($\sim 30\,\mu$s) neutral gas density depression on axis. Based on preliminary light emission studies of the discharge [20], one expects this density depression produced by hydrodynamic expansion to be approximately $1\,$cm in diameter and the gas density ratios

between the background fill held at 7 torr and the on-axis depression to be about 10 to 1. Two techniques can be used to detect and measure the relative density profiles left by the pre-pulse discharge: schlieren and phase contrast imaging.

4.1.1 Schlieren

The schlieren technique relies on the transverse gradient of the index of refraction associated with the neutral gas density gradients [21] [29]. If one propagates a probe beam through the gas disturbance, one can image the density gradients. The typical set up for our experiment is shown in figure 4.1. It consists of a 3 mJ pulsed Nd:YAG laser with $\lambda = 1064\,$nm, a 10 ns pulse width, beam expander-collimator, 1000 mm focal length lens, knife edge, collection optics, and a Cohu 8 bit CCD camera. Originally, in the absence of the gas channel, the rays from the undisturbed probe incident plane wave are all parallel and are all blocked by the knife edge. When the collimated beam of light is bent by the gas channel, the deflected rays will move away from the beam stop (knife-edge) and produce an image onto the CCD camera. The disturbance acts as an extended body composed by point sources with origin at the plane of the pre-pulse channel. The CCD collection optics image the mid-plane of the pre-pulse channel onto the CCD chip. This particular set up takes advantage of the laser's short pulse to acquire the data with a 10 ns time resolution.

The vector differential equation describing light rays is [10]:

$$\frac{d}{ds}\left(n\frac{d\vec{r}}{ds}\right) = \nabla n \tag{4.1}$$

where $\vec{r}$ is the position vector of a typical point on a ray and s is the length parameterization of the ray and n the index of refraction. From equation (4.1) one can derive the familiar

SCHLIEREN SET UP

Figure 4.1: Diagram showing the schlieren imaging set up. The collimated beam is refracted by the gas density gradient of the channel. This refracted beam produces an image on the CCD camera of the gas disturbance.
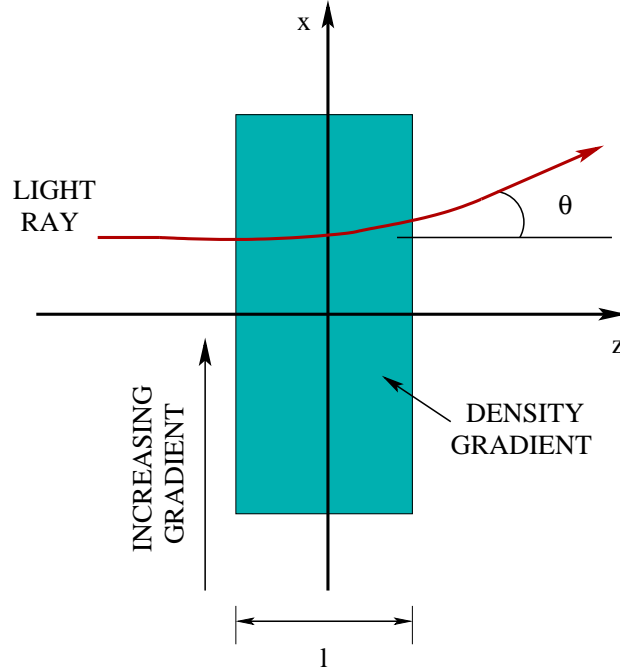
Figure 4.2: Diagram illustrating the deflection of a light ray as it transverses an optical medium with an index of refraction gradient.

angular ray displacement expression for a one dimensional density gradient [38] [29]:

$$\theta = \int_l \frac{1}{n}\left(\frac{dn}{dx}\right)dz \approx \frac{1}{n}\left(\frac{\Delta n}{\Delta x}\right)l \tag{4.2}$$

Here θ is the deflection angle in radians, l is the interaction length in the z direction, and n is the index of refraction assumed to vary very slowly with respect to z. A sketch of this geometry is shown in figure 4.2.

Unfortunately one cannot use equation (4.2) for a quantitative interpretation of the pre-pulse channel, since the index of refraction, through the gas density, is a function of both x and z. The only possible way to measure the density would be to measure the deflection of particular rays, but due to the cylindrical symmetry of the pre-pulse channel, these deflections can't be quantified. Hence, since all rays pass at least twice as the probe beam

transverses regions of different densities but similar density gradients, the channel deflects the rays by the corresponding angles picking up an accumulated contribution. Equation (4.2) will only be useful to determine sensitivities and establish design parameters for the set up of the schlieren instrument.

From equation (4.2) and (A.22) and the values from table A.1 we obtain:

$$\theta = \left(\frac{K_{\text{effective}}}{1 + \rho K_{\text{effective}}} \right) l \frac{\partial \rho}{\partial x} = 1.1 \times 10^{-23} l \frac{\partial N}{\partial x} \tag{4.3}$$

For $\Delta N \sim 10^{17} \, \text{cm}^{-3}$, $\Delta x \sim 1 \, \text{mm}$, and $l \sim 1 \, \text{cm}$, then we obtain $\theta \sim 10^{-5}$ radians. Considering that the ray will propagate through a distance of one meter from the channel to the focusing lens and one meter from the lens to the knife edge, as shown in figure 4.1, the ray will be displaced $\sim 10^{-5} \, \text{m}$ from the knife edge tip. This is enough to produce the desired image.

Figures 5.3 and 5.6 show images of the pre-pulse for two different pre-pulse capacitors and pre-pulse voltages. The information that one can extract is the qualitative understanding of the gas expansion through the mapping of the pre-pulse shockwave front's position as a function of time. From the images in figures 5.3 and 5.6 one can appreciate the uniform gas "wall" formed by the pre-pulse discharge.

4.1.2 Phase Contrast

Zernike's phase contrast technique relies on the phase shift that the electromagnetic plane wave receives from an optically thin or transparent object [10] [62]. This technique has been used extensively in biological microscopy. It offers several advantages over the traditional schlieren imaging technique. While the schlieren technique relies on the bent

light rays to clear a stop to form an image, the phase contrast technique utilizes both the background unrefracted light as well as the refracted beams [10]. Also the phase contrast method offers a much simpler quantitative interpretation of the produced image, this being that the intensity map is proportional to the phase change introduced by the disturbance object to the incident plane wave. The experimental set-up consists of the 514.5 nm line of a CW argon ion laser, necessary transport optics, phase mirror and a Kentek streak camera. A simple schematic of the experimental set up is shown in figure 4.3. The difference between the phase contrast set-up and the one for schlieren is only the phase mirror shown in detail in figure 4.4. The streak camera is used to obtain the time resolved images produced by the CW laser.

The principle on which this technique is based resides on the assumption that the object causing the refraction is completely optically transparent and it only introduces a small phase shift to the incident light ray. Let E_I be the incident monochromatic plane wave and E_T the phase shifted wave. Then one can write, for small phase shift ϕ:

$$E_T = E_I e^{i\phi} \approx E_I(1 + i\phi) = E_I + E_D \tag{4.4}$$

where $E_D = iE_I\phi$

One can think of the transmitted light passing through the disturbance as a wave with two components of amplitude E_I, e.i., one with the original phase of the incident undisturbed plane wave and another with a phase shift equal to $(\pi/2)\phi$. If one can advance or retard the phase of the unperturbed component by $(\pi/2)$ with respect to the perturbed light rays, then both disturbed and undisturbed rays would recombine to produce an image
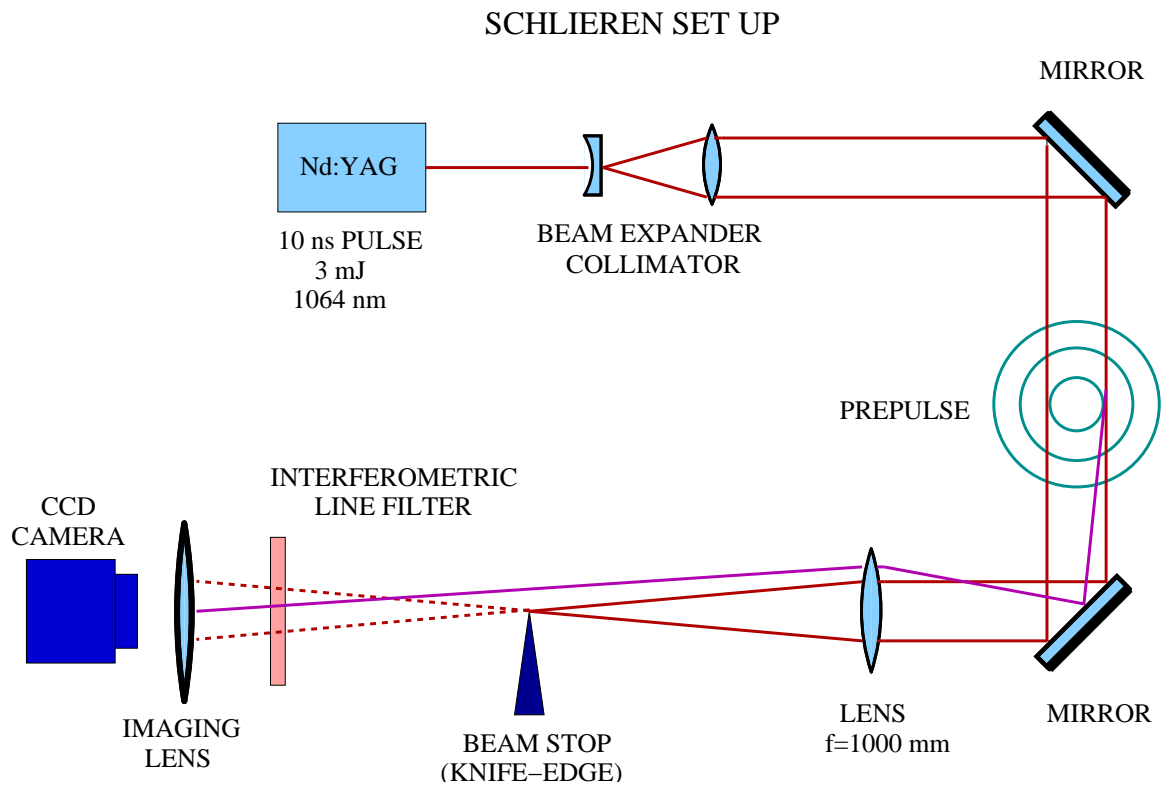
PHASE CONTRAST SET UP
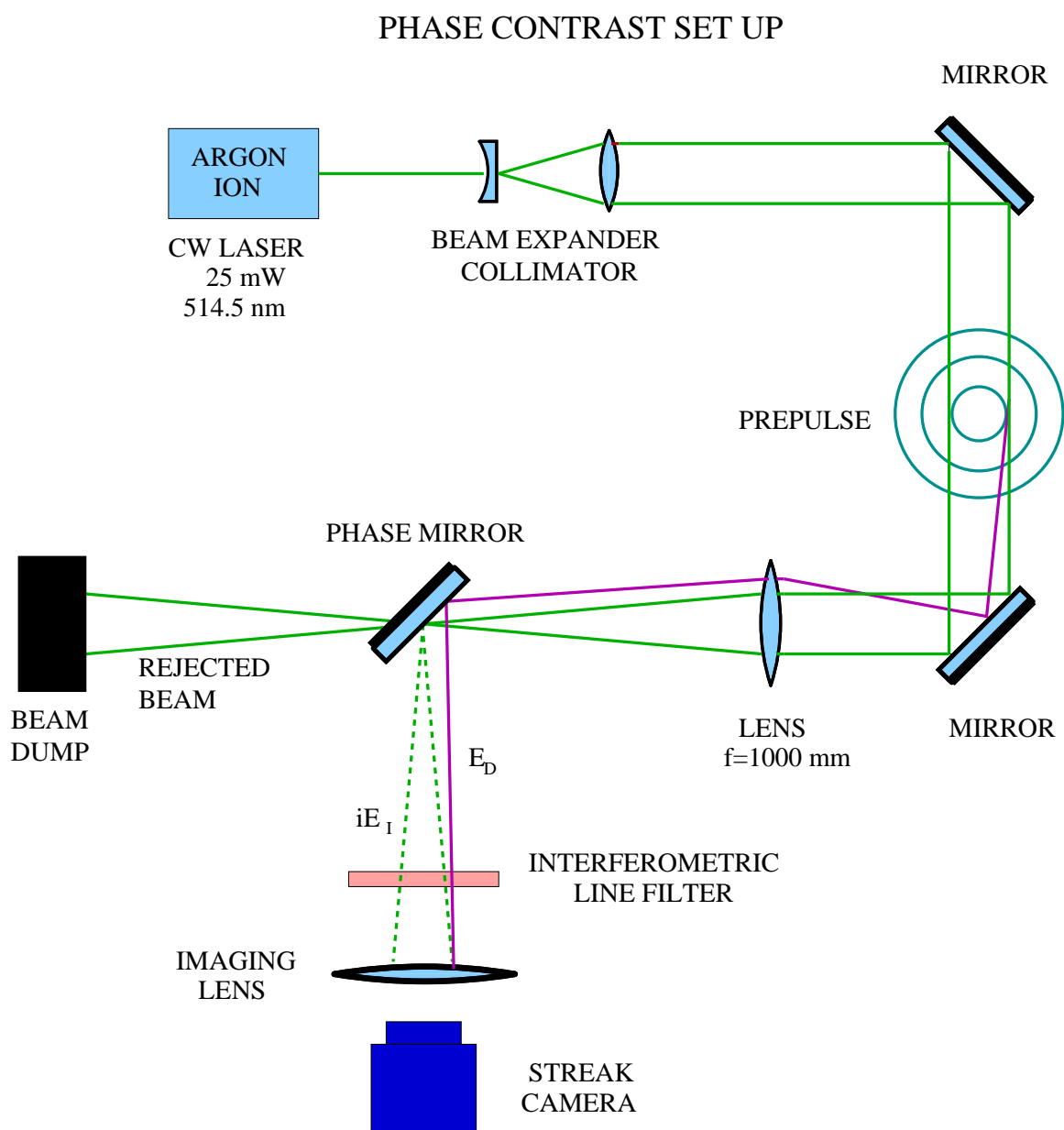
Figure 4.3: Diagram showing Zernike's phase contrast imaging set up. The collimated beam is refracted by the gas density gradient of the channel. This refracted beam is recombined with the unrefracted beam to produce an image of the gas disturbance on the streak camera.

proportional to the phase shift ϕ :

$$E_{image} = iE_I + E_D = iE_I(1 + \phi) \tag{4.5}$$

in terms of the intensity I, keeping only linear terms we have

$$I_{image} = E_{image} \cdot E_{image}^* = E_I^2(1 + 2\phi) \tag{4.6}$$

so from equation (4.6) we see that the image intensity is proportional to the phase shift introduced by the disturbance.

One can increase the contrast and optimize the sensitivity of the phase contrast instrument if one attenuates the undisturbed beam. Let $\alpha < 1$ be a positive real attenuation factor. Then we have:

$$E_{image} = i\alpha E_I + E_D = iE_I(\alpha + \phi) \tag{4.7}$$

$$I_{image} = E_{image} \cdot E_{image}^* = E_I^2(\alpha^2 + 2\alpha\phi + \phi^2) \tag{4.8}$$

from equation (4.8) we can compute the contrast C:

$$C = \frac{I_{image} - I_0}{I_0} = 2\frac{\phi}{\alpha} + \left(\frac{\phi}{\alpha}\right)^2 \approx 2\frac{\phi}{\alpha} \tag{4.9}$$

since $\phi << \alpha$ in our case. One can increase the contrast by making α smaller, e.i. we increase the attenuation. Typical reflectivities of uncoated optics for visible wavelengths are about 5%. Using dielectric anti-reflective coated optics one can reduce reflectivity to about 0.1%.

One can accomplish both the phase advance and attenuation of the incident unperturbed light beam by the proper construction of a phase mirror. A simple approach to the
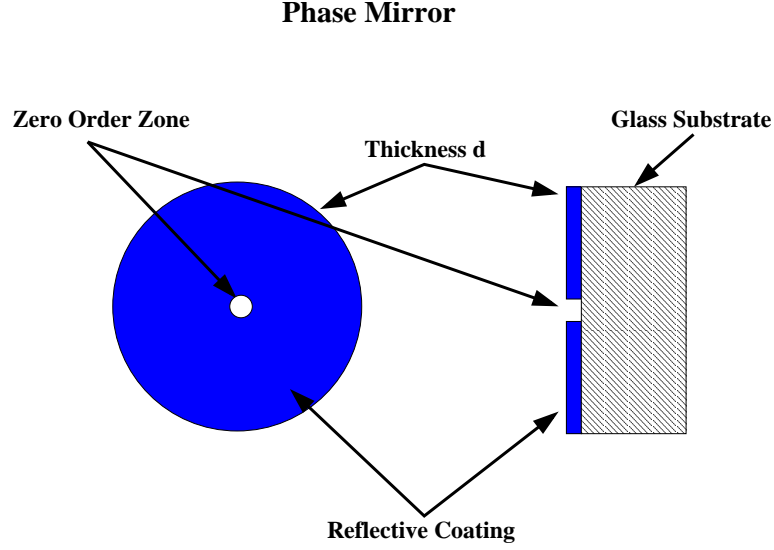
Phase Mirror

Figure 4.4: Diagram showing Zernike's phase contrast imaging mirror.

construction of this phase mirror is to take a dielectric AR coated glass substrate, masking a central region of a little more than the dimensions of the focused minimum spot size of the unrefracted probe beam, and applying a high reflectivity layer [62]. The thickness of the layer will depend on the working wavelength of the probing laser since the phase advance is inversely proportional to this wavelength:

$$\phi = \frac{2\pi}{\lambda}x = \frac{4\pi}{\lambda}d \tag{4.10}$$

where $2d = x$ according to figure 4.4. The thickness of the reflective layer is d and x the traversed path length. For $\phi = \pi/2$ corresponding to a phase retardation of a quarter of a cycle, one would obtain the thickness of the reflective layer:

$$d = \frac{\lambda}{8} \tag{4.11}$$

For $\lambda = 514.5\,\text{nm}$ we obtain a reflective layer thickness $d = 0.0643\,\mu\text{m}$. For our setup we

aluminum coated an optically polished fused silica substrate to the specified thickness and then ablated the zeroth order zone with a 1064 nm focused laser pulse.

For the case of the plasma channel experiment, the gas density depression of $\Delta N/N_0 \sim 1/10$ will produce a change in the index of refraction, according to the Gladstone-Dale relation, of 2.86×10^{-7} in nitrogen gas with $N_0 = 2.6 \times 10^{17} \, \mathrm{cm}^{-3}$. This corresponds to a phase shift of 3.49×10^{-2} radians for a laser probe wavelength of $\lambda = 515 \, \mathrm{nm}$ (Ar$^+$ laser). Considering a 5% reflectivity in the zeroth order zone of the phase mirror, we obtain a contrast $C \approx 1.5$. This contrast is sufficient to detect the pre-pulse gas density evolution.

4.2   Interferometry

Plasma electron densities were measured using a Michelson interferometer. A sketch of the apparatus is shown in figure 4.5.

Interferometry is a technique commonly used to measure plasma densities [52] [27] [38] since the plasma's index of refraction is a direct function of the plasma's electron density as it is seen in equation (A.21). The instrument in my experiment was set up to initially provide a null image consisting of a set of straight fringes in the absence of any significant electron density. The initial fringes are set by detuning one of the interferometer's mirrors. The interferometer provides a direct measurement of fringe shift induced by a change of the index of refraction created by the plasma. One uses an incident plane wave $\vec{E}$ as a probe:

$$\vec{E} = \vec{E}_0(t) \, e^{i\phi x} = \vec{E}_0(t) \, e^{ink_0 x} \tag{4.12}$$

with the phase ϕ given by

$$\phi(x) = k_0 \, n(x) \, x \tag{4.13}$$

MICHELSON TYPE INTERFEROMETER
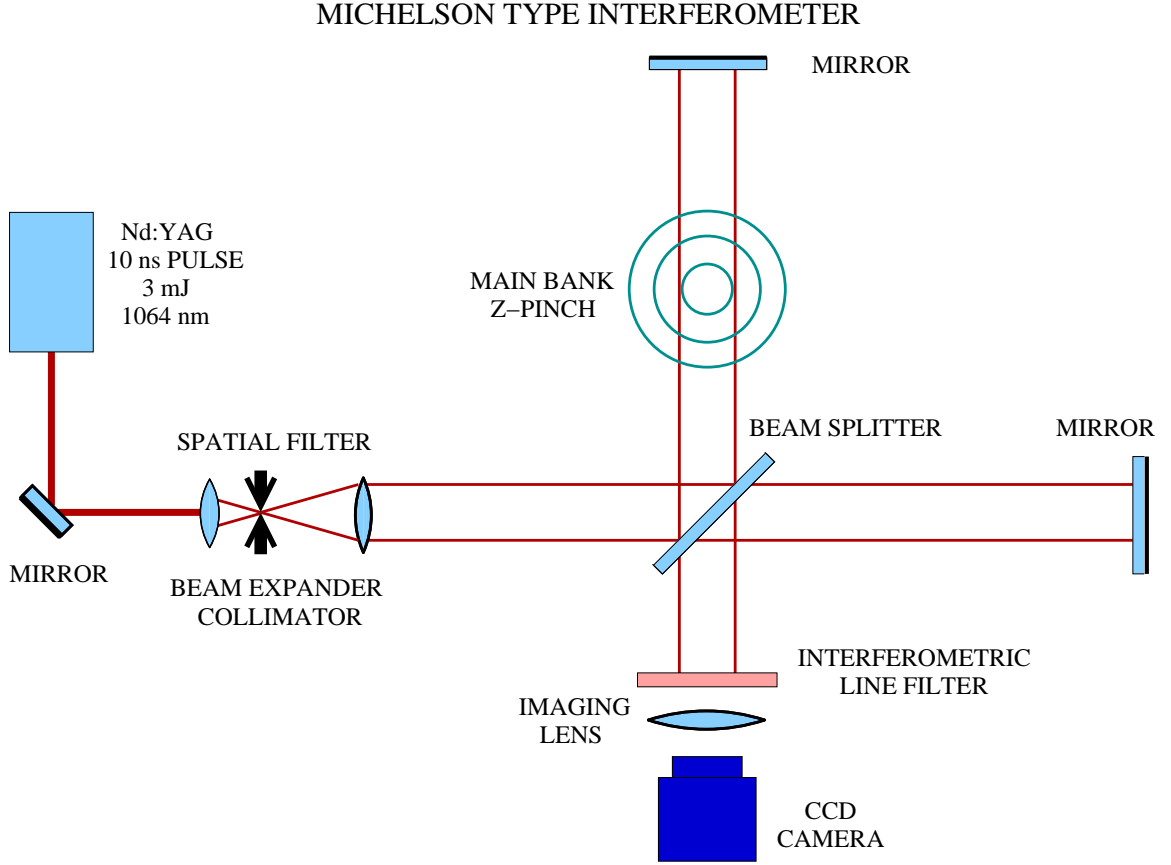
Figure 4.5: Diagram showing the Michelson interferometer set up. The collimated beam is passed through a beam splitter with one half beam is used to probe the plasma. This half beam is recombined with the half reference beam to produce an interference pattern that contains phase information directly related to the plasma electron density.

where $n(x)$ is the index of refraction, k_0 the vacuum probe laser wavenumber, and x the physical traversed path length. Here we are explicitly saying that the index of refraction $n(x)$ becomes a function of x once the probe beam transverses the plasma. We can re-write the phase in terms of the laser wavelength:

$$\phi(x) = \frac{2\pi}{\lambda_0}\, n(x)\, x \qquad (4.14)$$

So, for the case of our interferometer, the total phase shift of a plane wave

transversing a medium with a variable index of refraction is:

$$\Delta\phi = \frac{2\pi}{\lambda_0} \int_l n(x) \, dx \tag{4.15}$$

Using equation (A.21), we can write equation (4.15) as

$$\Delta\phi = -r_e\lambda_0 \int_l N(x) \, dx \tag{4.16}$$

where r_e is the classical electron radius. In terms of the fractional fringe shift K we write

$$\Delta K = -\frac{r_e\lambda_0}{2\pi} \int_l N(x) \, dx \tag{4.17}$$

From equation (4.17) we can immediately solve for the integral and get an integrated value of the electron density. In the case of the Michelson interferometer, one has to be careful to take into consideration that the accumulated fringe shift is produced by a double pass of the probe beam through the plasma. Hence, we pick up a factor of two so we have

$$\Delta K_{Michelson} = -\frac{r_e\lambda_0}{\pi} \int_l N(x) \, dx \tag{4.18}$$

where $\Delta K_{Michelson}$ in equation (4.18) indicates that this expression is only applicable for the double pass instrument.

With this in mind, in our case for example, with $\lambda_0 = 1\,\mu$m we obtain a integrated electron density of 1×10^{17} cm^{-2} per fringe shifted. The actual resolution of an interferogram is determined by the contrast between the bright and dark fringes and the CCD pixel resolution. The set up could resolve about one tenth of a fringe, corresponding to a minimum electron density detection resolution of about 1×10^{16} cm^{-2}.

Due to the cylindrical symmetry of the plasma channel, the electron density in reality is a function of (x, y) or, in cylindrical coordinates, (r) since the channel is assumed

azimuthally symmetric. A diagram of the geometry is shown in appendix B. This means
that when the probe beam transverses the plasma, the line integral in equation (4.18) is
carried out at a constant y. Then equation (4.18) becomes a version of Abel's integral (C.1)

$$K(y)_{Michelson} = -2 \frac{r_e \lambda_0}{\pi} \int_y^\infty \frac{N(r)}{\sqrt{r^2 - y^2}} \, r dr \qquad (4.19)$$

where the factor of 2 in the coefficient comes from doubling the integral value due to its
symmetry on the integrating limits. In practice the integral is not carried out to infinity
but rather to the radial distance where that plasma density falls off to zero[1]. This would
correspond to the region where fringe shift is unperceivable.

One can reproduce the electron density distribution $N(r)$ from the function $K(y)$
by inverting equation (4.19) using Abel's Inversion formula (C.2) [3] [58] [25] [78]. Then
equation (4.19) becomes

$$N_e(r) = \frac{1}{2 \, r_e \lambda_0} \int_R^\infty \frac{\frac{dK(y)}{dy}}{\sqrt{y^2 - r^2}} \, dy \qquad (4.20)$$

When comparing the integrated line density with the inverted density, one expects
a depressed profile of the electron density $N_e(r)$ and lower values about $r = 0$ since the
laser probe has a greater contribution to the line integral when the probe beam passes
through the core of the channel. The probe beam defines a chord through the cylindrically
symmetric plasma. One can see this effect from the example shown in appendix C.

4.3   Faraday Effect Polarimetry

The LBNL Faraday rotation polarimeter is designed to make an indirect measure-
ment of the azimuthal magnetic field produced by the plasma channel. This is accomplished

[1]see appendix C

by probing the plasma channel with a linearly polarized laser beam and measuring the polarization rotation utilizing the so called half-shadow angle technique [18] [46] that I'll explain in more detail later. The raw data generated by the polarimeter is a map of the total polarization's angle of rotation generated by the plasma's magnetic field as a function of the projection variable x transversed by the probe beam. The rotation is caused by the faraday effect of the magnetized plasma when the electromagnetic wave propagates through it [15] [38] [18] [31]. Here the probing laser beam crosses through the channel defining a chord. This chord integrates the product of the electron plasma density and the magnetic field's parallel component to the laser probe $\vec{k}$ vector over its interaction path length. The total angle measured by the polarimeter at the probe point depends on the difference between the optical path length traversed by the two circularly polarized components defined in section 4.1.2. This angle is

$$d\theta = \frac{1}{2}\left(k_+ - k_-\right)\ dl \tag{4.21}$$

where the $k_\pm$ wavenumber expressions are given in equation (A.17). Here we anticipate that the only contributions to the polarization rotation is due to components of $\vec{B} \parallel \vec{k}$. Hence, assuming $\omega >> \omega_p >> \omega_c$, we have [38]

$$d\theta = \frac{1}{2\pi}\ \frac{r_e^2\lambda^2}{e}\ N(x,y)\vec{B}(x,y)\cdot d\vec{l} \tag{4.22}$$

or in integral scalar form

$$\theta(y) = \frac{1}{2\pi}\ \frac{r_e^2\lambda^2}{e}\ \int B(x,y)N(x,y)\cos(\phi(x,y))dx \tag{4.23}$$

where $\phi = \phi(x,y)$ is the projection angle between $\vec{B}$ and $d\vec{l}$. A diagram of the geometry is shown in figure B.1. To obtain a function for the magnetic field $\vec{B}$ we need to deconvolve

equation (4.23) using a similar technique as we did for the interferometric data for the electron density. Here we start of with the expression for the rotation angle $\theta(y)$, which is the function generated by the experimental data. Combining the constant coefficients into a lumped constant A we have

$$\theta(y) = A\,\lambda^2 \int_0^\infty B(x,y)n_e(x,y)\cos(\phi(x,y))dx \tag{4.24}$$

When λ is in microns, $B(x,y)$ in Teslas, $n_e(x,y)$ in cm^{-3} and the integration is carried out in centimeters, we find $A = 2.63 \times 10^{-21}$ T^{-1}.

We can transform equation (4.24) into polar coordinates yielding [2]

$$\theta(y) = A\,\lambda^2 \int_y^\infty \frac{B(r)n_e(r)\cos(\phi(r))}{\sqrt{r^2-y^2}}\,rdr \tag{4.25}$$

Using equation (B.1) we can re-write equation (4.25) as

$$\theta(y) = A\,\lambda^2 \int_y^\infty \frac{B(r)n_e(r)\frac{y}{r}}{\sqrt{r^2-y^2}}\,rdr \tag{4.26}$$

Since the variable y is a constant as far as the integral is concerned, we can divide both sides of equation (4.26) by y defining the new function $\Theta(y)$

$$\Theta(y) = \frac{\theta(y)}{y} = A\,\lambda^2 \int_y^\infty \frac{\frac{B(r)n_e(r)}{r}}{\sqrt{r^2-y^2}}\,rdr \tag{4.27}$$

Comparing equations (4.27) and (C.1) we can define the function $F(r)$ as

$$F(r) = A\,\lambda^2 \frac{B(r)n_e(r)}{r} \tag{4.28}$$

Now it is straight forward to apply Abel's inversion (C.2)

$$F(r) = -\frac{1}{\pi} \int_y^\infty \frac{\frac{d\Theta(y)}{dy}}{\sqrt{y^2-r^2}}\,dy \tag{4.29}$$

[2]see appendix B

and the magnetic field can be extracted by solving for $B(r)$

$$B(r) = \frac{F(r)}{A\,\lambda^2\ n_e(r)}\ r \tag{4.30}$$

There are a couple of subtle points. Abel's inversion requires an axis-symmetric function with a zero derivative at the origin. $\theta(y)$ by itself *does not* satisfy both of these conditions, but $\Theta(y)$ *does*. $\theta(y)$ is the convolution of $\vec{B}$ and N_e with $\vec{B}$ being the odd function with point symmetry about the origin. The function $1/y$ converts the function $\theta(y)$ into an even function. With this in mind we can go one step further. If we assume that the channel's current distribution is indeed uniform, we expect that $\vec{B}(r) = B_0 \frac{r}{R}\ \hat{\theta}$ inside the channel where it is obvious that B_0 is the maximum value of the magnetic field at the maximum channel radius R. This would imply that

$$\frac{B(r)}{r} = \frac{F(r)}{A\,\lambda^2\ n_e(r)} = constant = \frac{B_0}{R} \tag{4.31}$$

Hence it is reasonable to expect the function $F(r)$ to resemble the electron density distribution. Taking this analysis one step further, we can determine the enclosed channel current, $I_{enclosed}$, by computing the function rB_θ

$$I_{enclosed} \propto rB_\theta(r) = \frac{r^2\ F(r)}{A\,\lambda^2\ n_e(r)} \tag{4.32}$$

knowing the total discharge current, a plot generated with equation (4.32) will give the fractional current enclosed by the channel.

An schematic for the experimental set up is presented in figure 4.6. It consists of a 30 W CW CO_2 laser with a cavity tuned at 10.6 μm with a linear polarized output beam. A high power electrooptical effect shutter is used to reduce the CW exposure to the detectors and reduce their thermal load. Various brewster window polarizers are used. The

FARADAY ROTATION POLARIMETER

CO2

30 Watt CW
10.6 μm
LINEAR
POLARIZATION
400:1

OPTICAL SHUTTER

LASER PULSE TRAIN
AFTER SHUTTER

BREWSTER POLARIZER
(POLARIZATION FILTER)

MIRROR

MAIN BANK
Z–PINCH

MIRROR

HgCdTe
FAST DETECTOR

BEAM SPLITTER

ANALYZER

IMAGING
LENS

V1

AMPLIFIER

ANALYZER

IMAGING
LENS

V1–V2
TO OSCILLOSCOPE

V2

HgCdTe
FAST DETECTOR
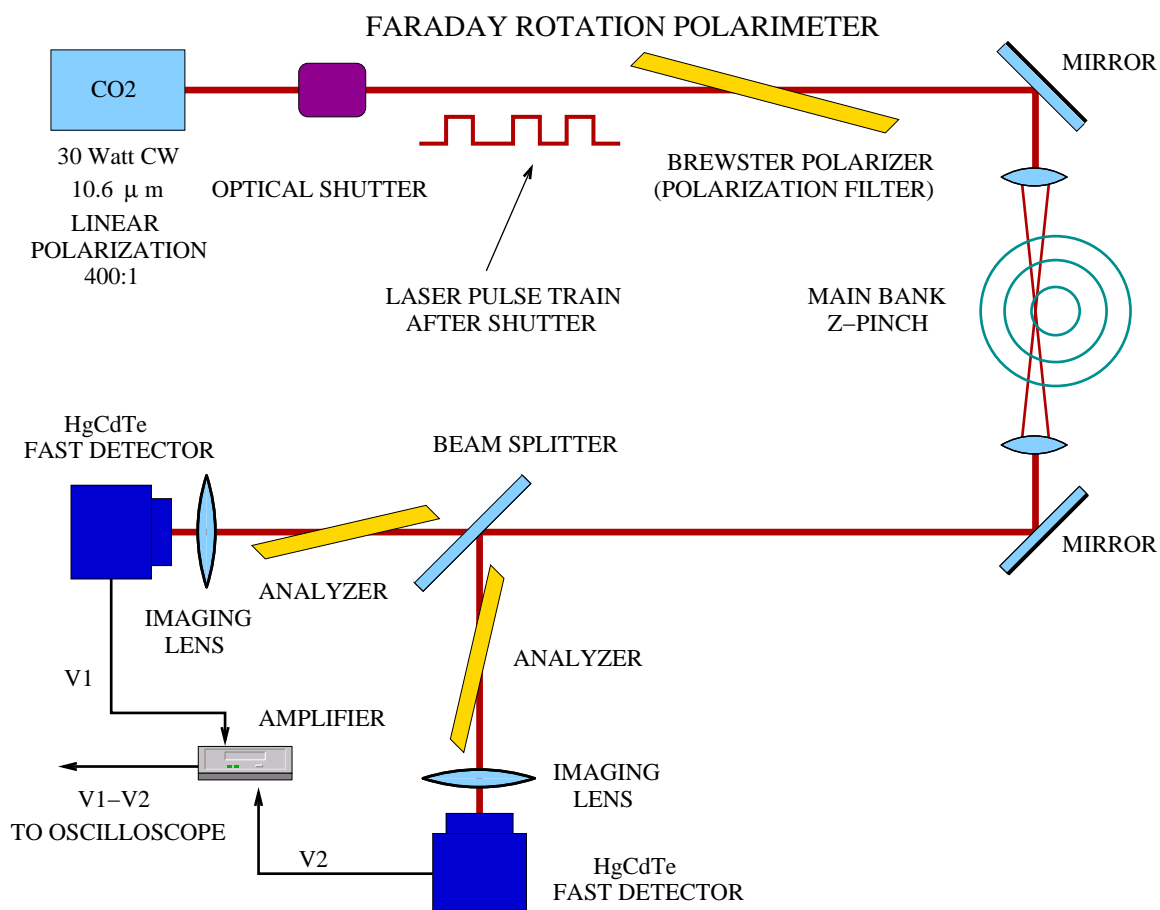
Figure 4.6: Diagram showing the Faraday effect polarimeter set up. The linear polarization of the beam is rotated by the channel through the difference in the beam's propagation speed of the ordinary and extraordinary induced in the plasma by the channel's magnetic field. The diagram shows the use of the half shadow angle technique were the subtraction of measured signals is used to increase sensitivity.

first polarizer is used to filter out any non-desired polarized components. The other two polarizers are used as analyzers just before the detectors. The detectors are fast mercury-cadmium-telluride (HgCdTe) detectors obtained from VIGO industries in Poland. As for the half shadow angle technique, this can be traced to Falconer [18]. The technique consists on splitting 50-50 the polarization rotated beam and passing each sub-beam through two separate polarization analyzers that are set at the so called half shadow angle χ. One of the two analyzers is set to $+\chi$ while the other to $-\chi$ with respect to the incoming unrotated polarized probe beam. Each split beam falls upon a fast mercury cadmium telluride detector that sends its response signal to a subtracting amplifier. The polarimeter is calibrated to the condition of zero difference of the two detector signals, $V_1 - V_2$, when there is no polarization rotation. Upon polarization rotation, one detector will see a larger signal –the beam's polarization is rotating toward the principal axis of the first analyzer– while the other detector sees a smaller signal –the beam's polarization is rotating away from the principal axis of the second analyzer– thus doubling the instrument's sensitivity.

To find out the performance of the interferometer we can put numerical values to equation (4.26). For $\lambda = 10.6\,\mu$m we have

$$\theta(y) = 2.955 \times 10^{-19}\, y \int_y^\infty \frac{B(r)n_e(r)}{\sqrt{r^2 - y^2}}\, dr \tag{4.33}$$

with $B(r)$ in Teslas and n_e in cm^{-3}.

The following analysis will show the expected results from the experiment. If we choose to take a uniform current density distribution totaling $50\,$kA and confined completely within the limits of $1\,$cm radius of the plasma channel, we obtain the magnetic field distribution shown in figure 4.7. Suppose that the electron density distribution within the

Magnetic Field for a Uniformly Distributed Current Density

Plasma Channel assumed to be bound at r=1 cm, B0=1 Tesla
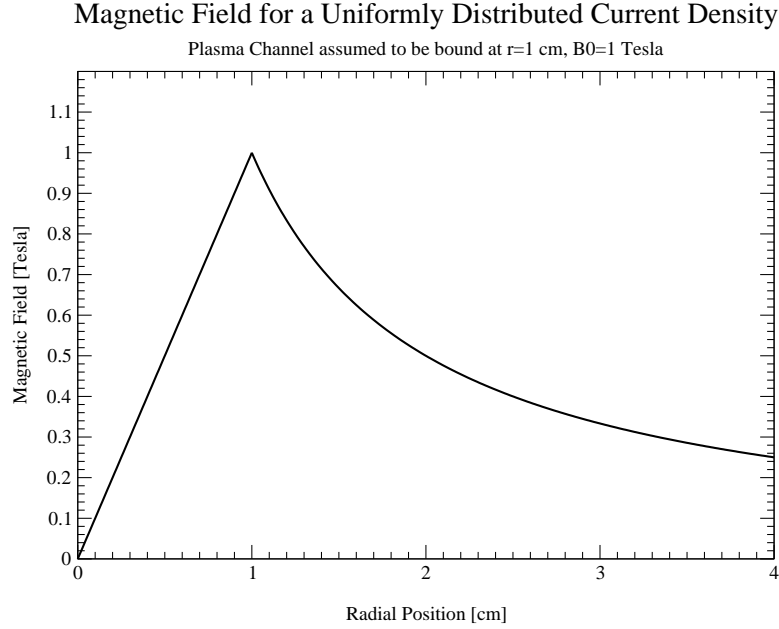
Figure 4.7: Plot showing the magnetic field for a $50\,\mathrm{kA}$ uniformly distributed channel current

plasma channel is characterized by a Gaussian with peak electron density of $1.5 \times 10^{17}\,\mathrm{cm}^3$

as shown in figure 4.8, then the total probe beam polarization rotation as a function of radial

position can be computed with equation (4.33). The resultant plot is shown in figure 4.9.

We see that the expected maximum rotation is about 0.009 radians or about 0.5 degrees. In

order to define any current distributions by direct measurement of the rotation angle, the

instrument should be able to resolve 0.01 degrees or less (~ 0.0002 radians). We use the

calibration plot shown in figure 4.10 in order to determine the polarization rotation of the

probe beam as it transverses the plasma since the measurement is made from the difference

of the detector electrical signals $V1 - V2$. It is important to keep in mind that this rota-

tion value corresponds to the maximum convolution values of magnetic field and electron

density, hence setting an expected upper bound on the possible measurable signals in the

plasma channel experiment. There are other limiting factors such as the noise floor of the

Mock Electron Density Distribution to Estimate Faraday Rotation

Peak value based on experimental data
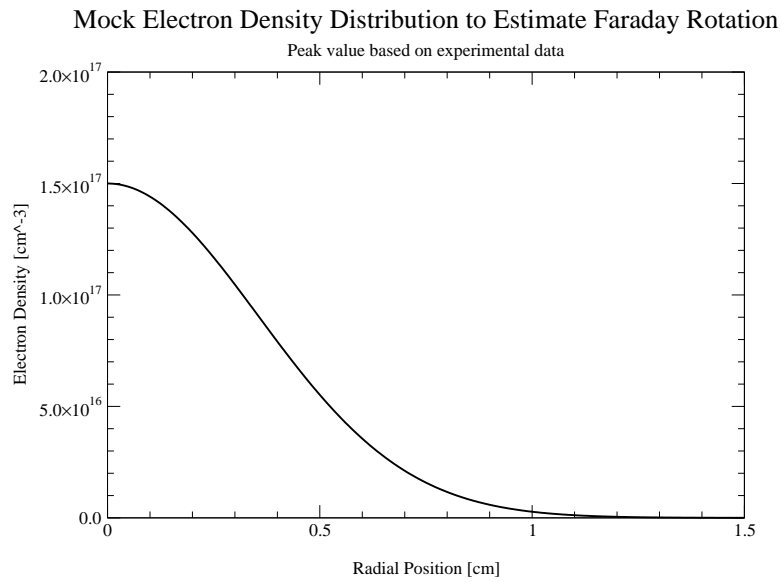
Figure 4.8: Mock electron density distribution used to estimate the faraday rotation effect. Peak value is based on experimental results.

Expected Polarization Rotation Angle

Uniform J=15.9 kA/cm2 (50 kA discharge) Ne peak=1.5x10^17 cm-3
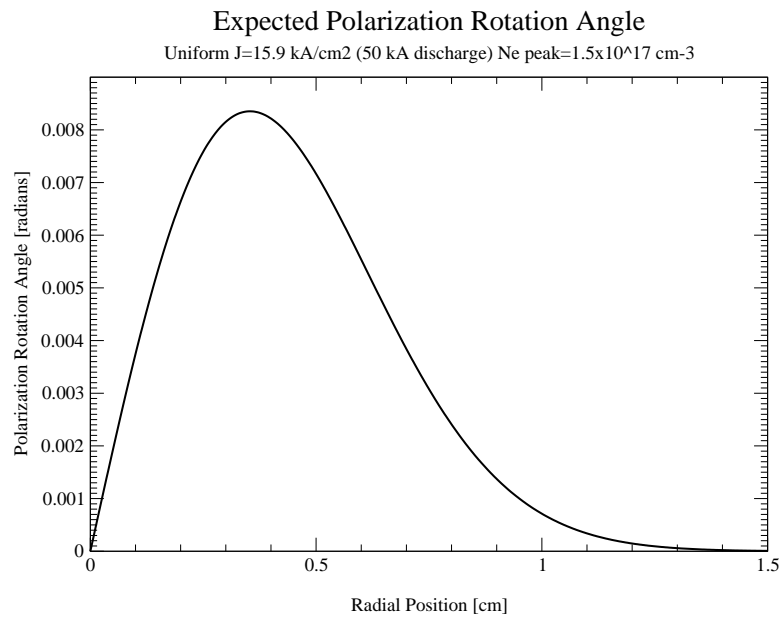
Figure 4.9: Polarization rotation induced by a plasma channel with a $50\,\mathrm{kA}$ uniformly distributed channel current with the magnetic field shown in figure 4.7 and $1.5 \times 10^{17}\,\mathrm{cm}^{-3}$ peak electron density having the distribution shown in figure 4.8
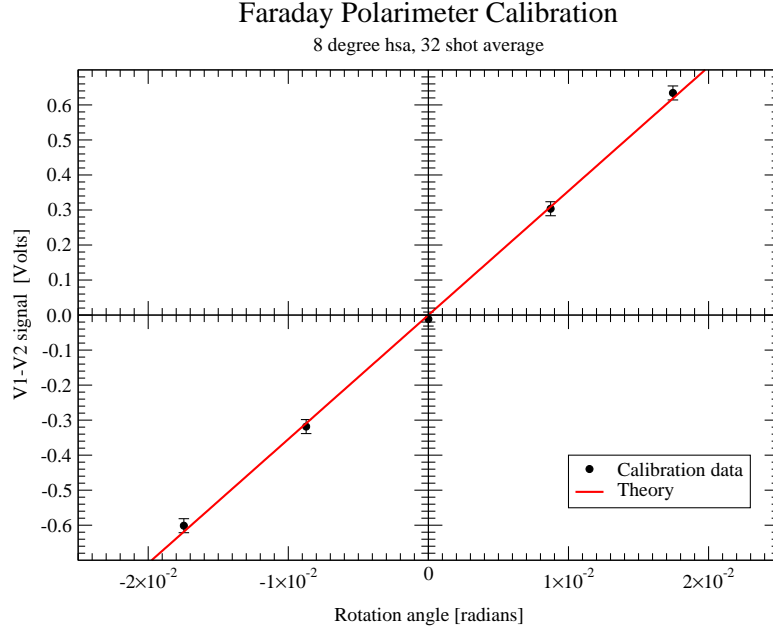
Figure 4.10: Calibration plot for the Faraday effect polarimeter. Amplified signal measured has a gain of 10.

instrument. Figures 4.12, 4.13, and 4.14 shows some of the noise characteristics. This gives a total uncertainty in the measurement of $\pm$ 0.002 radians for all measurements independent of the channel's repeatability. Further limitations are imposed by the refraction effect of the channel on the probe beam and by the shot-to-shot channel's statistics. Compensation optics were introduced immediately before the HgCdTe detectors and quantification of the beam deflection effects were made. The results are shown in figure 4.11. The statistical noise effects due to the electric coupling of the discharge and the intrinsic amplifier noise are shown in figures 4.12, 4.13, and 4.14.

The data collection techniques include the collection of the $V_1 - V_2$ signal, $V_1 + V_2$ signal, and the channel shots with no analyzer signal to account and subtract any systematic errors incurred by either deflection or broadband infrared radiation generated by the plasma.
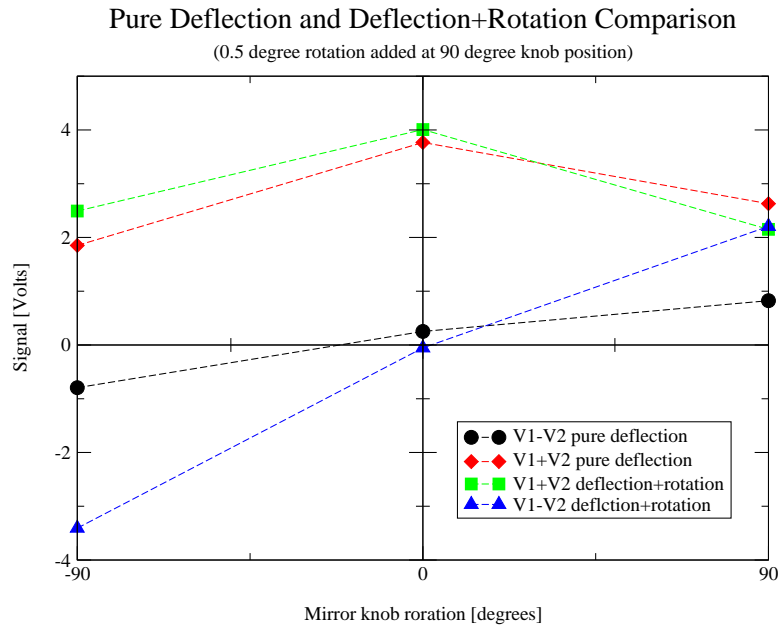
Figure 4.11: Faraday effect polarimeter probe beam deflection due to plasma refraction
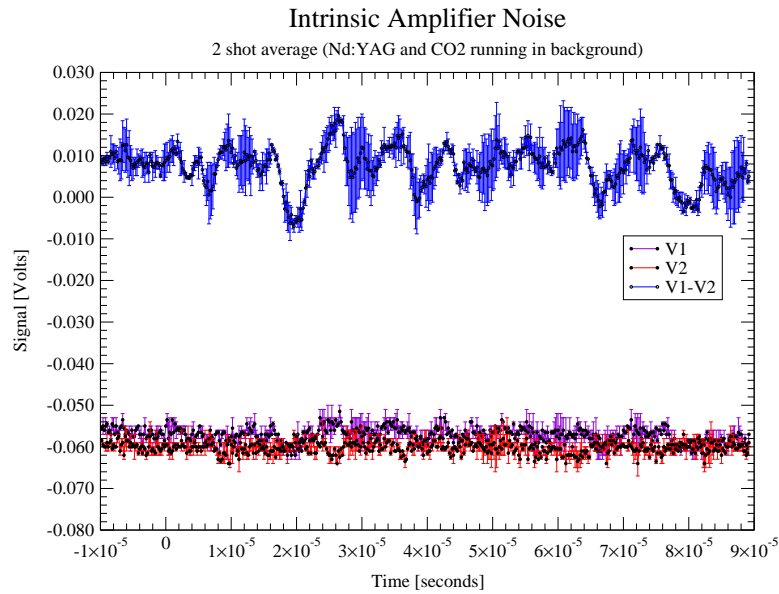
Figure 4.12: Faraday effect polarimeter electronic amplifier intrinsic noise.
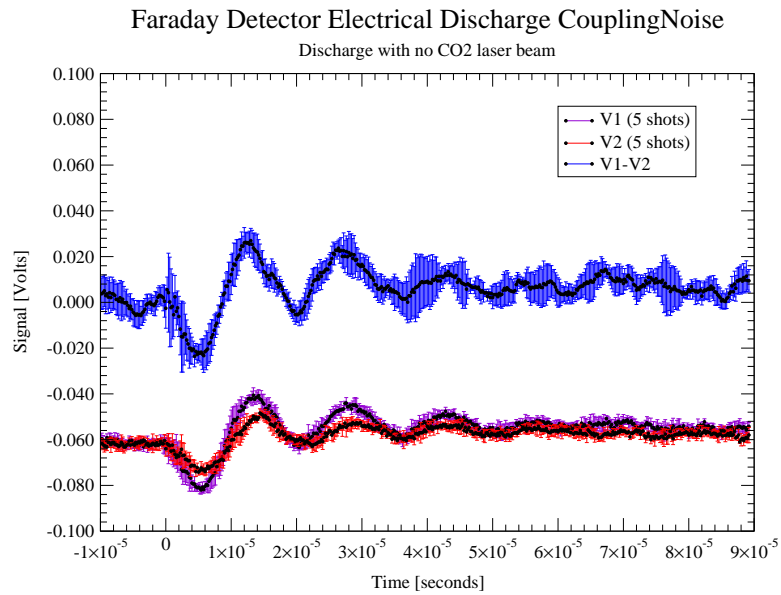
Figure 4.13: Faraday effect polarimeter electrical discharge coupling noise
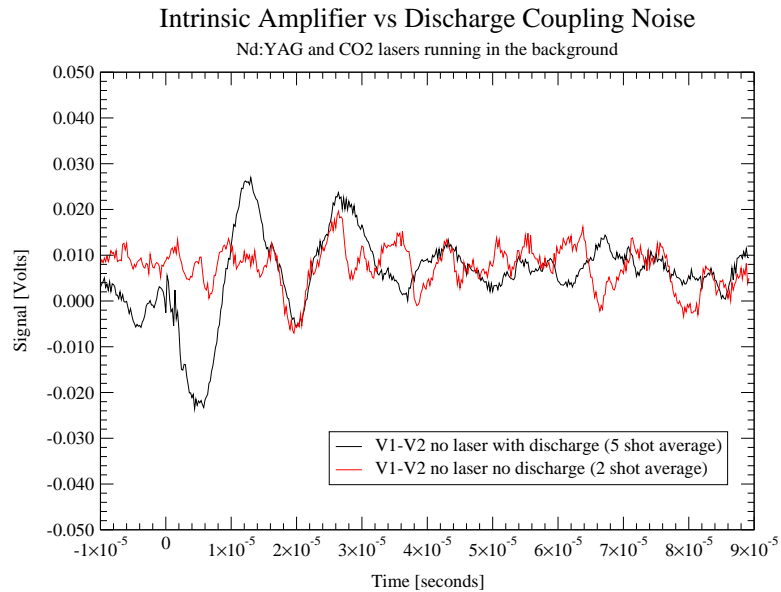
Figure 4.14: Comparison of intrinsic noise with discharge coupling noise. With aid of figure 4.10 the minimum faraday rotation measurable is 0.002 radians.

Chapter 5

Experimental Results

The results from a series of experiments aimed to characterize the z-pinch plasma channel conducted at LBNL are presented here. They mainly address the questions and concerns about repeatability, channel uniformity, and electrical current distribution. In this chapter I will attempt to quantify as much as possible the critical parameters necessary for code bench marking. In addition, when possible, pertinent conclusions about the channel will be set forth based on the evidence presented. I will reserve this chapter exclusively to the experimental analysis and its presentation. In chapter 6 I will make the appropriate comparisons of experiment with theory.

The control parameter space for the experiments include pressure, gas species, discharge voltage, and discharge capacitance. It was observed that there is a particular window of this parameter space for which the combination of pre-pulse and main bank discharges occurred consistently. The typical parameter set up consisted of $7\,\text{torr}$ of nitrogen, $0.5\,\text{torr}$ of benzene, $7\,\text{kV}$ pre-pulse voltage, and $15\,\text{kV}$ to $25\,\text{kV}$ main bank voltage.

5.1 Pre-Pulse

As mentioned previously, the main bank discharge z-pinch column's enhanced stability is due in great part by the introduction of the pre-pulse discharge. Exactly what conditions are left by the pre-pulse for the main bank channel are part of this investigation to determine. The tools used here were schlieren and phase contrast imaging techniques. In conjunction both tests proved useful in determining both the spatial uniformity of the pre-pulse channel as well as its time evolution. The observed feature was the expansion of the shock wave produced by the pre-pulse discharge.

One of the possible parameters to control for z-pinch optimization is the initial gas depression diameter footprint created by the pre-pulse. The final gas depression left behind by the pre-pulse will in part determine the main bank pinch time. Other parameters on which the pinch time depends on are the gas species mass and the discharge current. Knowing and understanding the pre-pulse evolution and the gas footprint left to the main bank is critical to controlling the main discharge.

5.1.1 Voltage and Current Waveforms

The initial and easiest parameters to monitor are the applied pre-pulse voltage and current. Two examples of these traces are shown in figures 5.1 and 5.2 showing the dependence of the joule heating period on the benzene as was discussed in section 3.2.4. The initial five to twenty microseconds correspond to the resistive phase of the pre-pulse where initial joule heating occurs. Once the proper $\vec{E}/P$ condition is met, avalanching occurs. In particular, the effect of the added benzene is to provide a reduced resistive path facilitating

Pre-pulse Voltage and Current Waveforms

7 torr nitrogen, 0.5 torr benzene
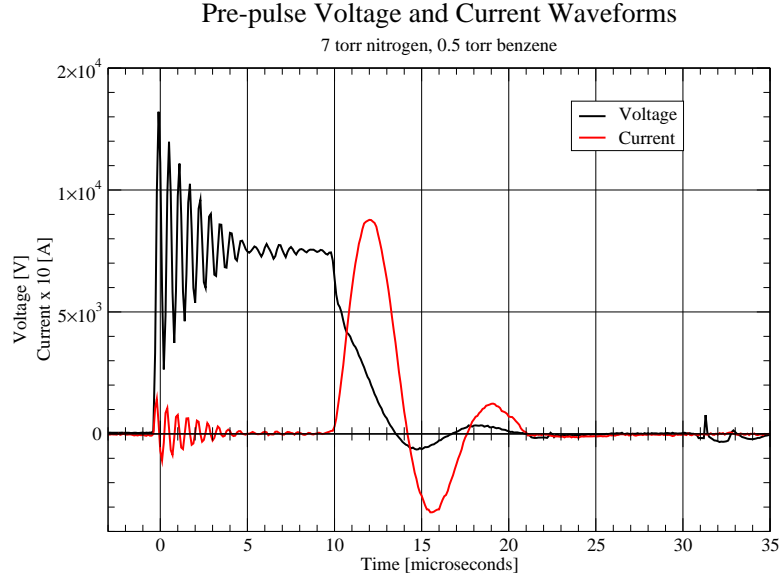
Figure 5.1: Pre-pulse voltage and current waveforms 7 torr nitrogen, 0.5 torr benzene,7.5 kV discharge. The high frequency oscillations are due to the coupling to the main bank pulser.

the I^2R effect. The high frequency oscillations in figures 5.1 and 5.2 correspond to the LC coupling between the channel chamber and the main bank pulser.

5.1.2 Schlieren

The schlieren set up proved to be beneficial due to its ability to obtain time resolved snapshots from the expansion shock wave produced by the pre-pulse. The time resolution is given by the pulsed probe laser with a 10 ns pulse width. Examples of these snapshots are presented in figures 5.3 and 5.6.

The characteristic that becomes apparent immediately from these pictures is the uniformity of the shock fronts parallel to the path defined by the initial ionizing laser. This immediately suggest that the energy of the capacitor is deposited uniformly along the channels axis. This is a remarkable fact given that the discharge electron flow is initiated at
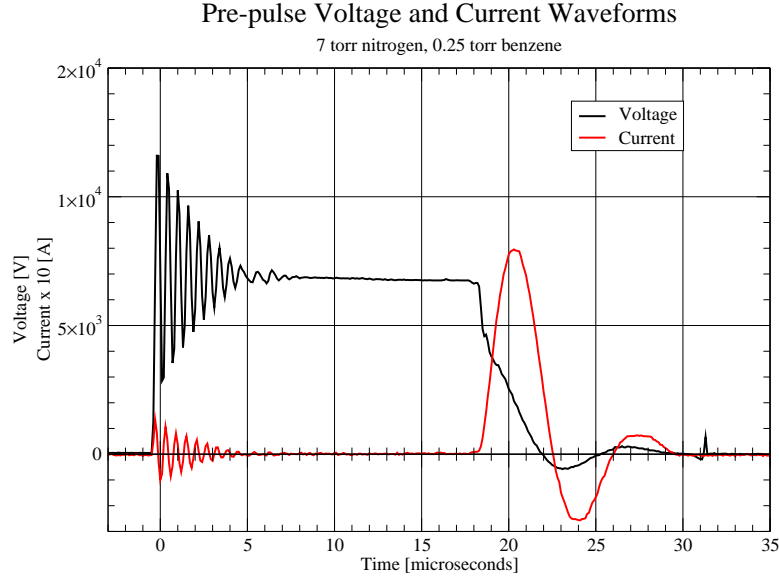
Figure 5.2: Pre-pulse voltage and current waveforms 7 torr nitrogen, 0.25 torr benzene, 7.5 kV discharge. The high frequency oscillations are due to the coupling to the main bank pulser. Notice the longer joule heating period compared to figure 5.1

the cathode, i.e. current is initiated at one end of the chamber, and one would expect to see a faster expansion at one of the ends of the channel producing a tapered front. Hence the uniformity of the shock front supports and validates the joule heating-avalanche hypothesis. Upon the passage of the ionizing laser there is a residual amount of uniformly distributed free electrons along the z axis, that with the application of the pre-pulse voltage the electric field $\vec{E}_z$ along the channel's axis accelerates these free electrons to produce the initial joule heating. The joule heating current is uniform along the channel path. The kinetic energy distribution of the free electrons shift to the point where electron avalanching takes place. Like the heating current, the avalanche process is uniform and the total energy deposition is uniform along the z axis as well.

Figures 5.4 and 5.7 show the shock front profile for different times as it is detected by the schlieren instrument. One has to remember that the instrument is only sensitive to

0.7 μsec

1.1 μsec

1.6 μsec

1.9 μsec

6.7 μsec
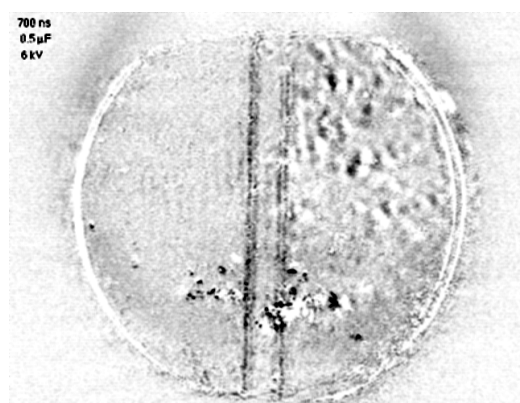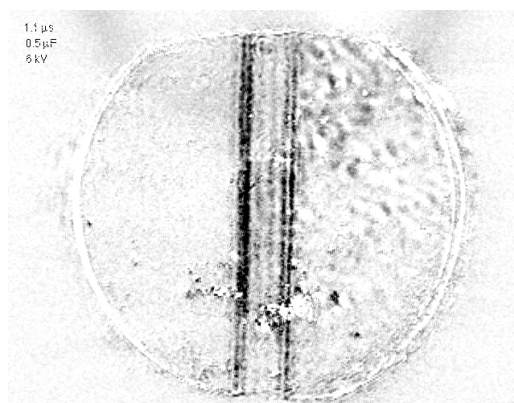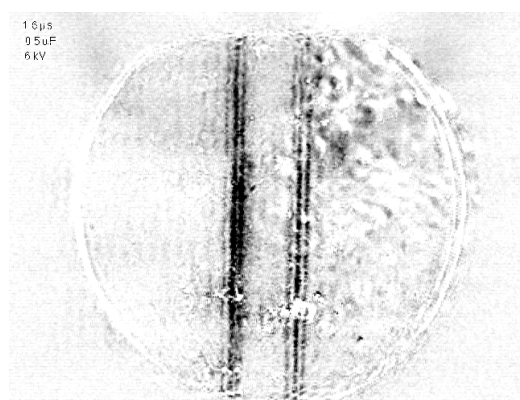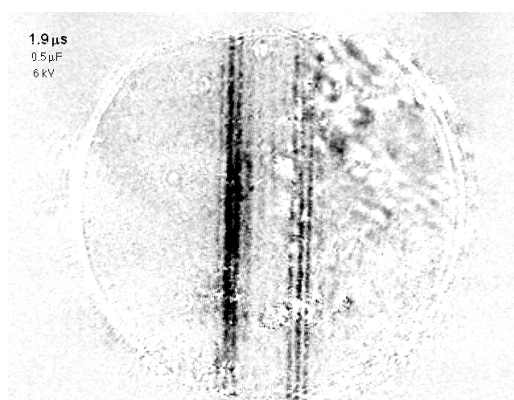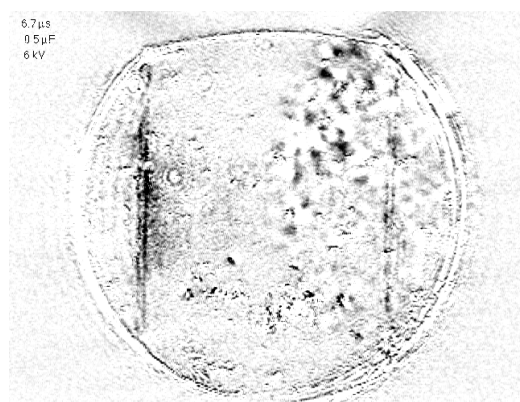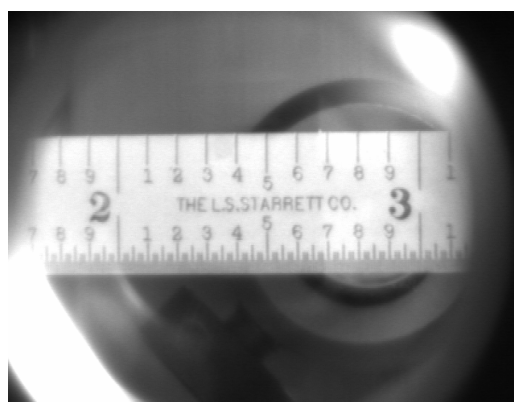
Field of View

Figure 5.3: Time resolved schlieren images of a 6.0 kV pre-pulse nitrogen discharge. Discharge parameters $C = 0.5\,\mu\mathrm{F}$, 7 torr N_2. The dark blotches on the pictures are carbon residues from benzene breakdown.

6.0 kV nitrogen Pre–pulse Discharge
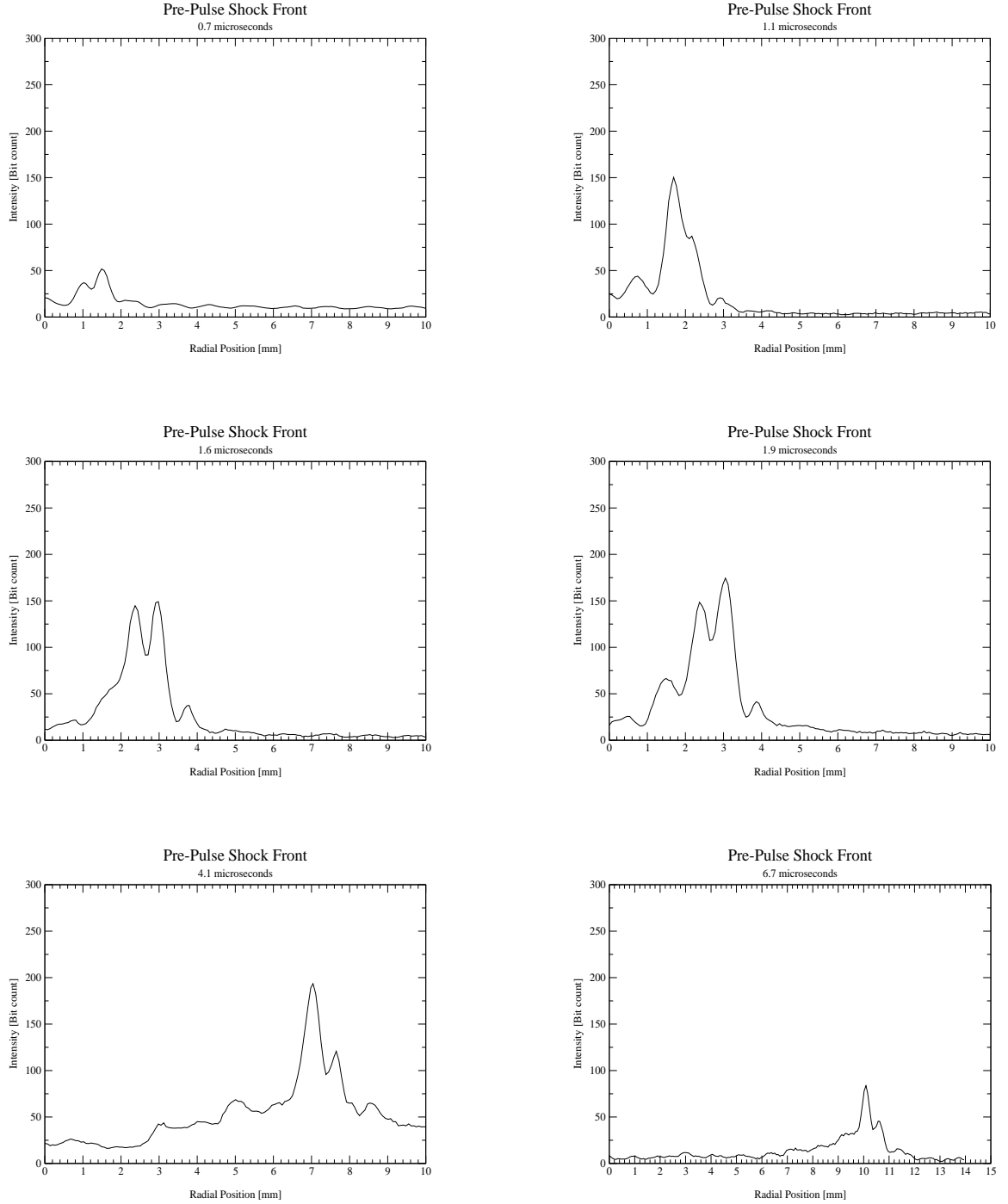
Figure 5.4: Time resolved shock front profiles generated from the schlieren images of a 6.0 kV pre-pulse nitrogen discharge. Discharge parameters $C = 0.5\,\mu\mathrm{F}$, $7\,\mathrm{torr}\ \mathrm{N}_2$. These profiles give a qualitative image of density profile of the propagating shock.

Figure 5.5: Time map of the profiles generated from the schlieren images of a $6.0\,\mathrm{kV}$ prepulse nitrogen discharge. Discharge parameters $C = 0.5\,\mu\mathrm{F}$, $7\,\mathrm{torr}$ N_2. The Z axis corresponds to the bit count of the imaging CCD camera.

0.28 μsec

0.92 μsec

1.75 μsec

2.76 μsec

6.24 μsec

Field of View
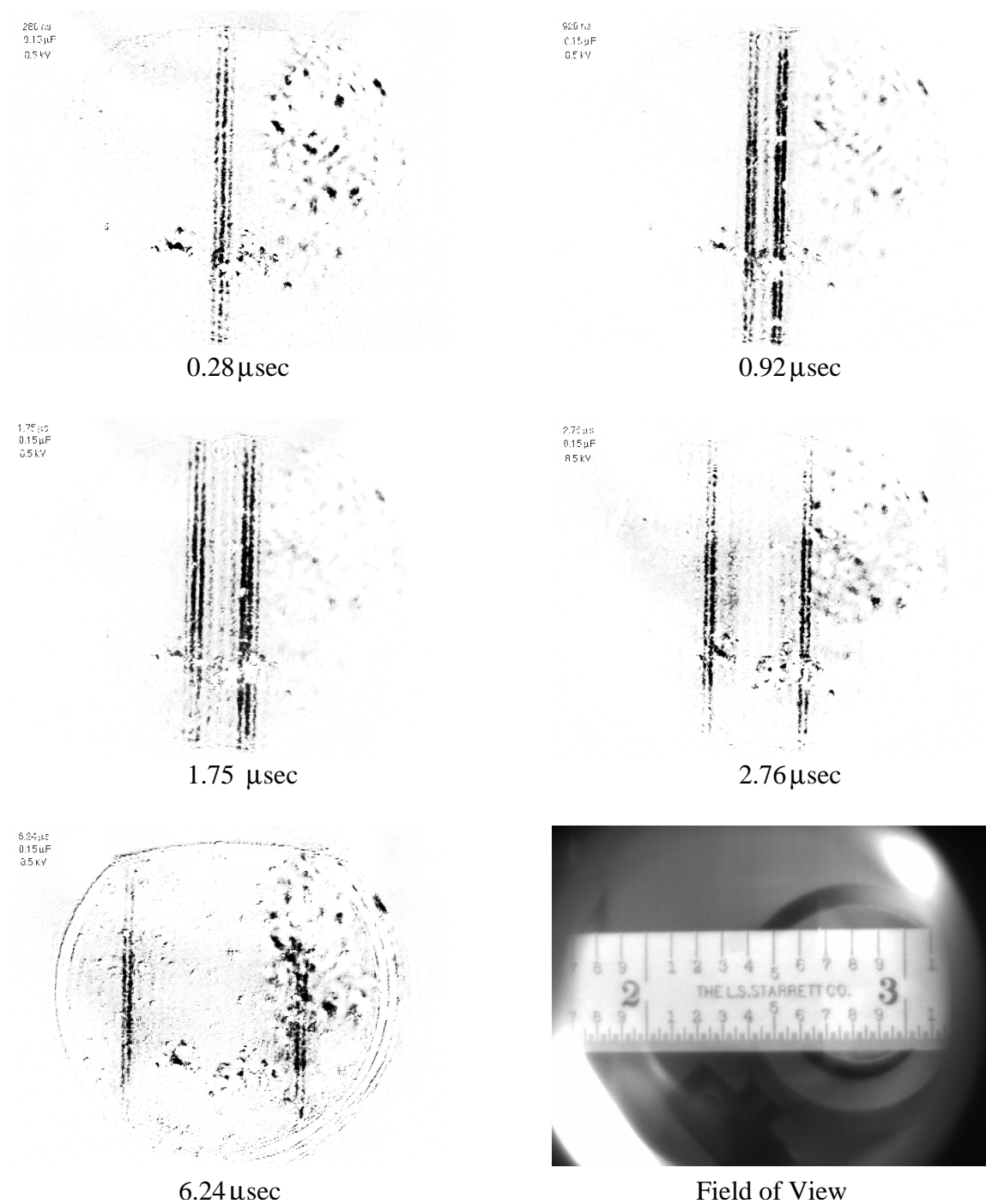
Figure 5.6: Time resolved schlieren images of a 8.5 kV pre-pulse nitrogen discharge. Discharge parameters $C = 0.15\,\mu\text{F}$, 7 torr N_2. The dark blotches on the pictures are carbon residues from benzene breakdown.

Figure 5.7: Time resolved shock front profiles generated from the schlieren images of a 8.5 kV pre-pulse nitrogen discharge. Discharge parameters $C = 0.5\,\mu\text{F}$, 7 torr N_2. These profiles give a qualitative image of the density profile of the propagating shock.

Shock front for 8.5 kV N2 Discharge
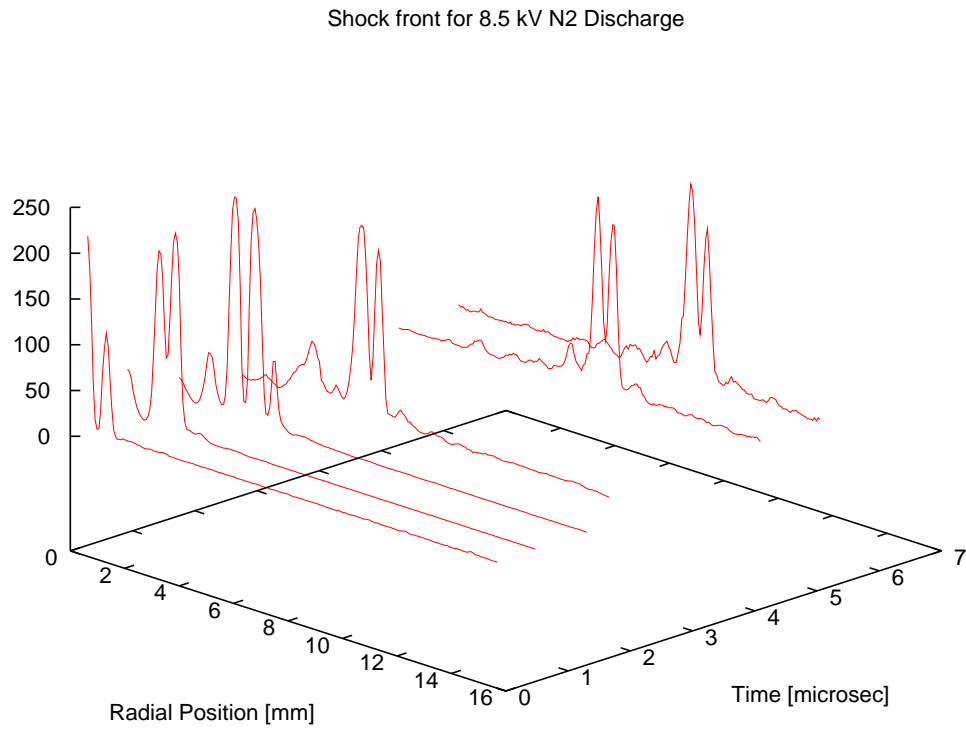
Figure 5.8: Time map of the profiles generated from the schlieren images of a 8.5 kV pre-pulse nitrogen discharge. Discharge parameters $C = 0.5\,\mu\text{F}$, 7 torr N_2. The Z axis corresponds to the bit count of the imaging CCD camera.

density gradients and the profiles generated also incorporate line integrated contributions. One can only infer qualitative information from these figures since there is no direct correlation to the relative density distribution. On the other hand, the image presented by the schlieren instrument is in fact a good representation of the shape and location of the shock front [29].

Figures 5.5 and 5.8 show the time history of the shock front based on the schlieren snapshots. As we will see next, the complete time history is captured with the phase contrast technique.

5.1.3 Phase Contrast

The phase contrast technique made possible the observation of the time evolution of the shock front. This was done by imaging the channel through a $100\,\mu$m slit into a $1\,\mu$s resolution Kentek streak camera. The images produced capture the shock front evolution at a particular representative location approximately in the mid-section along the length of the channel. The pictures in figures 5.9 and 5.10 show the radial shock position (in the ordinate axis) versus the streak camera sweep time (the abscissa axis). One has to note from the pictures that while the sensitivity of the phase contrast instrument is greater than the schlieren, the signal to noise ratio of the images is lower for the phase contrast. Nevertheless, one can obtain the shock front time evolution with good accuracy. A series of experiments were performed to investigate the sensitivity of the shock wave propagation to the variation of the different control parameters. Figures 5.9 and 5.10 show sample images of a voltage scan experiments and gas species scan experiments respectively.

One can infer several things from these images. One can immediately determine
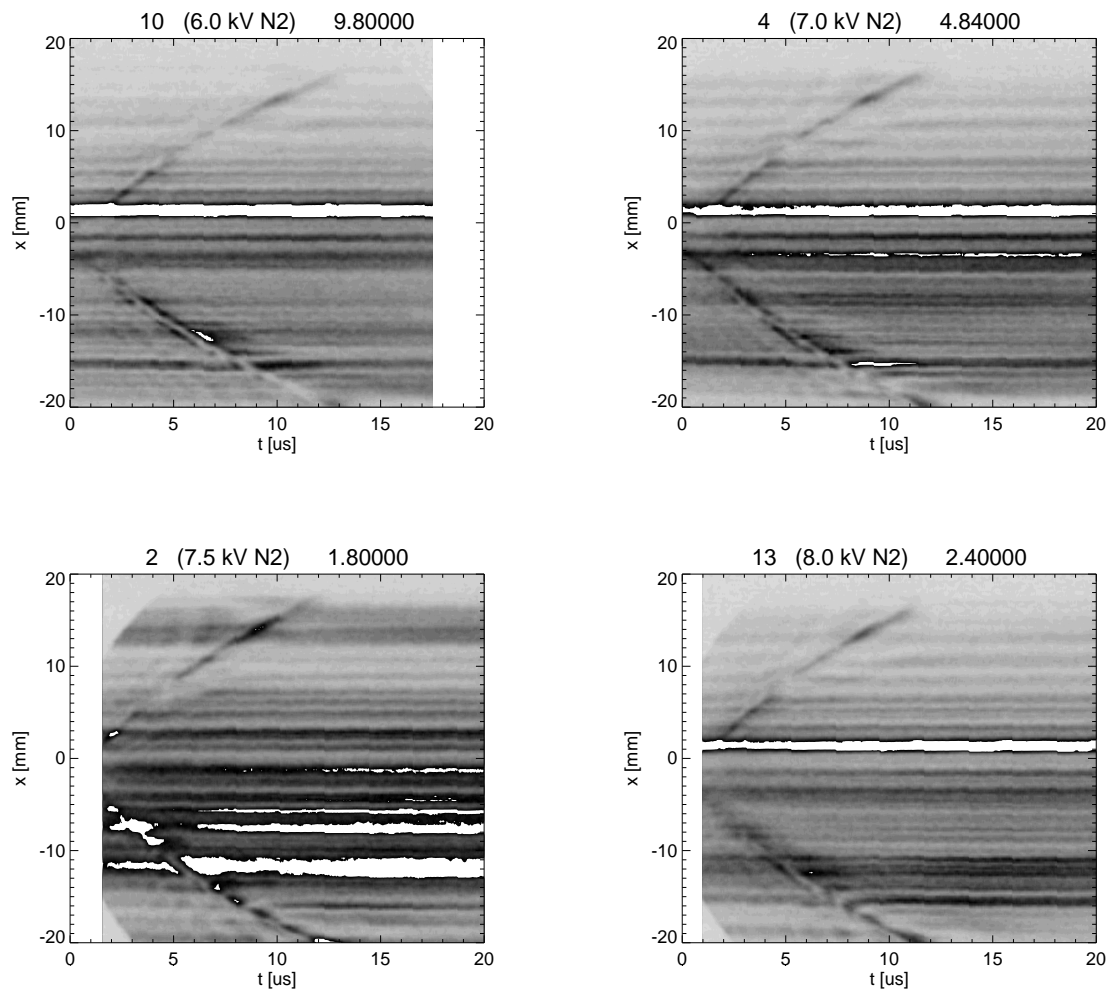
PHASE CONTRAST VOLTAGE SCAN

Figure 5.9: Phase contrast streak images of the pre-pulse expansion shockwave. Discharge voltage scan. The applied voltages are shown in the title to each picture. Fill pressure was 7 torr of nitrogen with 0.5 torr of benzene.
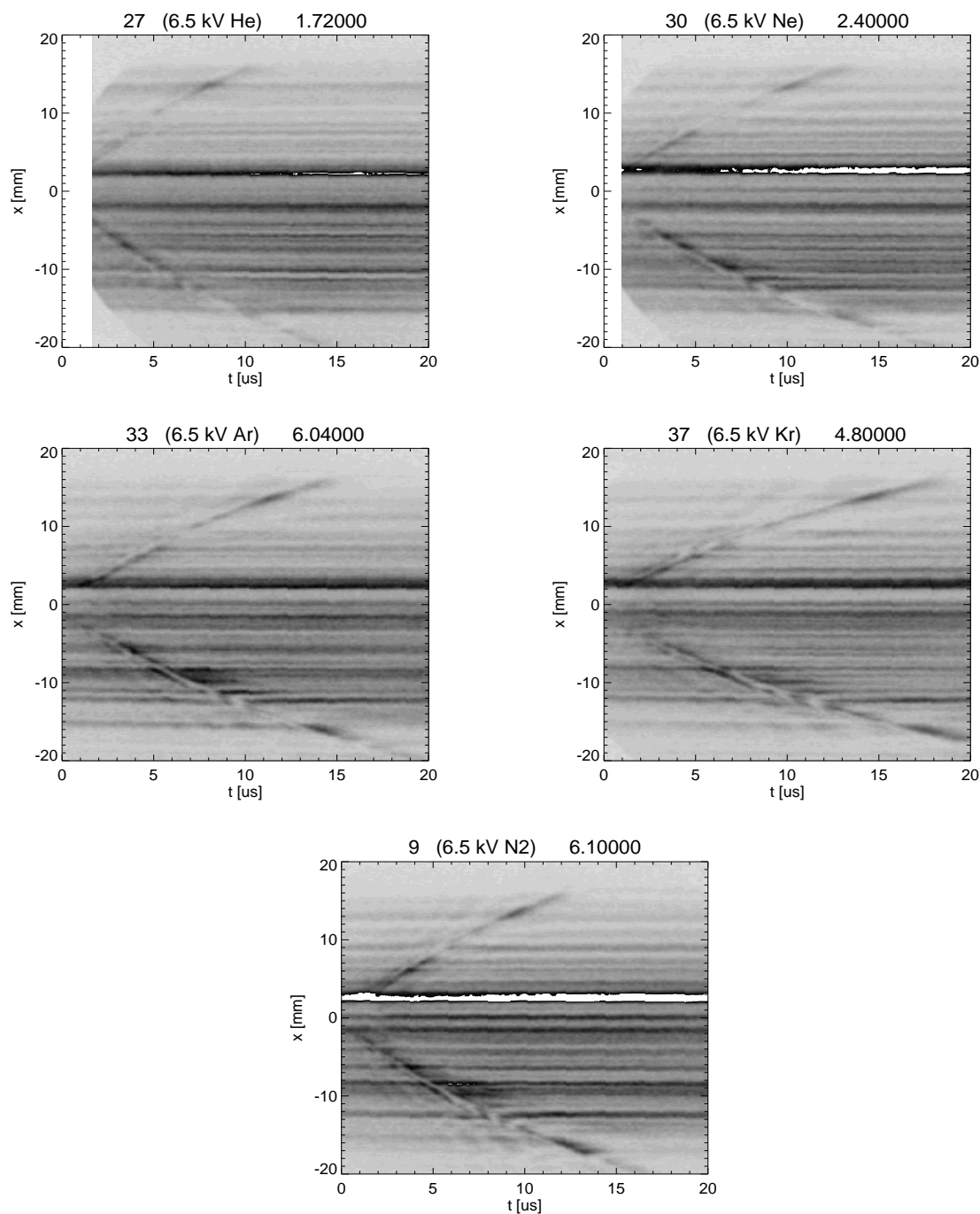
GAS SCAN

Figure 5.10: Phase contrast streak images of the pre-pulse expansion shockwave. Gas fill species scan. Gas species is shown in the title to each picture.Fill pressure was 7 torr with 0.5 torr of benzene.

a speed plot from the shock position versus time plots generated by the phase contrast pictures. From these plots one can determine an upper bound on the gas temperature just behind the shock front. One can apply an empirical model to explain the hydrodynamics based on a strong wave blast model. The strong blast model is similar to the ones studied in supernovae explosions [61]. In this instance we can have as well a second method in which to estimate the gas temperature. This analysis will be presented in section 5.1.4.

The phase contrast pictures reveal some small wave formation just ahead of the main shock, thus suggesting that indeed the initial joule heating takes place over the initial $15\,\mu$s time frame forming this front previous to the avalanche breakdown and the following hydrodynamic expansion. This confirms that the total pre-pulse energy deposition is far from being instantaneous. It is rather unfortunate that the images produced were buried with substantial background noise created by the carbon debris left by the benzene.

5.1.4   Shock Front Data Analysis

The quantitative analysis that can be done with the collected data is mostly for the shock front temporal evolution and its dependence with the several controllable external parameters. These parameters include the applied discharge voltage, gas species, discharge capacitance, and chamber fill pressure. Also shock expansion speed plots can be generated to look at the correlation of the shock front to the variation of the control parameters. I derive gas temperature plots from the shock speed plots. In particular, we can use the relationship

$$v = \sqrt{\frac{k_B T}{m}} \tag{5.1}$$

this equation expressed in terms of the thermal energy U_{therm} is

$$U_{therm} = k_B T = mv^2 \qquad (5.2)$$

From here we can get a first approximation for the gas temperature in the vicinity of the shock.

Capacitor Scan

For this experimental series, the pre-pulse capacitors were changed for each run, maintaining the rest of the parameters constant. This is equivalent to a change in the stored electrical energy used to produce the pre-pulse channel. The installed capacitance was $0.05\,\mu F$, $0.15\,\mu F$, and $0.5\,\mu F$. The applied voltage was $6.5\,kV$ with a N_2 gas fill of $7\,torr$ and $0.5\,torr$ of benzene. This seemed to be the most interesting of all of the runs since, as expected, there is a strong dependence of the shock expansion to the deposited electrical energy. Figure 5.11 shows the data for such runs. The ordinate axis is scaled for FWHM in mm or in plain terms the channel's diameter defined by the shock front.

Figure 5.12 shows the shock front radial position data being fitted to an empirical $r(t) = \kappa\, t^{2/3}$ law, following the reasoning behind the blast wave theory. Here κ is a proportionality constant. The original intent was to apply the blast wave with the $t^{2/5}$ dependence [68] [33], but the predicted radial positions differed significantly, thus prompting me to use a modified version of the blast wave law. Figure 5.13 shows a comparison between the two models. This difference needs to reside in the fact the original blast wave theory is developed around the premise of having a initial point source of energy -the imploding star- and depositing the exploding energy over 4π steradians. In particular our case we have the
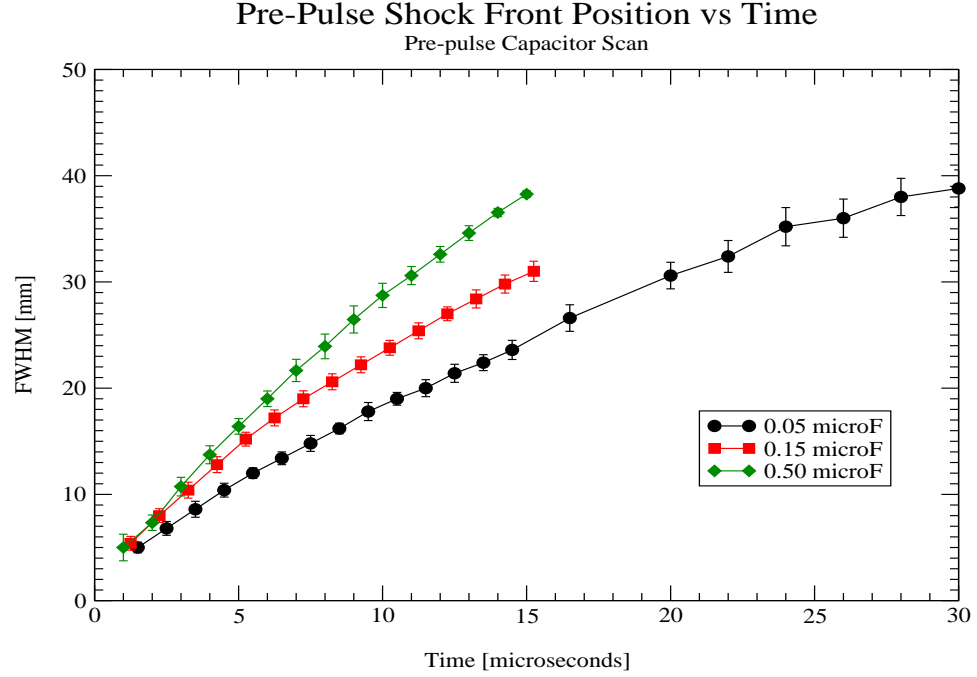
Figure 5.11: Plot generated from the phase contrast streak images of the pre-pulse shock-wave expansion. Capacitor [energy] scan.

energy deposited over a cylindrically symmetric region with the energy deposition being done by a line source. If one were to consider the energy being released by a point source, the problem has to be defined in such a way to restrict it to a plane. Another feature to note from figure 5.13 is that the model that describes the supernova explosion has a steeper initial speed compared to that of the modified model. In the former case the energy deposition is faster and for a short time; in the modified model the energy deposition is slower and occurs over a much longer time as determined by the intrinsic RC circuit decay constant of the channel experiment. Certainly this topic can be the subject of some future theoretical study. For now I will focus on discussing the phenomenological aspects of the data.

Figures 5.14 and 5.15 show the local speed and local temperature of the shock
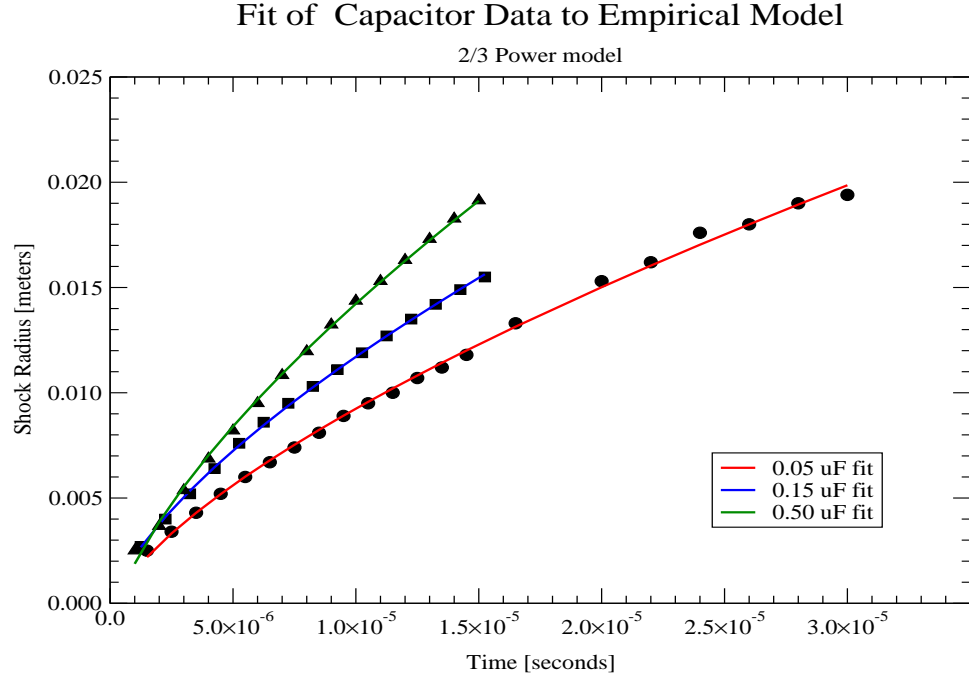
Figure 5.12: Plot of the phase contrast pre-pulse shockwave expansion data fitted to the $t^{2/3}$ law. Capacitor [energy] scan.

front as a function of time as it moves radially outward from the channel's axis. These plots are generated from the fitted position law, namely from

$$r(t) = \kappa\, t^{2/3} \tag{5.3}$$

$$v(t) = \frac{2}{3}\frac{\kappa}{t^{1/3}} \tag{5.4}$$

$$k_B T(t) = \frac{4}{9}\, M\, \frac{\kappa^2}{t^{2/3}} \tag{5.5}$$

where M is the mass of the molecule species and k_B the Boltzmann constant. Table 5.1 shows the value of κ for the different shock fronts.

If we take equation (5.5) solve for κ and substitute back in equation (5.3) we obtain

$$r(t) = \frac{3}{2}\sqrt{\frac{k_B T(t)}{M}}\, t \tag{5.6}$$

where we can identify the square root term as the sound speed.

Comparison Between the Functions
x^(2/5) and x^(2/3)
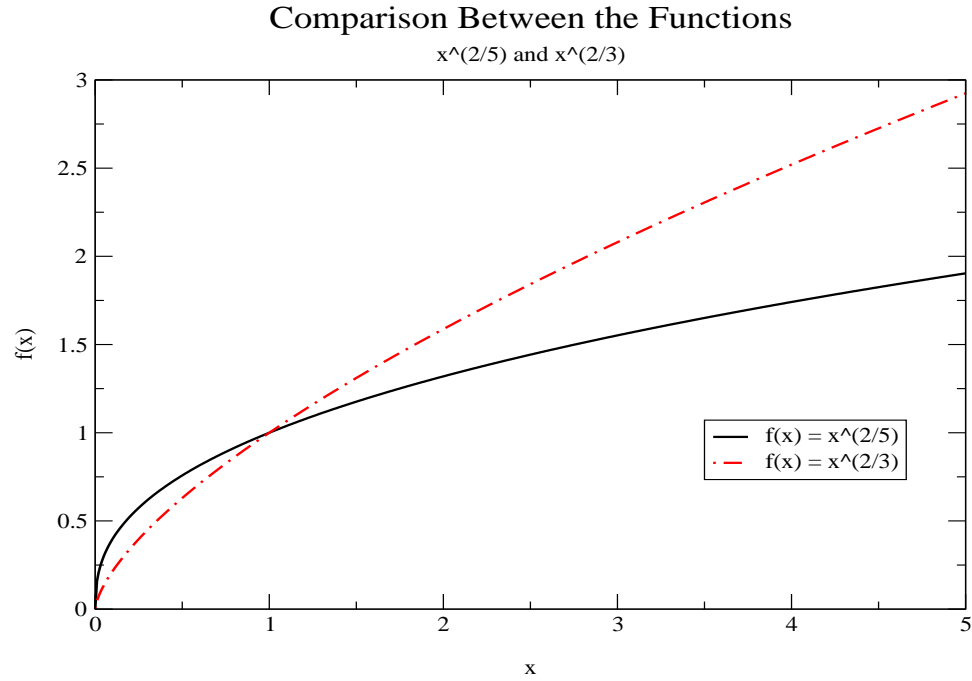
Figure 5.13: Comparison between the functions $f(x) = x^{2/5}$ and $f(x) = x^{2/3}$. Supernova explosions are better described by the $f(x) = x^{2/5}$ power law, while the pre-pulse channel is by the $f(x) = x^{2/3}$ function.

Capacitor installed $[\,\mu F]$	$\kappa \; \left[\frac{m}{s^{2/3}}\right]$
0.05	21.1711
0.15	25.9977
0.50	33.9287

Table 5.1: Values of κ for equation 5.3 generated from the pre-pulse capacitor data.
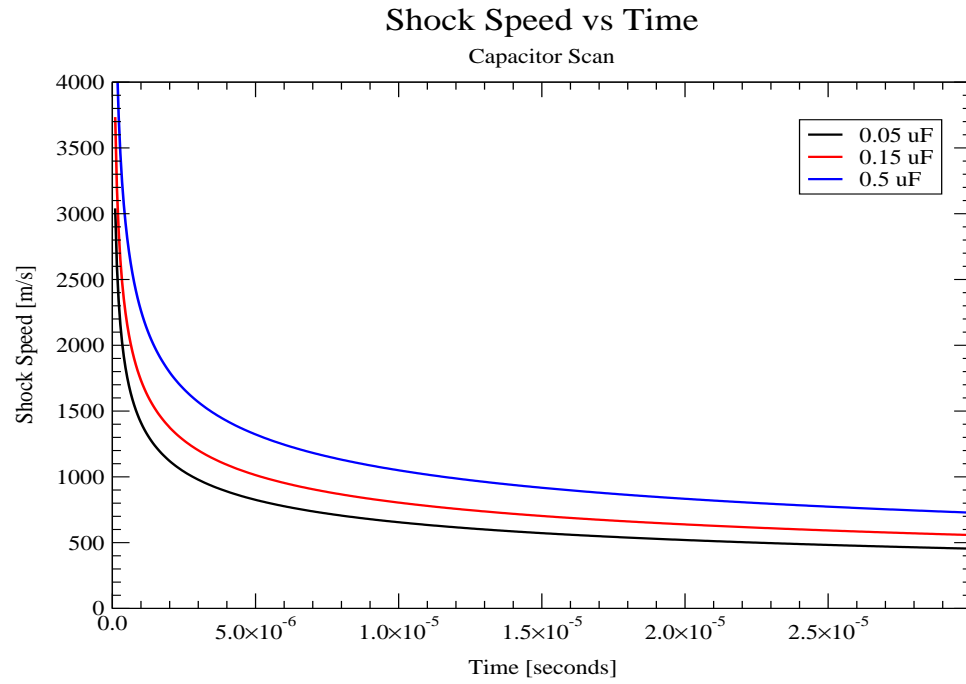
Figure 5.14: Shockwave speed as a function of time derived from equation 5.4. Capacitor [energy] scan.
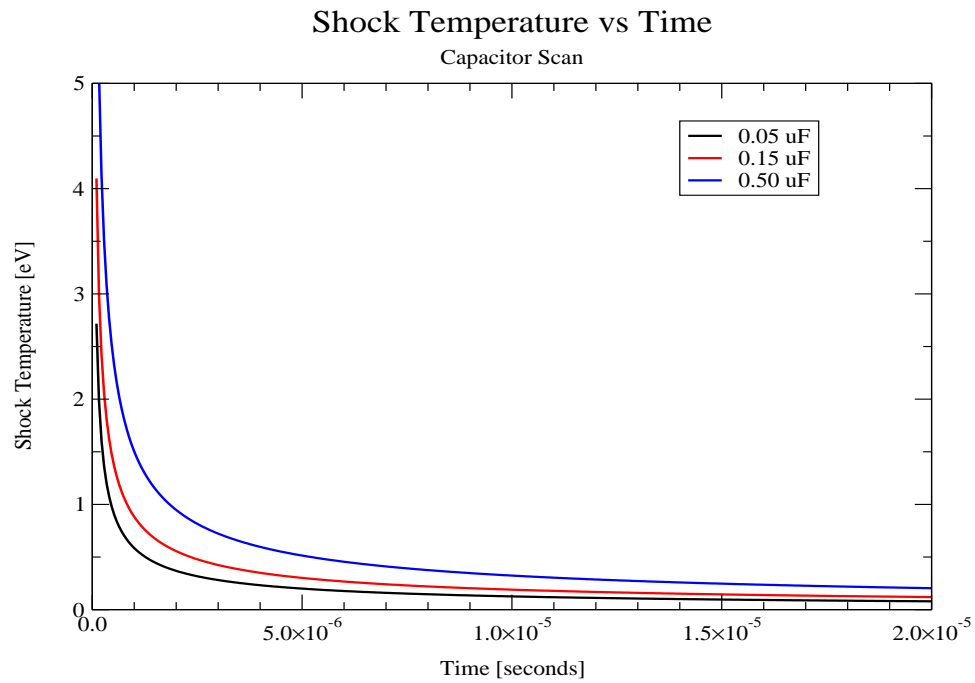
Figure 5.15: Shockwave temperature as a function of time derived from equation 5.5. Capacitor [energy] scan.

Gas Species Scan

From the species scan data we can extend our phenomenological arguments. Here it is of interest how the molecular mass affects ultimately the size of the gas depression left by the pre-pulse discharge. A priori we can anticipate that the heavier the gas, the slower the shock expansion and smaller the pre-pulse channel left for the main bank.

Keeping the pre-pulse energy constant, e.i., constant pre-pulse voltage with constant pre-pulse capacitance, one would expect a simple relationship where the shock speed was only dependent on the mass of the species. This is not the case. Certainly other energy related processes are in play such as the ionization potentials for each species when it comes down to making an energy balance assessment. In our case we can just take the ratios of the respective thermal energies

$$\frac{U_{\mathrm{I}}}{U_{\mathrm{II}}} = \frac{k_B T_{\mathrm{I}}}{k_B T_{\mathrm{II}}} = \frac{M_{\mathrm{I}} \kappa_{\mathrm{I}}^2}{M_{\mathrm{II}} \kappa_{\mathrm{II}}^2} \tag{5.7}$$

Here the subindices I and II denote the different gas species to be compared.

Figure 5.16 shows the gas species data. By fitting our data to equation (5.3) we can determine κ for each plot, then we can tabulate the ratios of the calculated $U_{thermal}$ of the different gas species to that of helium. This comparison is presented in table 5.2 The interesting fact is that molecular nitrogen behaves like argon. This might imply that a considerable amount of the energy expended goes into dissociating the molecules. This is an interesting effect that would have to be studied further in case of an engineering analysis for target chamber gas fill. This might imply that a vapor-gas mixture of FLiBe-Xenon will behave quite differently than that of pure xenon or other monoatomic gas in the presence of FLiBe. For all practical purposes in the use of the pre-pulse to control the main bank

Species	M_{species} [amu]	$\kappa \left[\frac{\text{m}}{\text{s}^{2/3}}\right]$	$U_{\text{species}}/U_{\text{Helium}}$
Helium	4	36.8162	1.000
Neon	20	30.0966	3.341
Argon	40	29.9053	6.598
Krypton	84	23.4567	8.525
Nitrogen Molecule	28	33.9287	5.945

Table 5.2: Values for κ determined by equation 5.3 and the respective computed thermal energy relative to helium for the tested gas species. Reference is that of the He$_4$ isotope.
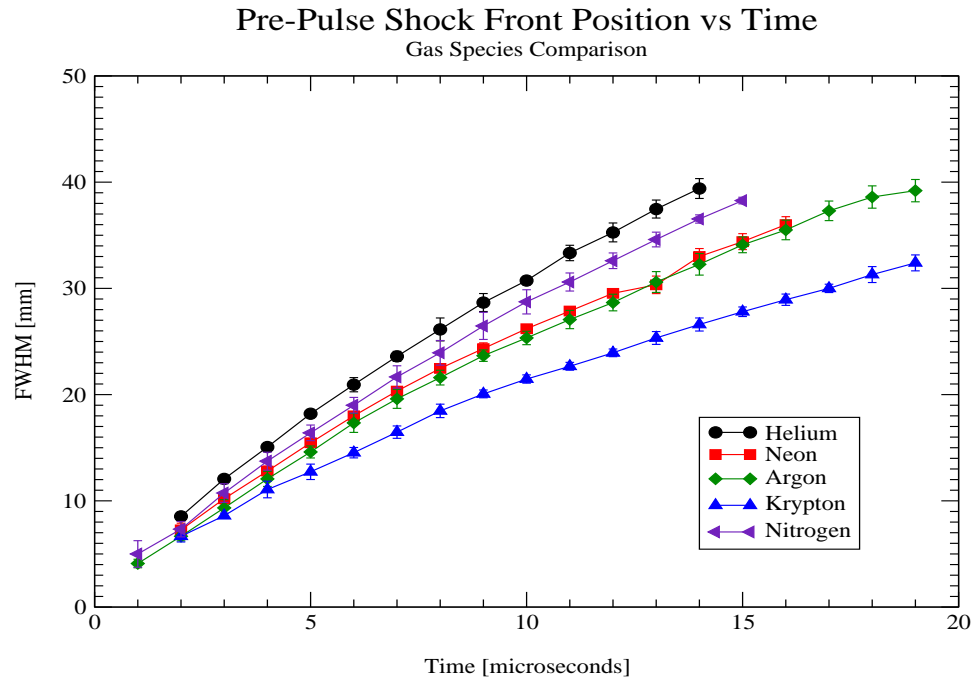
Figure 5.16: Phase contrast streak images of the pre-pulse expansion shockwave. Gas fill species scan.

Fit of Gas Species Data to Emperical Model

2/3 Power Model
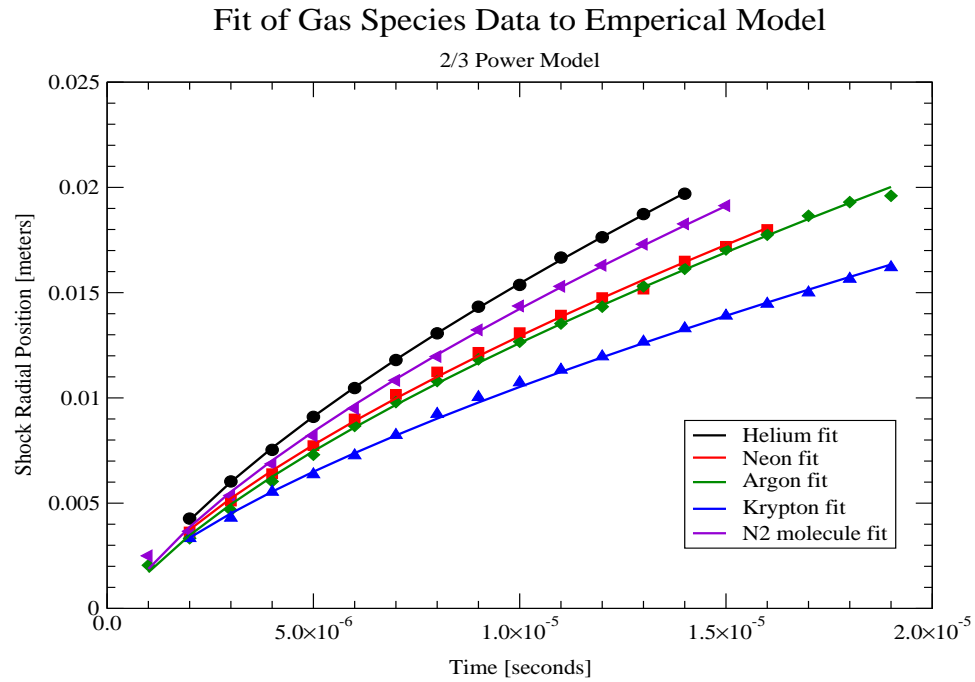
Figure 5.17: Plot of the phase contrast pre-pulse shockwave expansion data fitted to the $t^{2/3}$ law. Gas fill species scan.

Shock Temperature vs Time
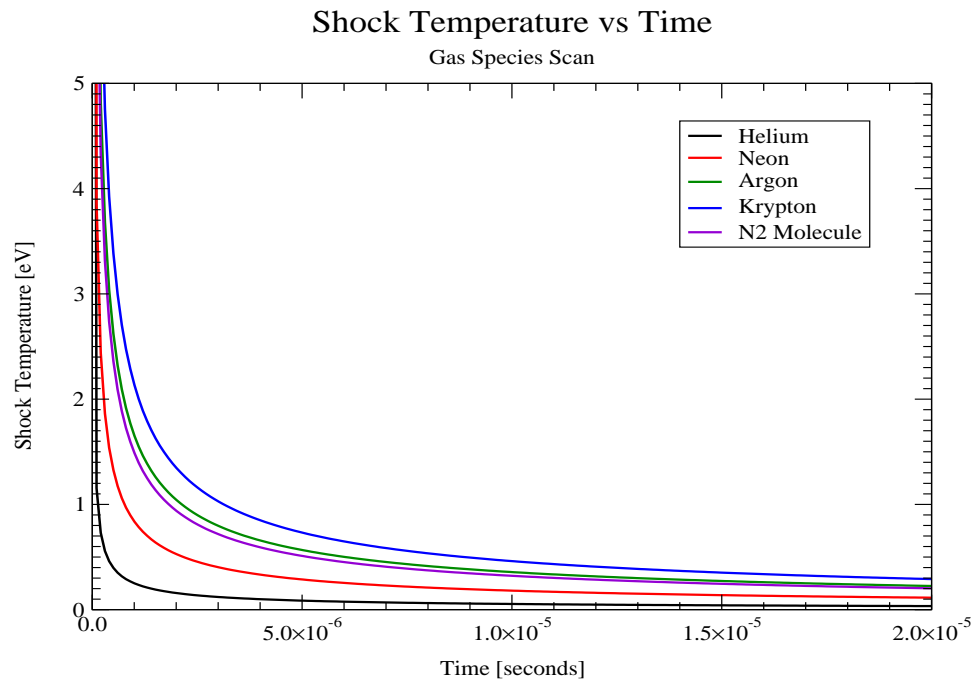
Gas Species Scan

Figure 5.18: Shockwave temperature as a function of time derived from equation 5.5. Gas fill species scan.

pinch size and pinch timing one would want to put the heaviest gas in the target chamber of a HIF fusion device due to its slower rate of expansion. The data suggest the use of a gas such as krypton or xenon.

Voltage and Pressure Scan

The pre-pulse shock front showed to be much less sensitive to the pre-pulse applied voltage as well as to the gas filled pressure. While it is not surprising that the pressure fill does not affect the characteristics of the shock front, it is surprising how the discharge is insensitive to the applied pre-pulse voltage. The insensitivity to the applied voltage does have an explanation. In the case of this series, we are indeed varying the pre-pulse energy, but the variation is much smaller than the variation in the capacitor scan series. The significant aspect to note here is that or voltage variation really reflects the sensitivity to the ratio of $\vec{E}/P$. Figure 5.19 shows the collected data for the voltage scan and the pressure scan is shown in figure 5.20. Although from the physics point of view these insensitivities are not very exciting, they do provide a positive note for pre-pulse control. The variation on the applied voltage is seen on the joule heating phase just before breakdown as shown in figure 3.5. One can adjust both the pressure and voltage in conjunction to optimize the avalanche process that appropriately depends in the ratio of $\vec{E}/P$. Also we must remember that benzene plays an important role. This can be seen from the data and discussion presented in section 3.2.
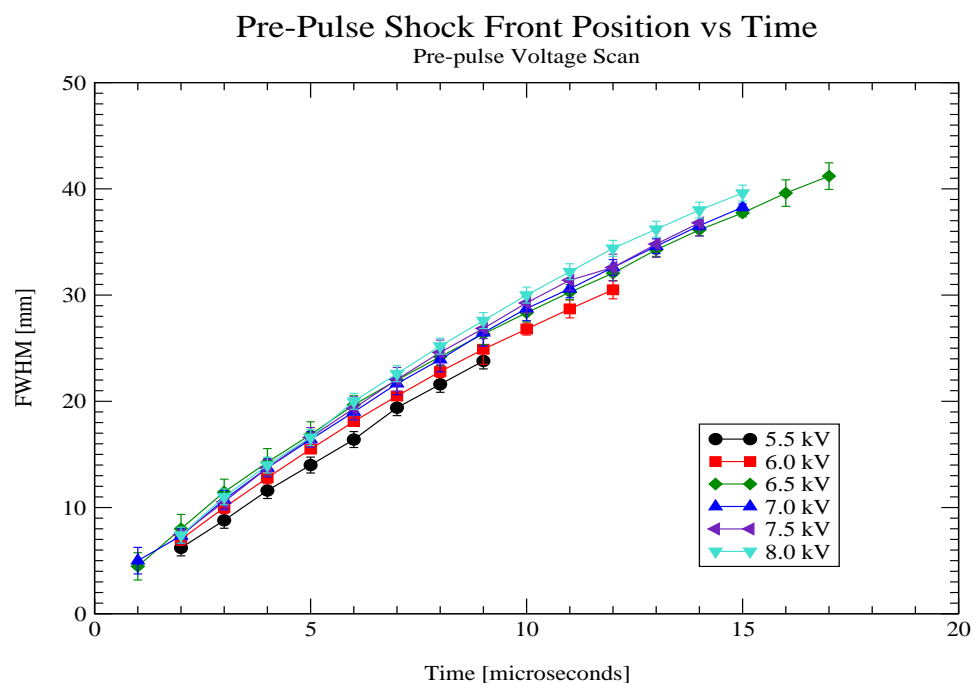
Figure 5.19: Phase contrast streak images of the pre-pulse expansion shockwave. Voltage scan.
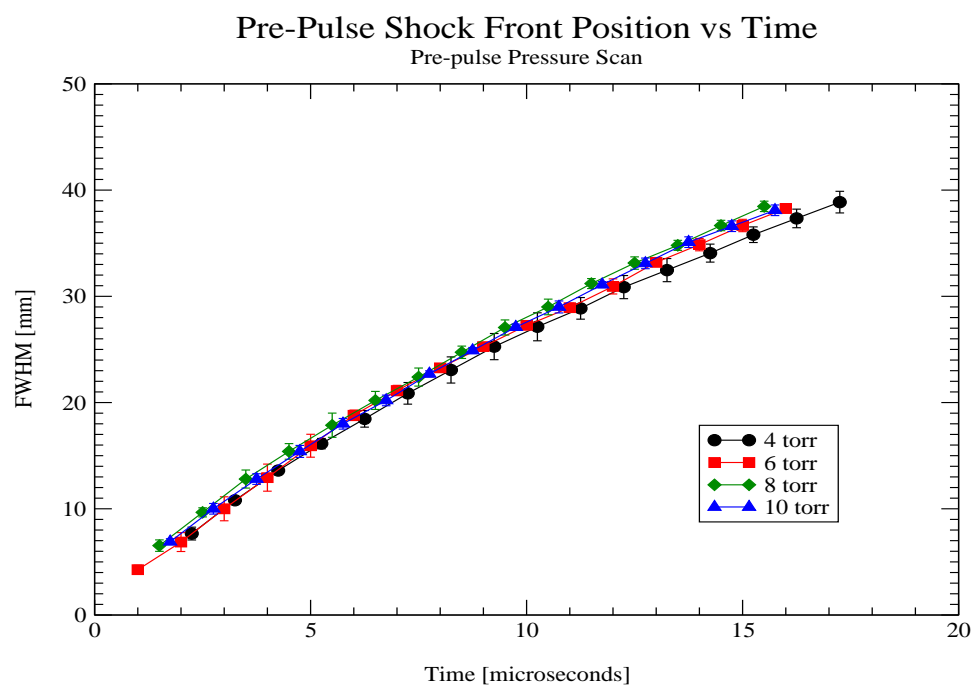
Figure 5.20: Phase contrast streak images of the pre-pulse expansion shockwave. Pressure scan.

5.2   Main Bank

The main bank discharge depends greatly on the conditions left by the pre-pulse discharge. The repeatability, MHD stability and uniformity of the z-pinch seemed to be very well correlated to the pre-existence of the pre-pulse firing properly. In the following sections I'll present the data collected in the investigation of the main bank discharge characteristics preceded by the pre-pulse through the study of the channel's plasma electron temporal evolution and an attempt to determine the main channel's magnetic field distribution.

5.2.1   Voltage and Current Waveforms

The initial assessment of the main bank discharge can be made from the voltage and current waveforms. Figures 5.21 and 5.22 show a $15\,\mathrm{kV}$ and a $22\,\mathrm{kV}$ discharge respectively. The region of interest is the quarter period that includes the first $4\,\mu\mathrm{s}$ after the initial application of the main bank voltage. The energy deposited into the channel in the first $4\,\mu\mathrm{s}$ is approximately $400\,\mathrm{J}$ for a $15\,\mathrm{kV}$ discharge.

During the following quarter cycle most of the energy stored in the magnetic field is returned to the pulser. From the energetics point of view, only one-fourth of the electromagnetic energy ($\sim 100\,\mathrm{J}$) get dissipated through non-conservative processes. This implies that about $300\,\mathrm{J}$ get stored in the magnetic field produced by the channel's current. We can estimate an average to the $\vec{B}$ field through a back-of-the-envelope calculation. Knowing that

$$\langle B \rangle = \sqrt{\frac{8\pi U}{V}} \tag{5.8}$$

where U is the energy in the magnetic field and V is the volume that encloses the magnetic

Voltage and Current Waveforms for 15 kV Main Bank Discharge

7 torr nitrogen, 0.5 torr benzene
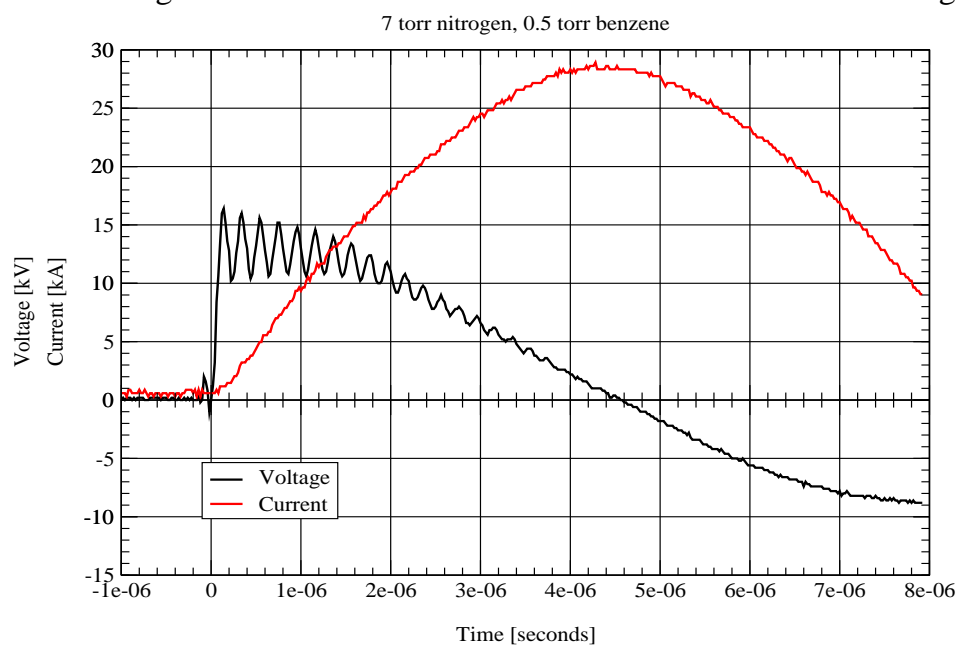
Figure 5.21: Main bank voltage and current waveforms. 15 kV discharge

Voltage and Current Waveforms for 22 kV Main Bank Discharge

7 torr nitrogen, 0.5 torr benzene
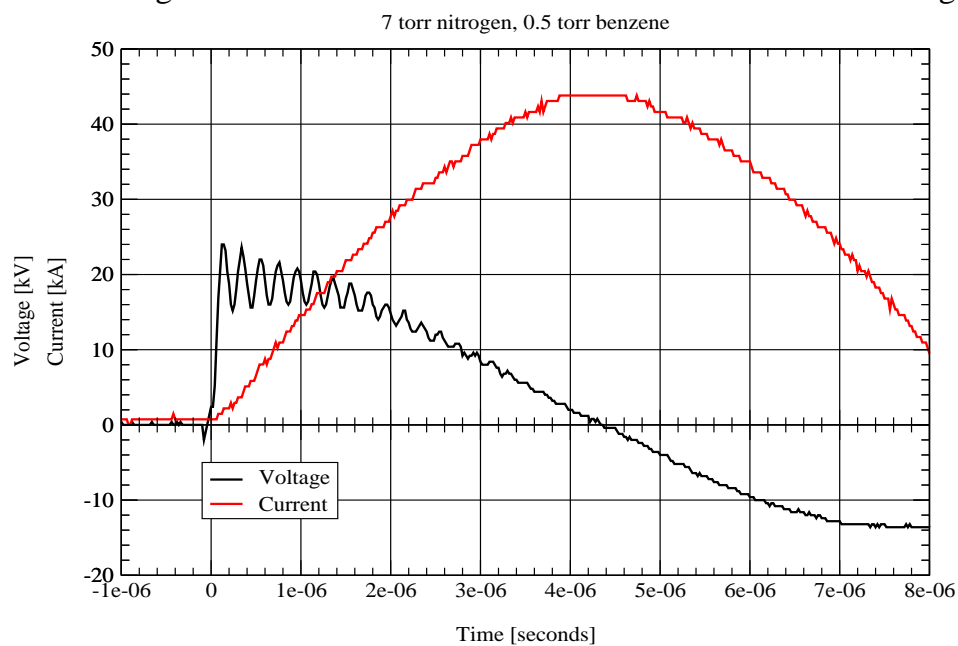
Figure 5.22: Main bank voltage and current waveforms. 22 kV discharge

field. The rough dimensions of the chamber are $30\,\text{cm} \times 30\,\text{cm} \times 40\,\text{cm}$. Crunching the numbers give a value for $\langle B \rangle \sim 0.2\,\text{T}$.

5.2.2 Interferometry

The data collected with the Michelson interferometer apparatus consisted of fringe images that could be directly related to the electron density produced by the main bank discharge. Typical discharge parameters were $7\,\text{torr}$ of N_2, $15\,\text{kV}$ to $30\,\text{kV}$ of applied voltage. Figure 5.23 shows the interferometer output both in the absence and presence of the electron density produced by the main bank channel. Figures 5.25 and 5.26 show examples of interferometer images for main bank discharges at $15\,\text{kV}$ and $22\,\text{kV}$ respectively. The images correspond to the mid section of the plasma channel.

From the interferograms there is no evidence of MHD instability. The pictures in figures 5.25 and 5.26 can be contrasted with figure 5.24 where there is evidence of MHD instability due to the firing of the main bank with no pre-pulse discharge.

5.2.3 Electron Density Data Analysis

Directly from the interferograms one can obtain the line integrated electron density for the plasma channel. From the discussion in section 4.2 we can see that the corresponding line integrated density for each fringe deflected by a one fringe unit corresponds to $10^{17}\,\text{cm}^{-2}$. Figures 5.27 and 5.28 show the line integrated electron density for a $15\,\text{kV}$ and $22\,\text{kV}$ main bank discharge respectively with corresponding peak integrated electron densities of $4 \times 10^{17}\,\text{cm}^{-2}$ and $6 \times 10^{17}\,\text{cm}^{-2}$. Both discharges were done on a $7\,\text{torr}$ nitrogen gas fill. Figures 5.29 and 5.30 show the same data as figures 5.27 and 5.28, but they are plotted as
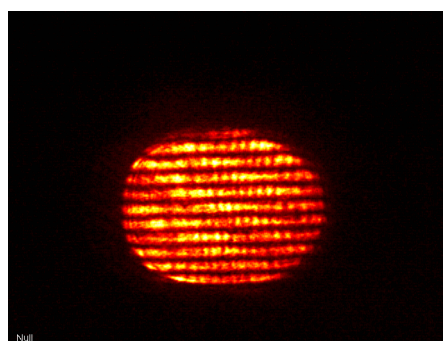
Null (no channel)
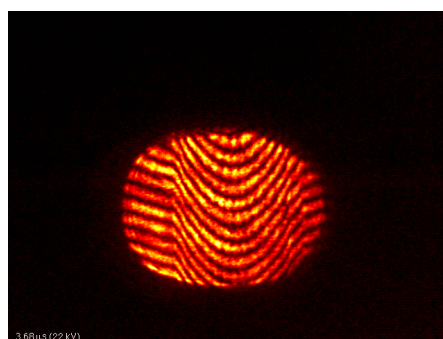
Plasma Channel
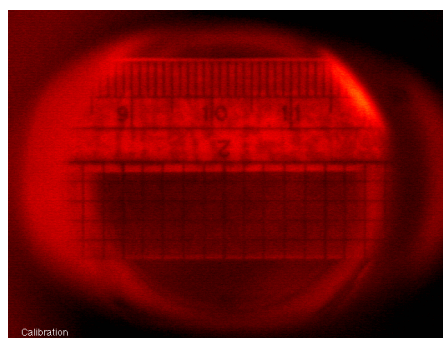
Reference Scale

Figure 5.23: Interference fringes: no channel (null), channel, and scale.
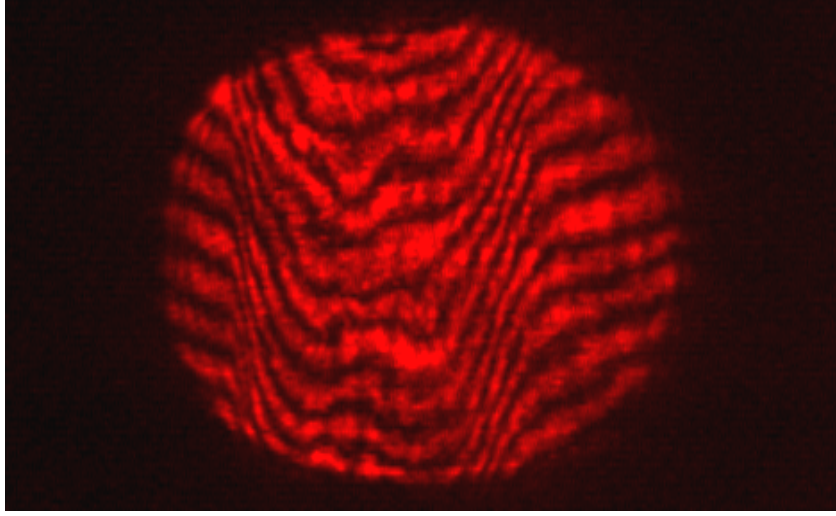
Main Bank Discharge in the absence of Pre–pulse

Figure 5.24: Interference fringes in the absence of the pre-pulse showing instabilities. $I_{MB} = 27\,kA$

a surface to emphasize the electron density time evolution.

The electron density can be determined by deconvolving the line integrated data utilizing abel's inversion. A brief review of the technique for doing so is presented in appendix C. I fit the line integrate density to an 8th degree polynomial and just keep the even power terms. The need to drop these terms is necessary due to the symmetry requirements imposed by the Abel deconvolution. The error incurred by dropping the odd terms of the polynomial is negligible since the odd terms are smaller by at least 9 orders of magnitude. The coefficients to the polynomial fits are shown in table 5.3 for the $15\,kV$ discharge and table 5.4 for the $22\,kV$ discharge.

Once the polynomial fit is determined, the Abel inversion process can be done. The term by term coefficients for the Abel inverted line density are presented in table 5.5 for the $15\,kV$ discharge and in table 5.6 for the $22\,kV$ discharge. The electron density

1.0 μsec

2.12 μsec

3.02 μsec

5.12 μsec
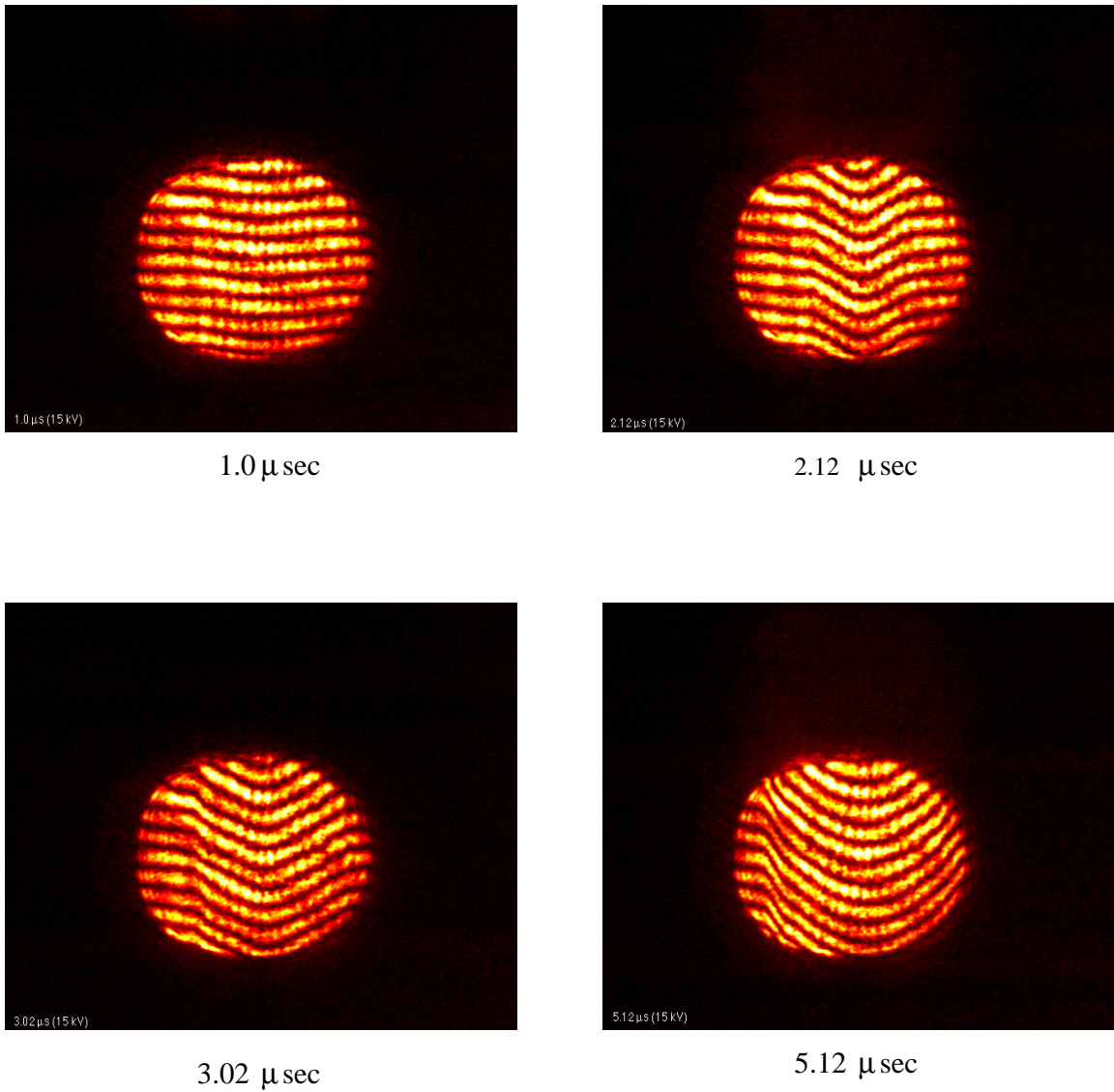
Evolution of electron plasma density 15 kV discharge

Figure 5.25: Interferometric fringes showing the time evolution of a main bank channel for a 15 kV discharge.

0.98 μsec

2.12 μsec

2.96 μsec

3.68 μsec
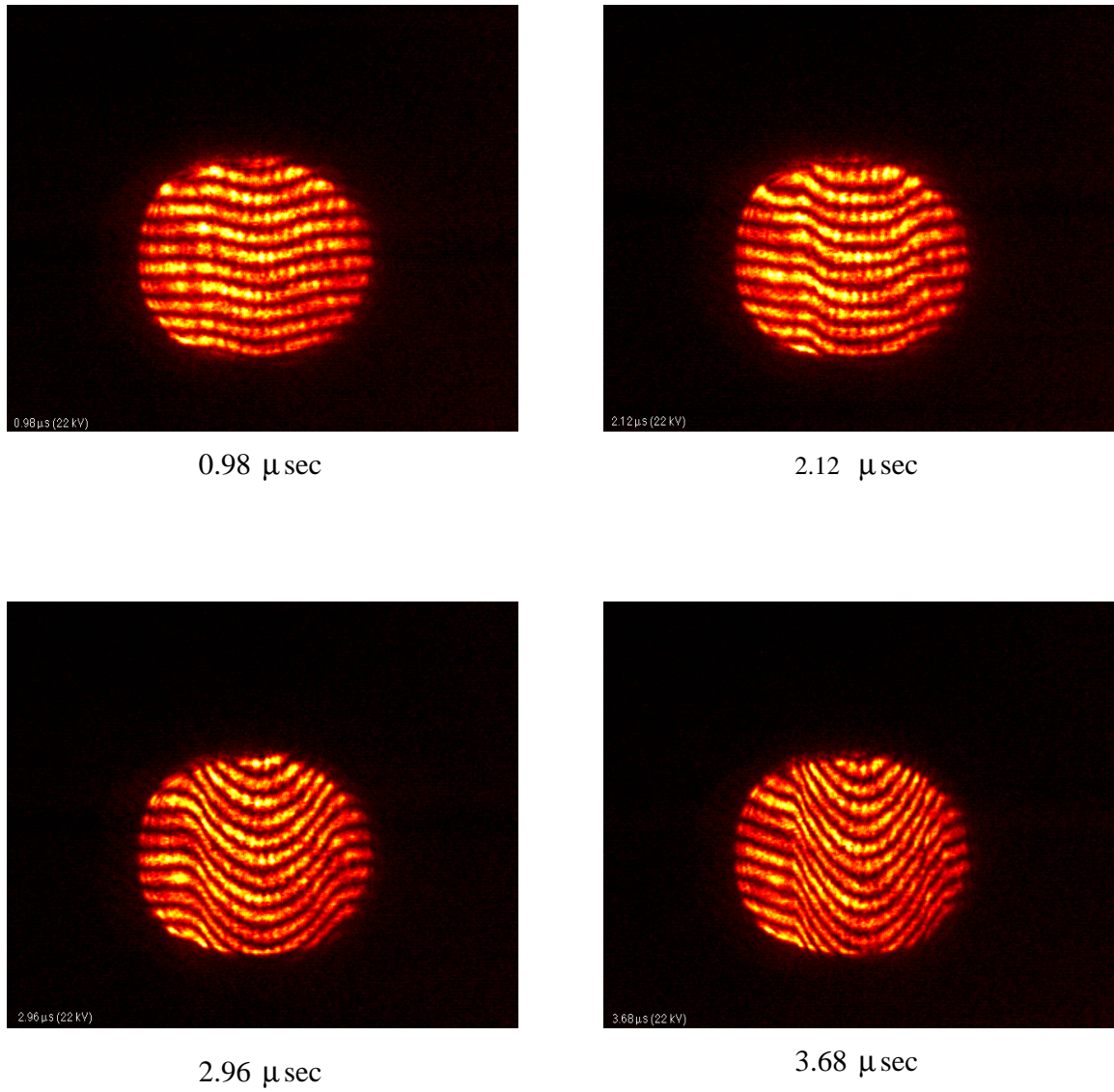
Evolution of electron plasma density 22 kV discharge

Figure 5.26: Interferometric fringes showing the time evolution of a main bank channel for a 22 kV discharge.

Figure 5.27: Line integrated electron density of a 15 kV discharge.
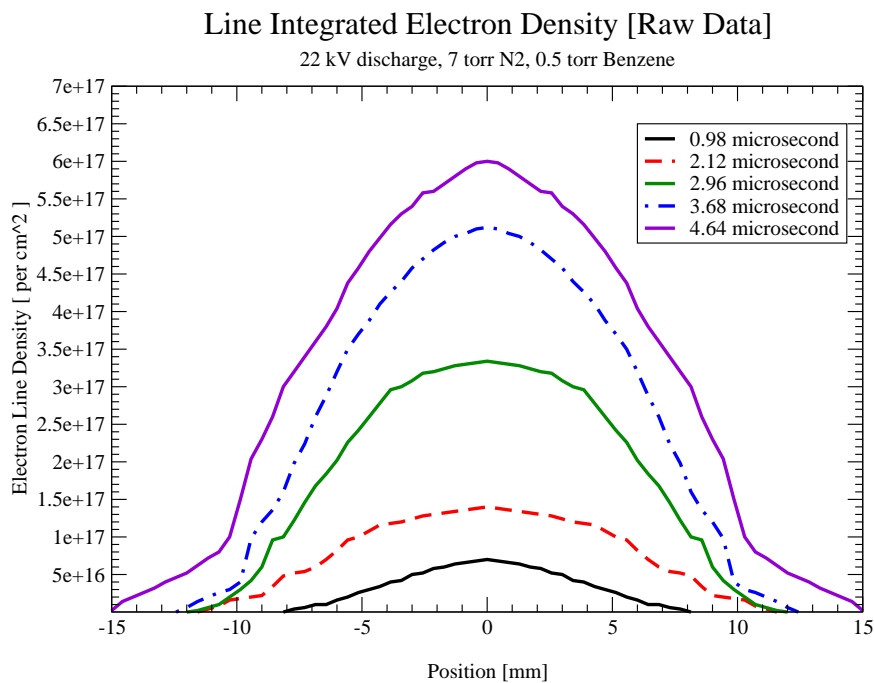
Figure 5.28: Line integrated electron density of a 22 kV discharge.

15 kV Line Integrated Electron density [per cm^2]
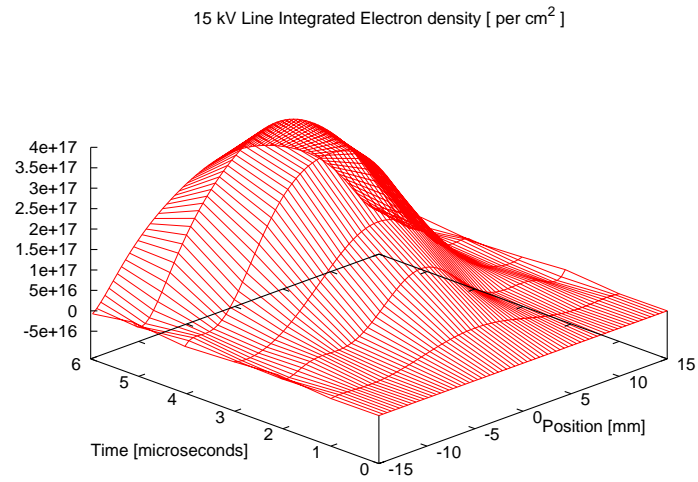
Figure 5.29: Time evolution of the line integrated electron density for a 15 kV discharge.

22 kV Line Integrated Electron density [per cm^2]
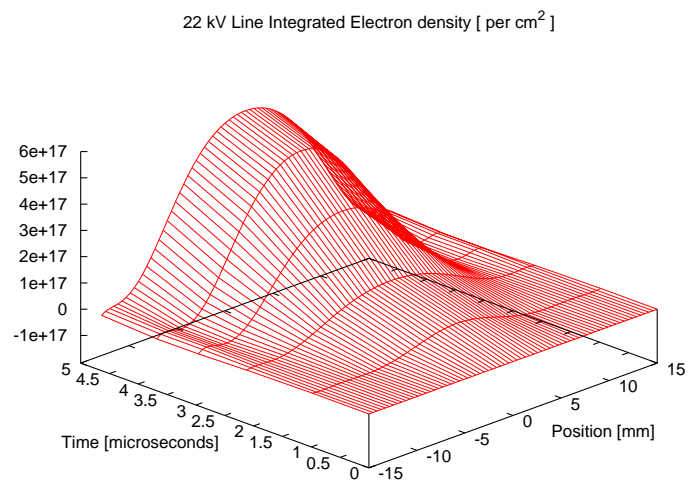
Figure 5.30: Time evolution of the line integrated electron density for a 22 kV discharge.

15 kV Main Bank Discharge

Time	Coefficients ($\times 10^{17}$)				
	x^0	x^2	x^4	x^6	x^8
$1.00\,\mu s$	0.4338	-0.9161	0.5895	-0.1083	-0.0053
$2.06\,\mu s$	1.3290	-3.3539	3.2584	-1.4246	-0.2329
$3.02\,\mu s$	2.1679	-3.2843	1.9010	-0.5529	0.0750
$4.04\,\mu s$	3.3960	-2.4052	-2.2513	2.4469	-0.5654
$5.12\,\mu s$	3.7119	-2.5585	1.0384	-1.0072	0.3262
$5.96\,\mu s$	2.6634	-1.4961	0.6772	-0.6241	0.1695

Table 5.3: Values of the coefficients for even power terms of the polynomial fit of the integrated line density for the 15 kV channel discharge. Radial coordinate x from 0 cm to 1.5 cm.

22 kV Main Bank Discharge

Time	Coefficients ($\times 10^{17}$)				
	x^0	x^2	x^4	x^6	x^8
$0.98\,\mu s$	0.6713	-2.1771	2.4924	-1.1997	0.2063
$2.12\,\mu s$	1.3894	-1.6074	-0.0696	0.5908	-0.1628
$2.96\,\mu s$	3.3740	-3.4138	-1.3891	2.3044	-0.5846
$3.68\,\mu s$	5.0844	-5.2564	-1.3047	2.7388	-0.6994
$4.64\,\mu s$	5.8533	-4.1178	-2.3949	2.7297	-0.6049

Table 5.4: Values of the coefficients for even power terms of the polynomial fit of the integrated line density for the 22 kV channel discharge. Radial coordinate x from 0 cm to 1.5 cm.

profiles generated are shown in figures 5.31 and 5.32 for the 15 kV and the 22 kV discharge respectively. The deconvolution analysis gives an upper bound on the shape and value of the electron density function. In practice, it is much more useful and accurate to obtain theoretically an electron density distribution and try to replicate the line integrated electron density results. One can take the results of figures 5.31 and 5.32 as first guess values for simulation purposes. Peak electron density values are $1.55 \times 10^{17} \, \text{cm}^{-3}$ for the 15 kV discharge and $3.3 \times 10^{17} \, \text{cm}^{-3}$ for the 22 kV discharge.

If one is to proceed with the notion that the Abel analysis is just a first approximation, one can determine other parameters of the channel's evolution. From the deconvolved electron density I have made several plots. One of these plots is the electron density evolution for 15 kV and 22 kV discharges shown in figures 5.33 and 5.34 respectively. Also of interest is the on-axis electron density evolution as well as the width of the electron density distribution which is an indirect and qualitative way to characterize the effect of the pinching magnetic field. If one could determine the plasma temperature evolution as well, perhaps through some spectroscopic measurement [1] [31] [69], then one can estimate the magnetic pressure that equilibrates the mechanical pressure. Figures 5.35 through 5.37 show the plasma width and the on-axis electron density evolution.

A question of interest is the degree of ionization during the main bank discharge. One can roughly estimate this by comparing the electron density to the number of molecules in the chamber gas fill. The number of molecules in the chamber can be determined by using the ideal gas equation of state and Loschmidt's number, which is the number density of gas molecules at STP conditions. What is somewhat unknown is the base density when

15 kV Main Bank Discharge Inverted

Time	α	Coefficients ($\times 10^{17}$)			
		a_0	a_2	a_4	a_6
$1.00\,\mu s$	1.00	1.1821	-1.3916	0.3561	0.0193
$2.06\,\mu s$	1.00	4.3389	-6.0905	4.9847	0.8519
$3.02\,\mu s$	1.44	4.0385	-4.0087	1.5718	-0.2743
$4.04\,\mu s$	1.96	4.2792	1.3088	-5.8037	2.0677
$5.12\,\mu s$	1.69	4.4296	-1.3234	2.2149	-1.1930
$5.96\,\mu s$	1.69	3.5117	-1.8469	1.9447	-0.0062

Table 5.5: Values of the coefficients for even power terms of the Abel inverted polynomial fit of the electron density for the 15 kV channel discharge. Radial coordinate r from 0 cm to 1.0 cm for the equation $N_e(r) = \frac{1}{\pi}\left[\sqrt{\alpha - r^2}\left(a_0 r^0 + a_2 r^2 + a_4 r^4 + a_6 r^6\right)\right]$.

22 kV Main Bank Discharge Inverted

Time	α	Coefficients ($\times 10^{17}$)			
		a_0	a_2	a_4	a_6
$0.98\,\mu s$	0.64	2.7552	-5.5338	3.5976	-0.7545
$2.12\,\mu s$	1.21	2.6187	-6.3130	-1.5304	0.5954
$2.96\,\mu s$	1.21	6.2036	4.1677	-6.0861	2.1380
$3.68\,\mu s$	1.44	8.5899	-8.4205	-6.9225	2.5578
$4.64\,\mu s$	1.96	7.1158	1.0130	-6.5671	2.2122

Table 5.6: Values of the coefficients for even power terms of the Abel inverted polynomial fit of the electron density for the 22 kV channel discharge. Radial coordinate r from 0 cm to 1.0 cm for the equation $N_e(r) = \frac{1}{\pi}\left[\sqrt{\alpha - r^2}\left(a_0 r^0 + a_2 r^2 + a_4 r^4 + a_6 r^6\right)\right]$.

Abel Inverted Electron Density

15 kV discharge , 7 torr N2, 0.5 torr benzene
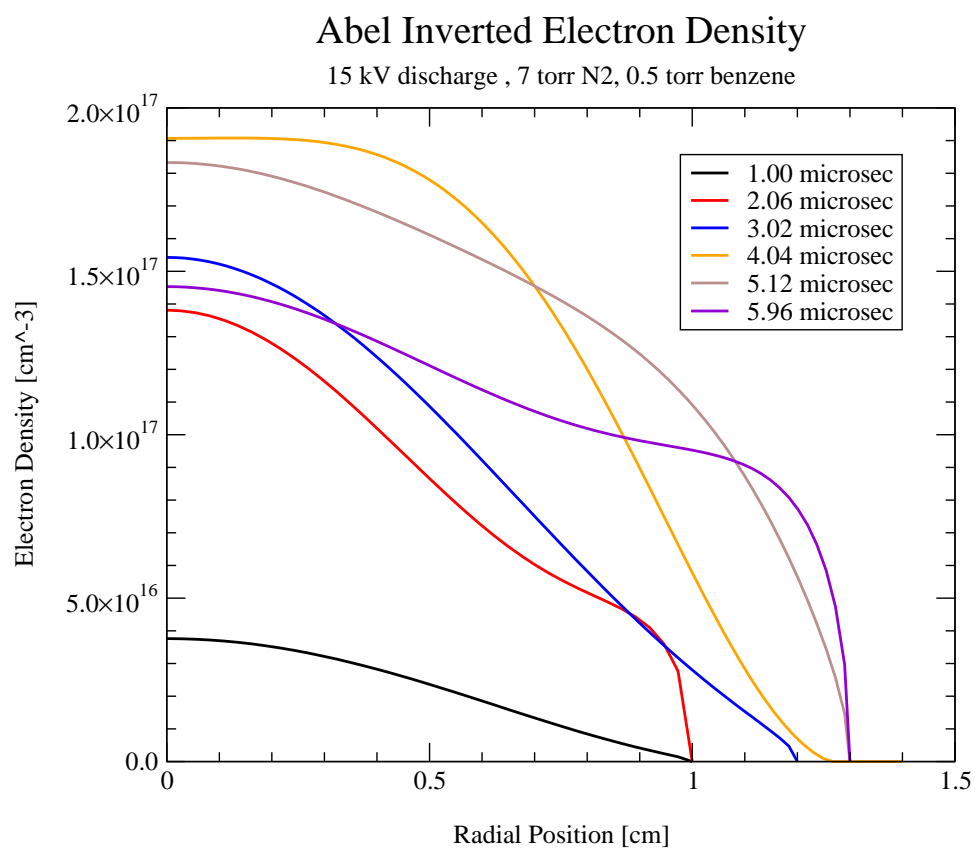
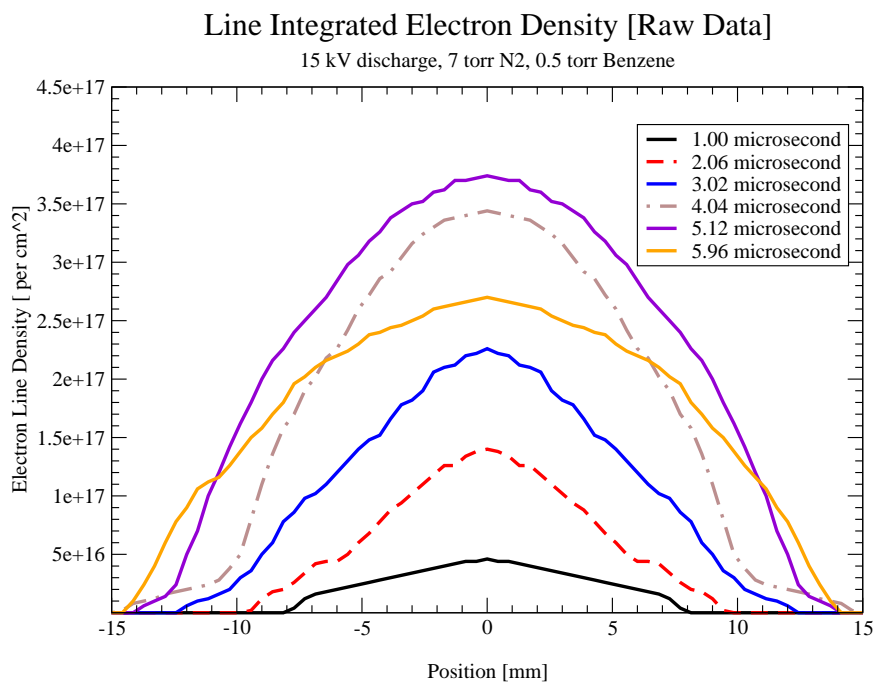

Figure 5.31: Abel inverted electron density of a 15 kV discharge.

109
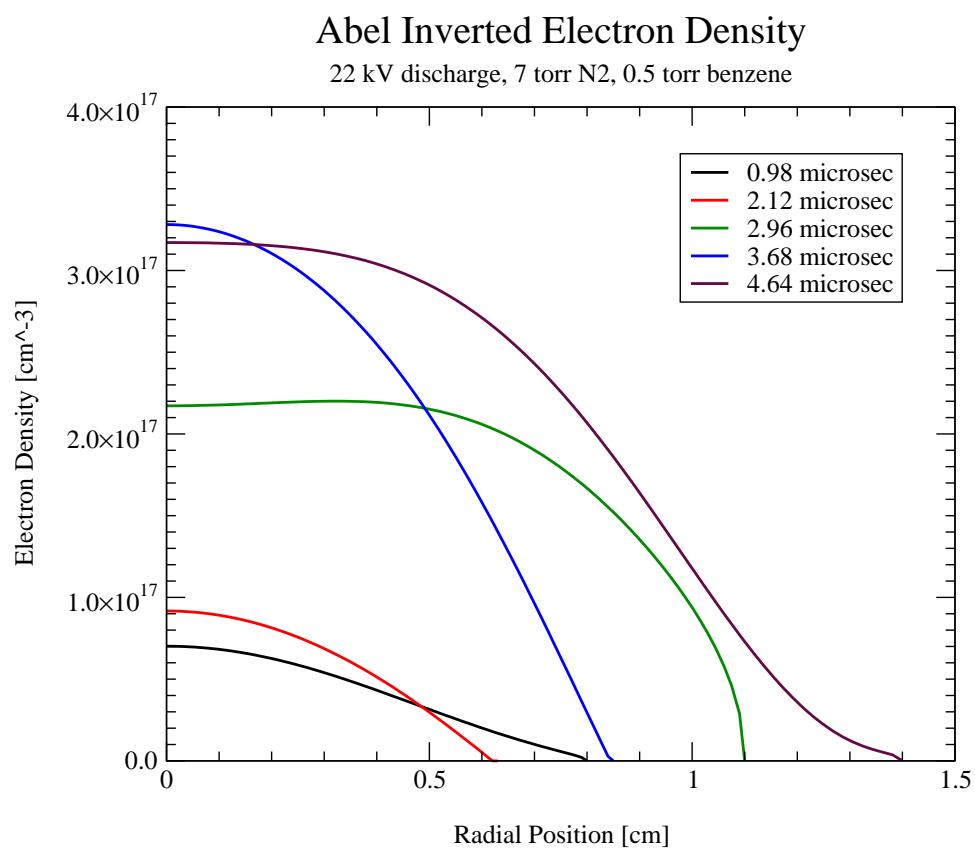
Figure 5.32: Abel inverted electron density of a 22 kV discharge.

15 kV Abel Inverted Electron density [per cm^3]
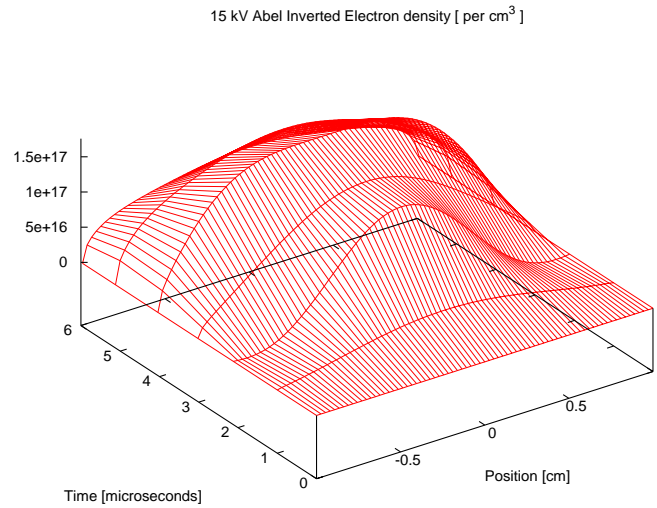
Figure 5.33: Time evolution of the Abel inverted electron density for a 15 kV discharge.

22 kV Abel Inverted Electron density [per cm^3]
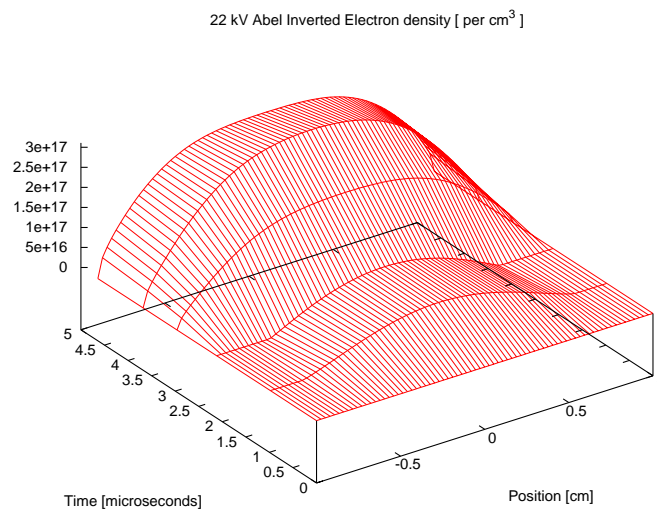
Figure 5.34: Time evolution of the Abel inverted electron density for a 22 kV discharge.
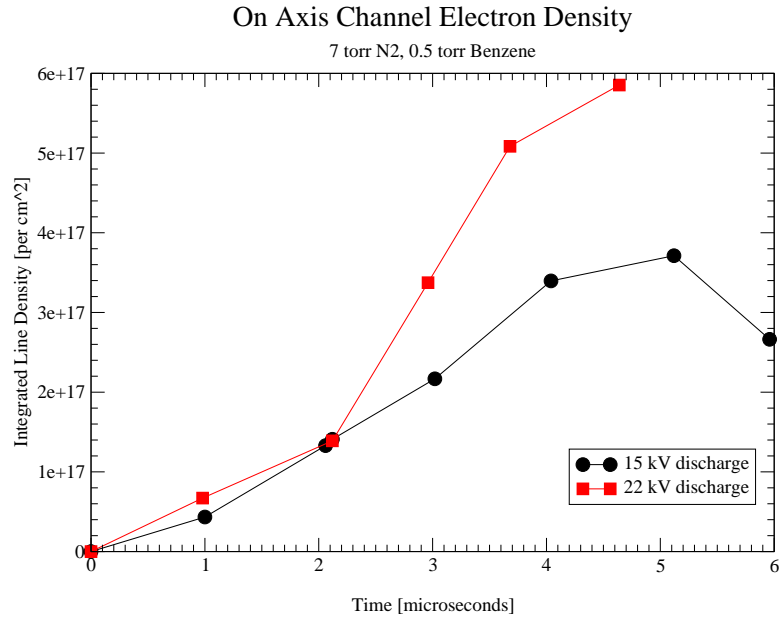
Figure 5.35: On axis value of the line integrated electron density as a function of time for the 15 kV and the 22 kV main bank channels.
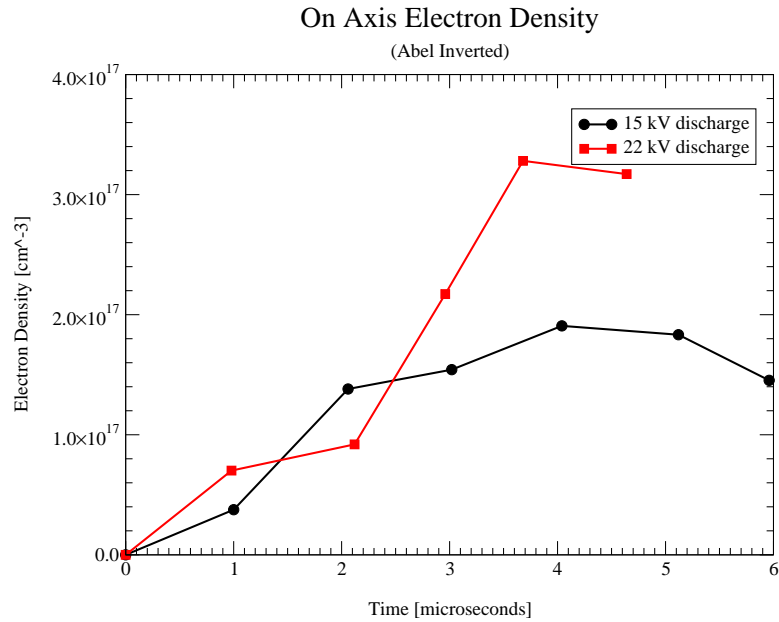
Figure 5.36: On axis value of the Abel inverted electron density as a function of time for the 15 kV and the 22 kV main bank channels.
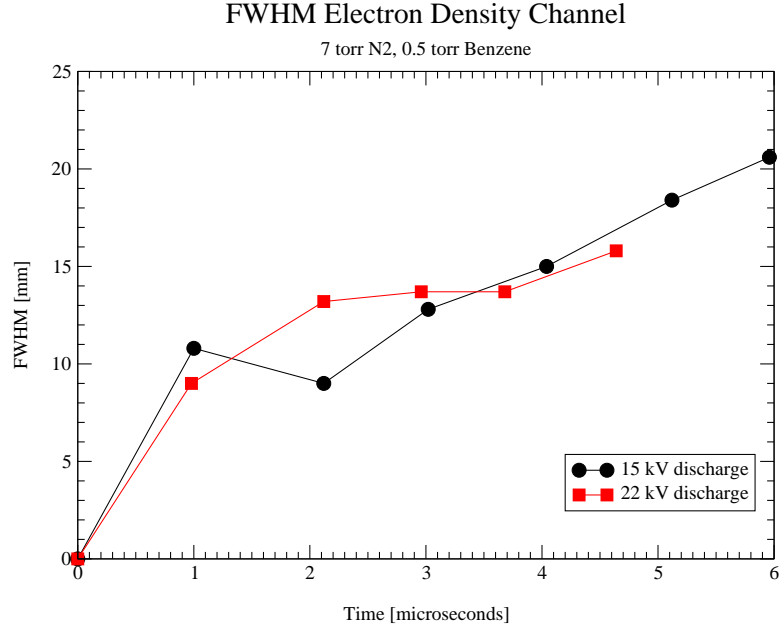
Figure 5.37: Measurement of the channel's electron density FWHM value as a function of time for the 15 kV and the 22 kV main bank channels.

the main bank discharge is initiated. If indeed the pre-pulse depresses the on axis density by one order of magnitude, then the number to compare to the peak on axis electron density is the number of gas molecules at the onset of the main bank discharge. In the absence of a pre-pulse we would have

$$n_{7\,\text{torr}} = \frac{7\,\text{torr}}{760\,\text{torr}} n_{Loschmidt's} = 2.5 \times 10^{17}\,\text{cm}^{-3} \tag{5.9}$$

where $n_{Loschmidt's} = 2.6 \times 10^{19}\,\text{cm}^{-3}$ [30]. In the presence of the gas depression this baseline is shifted down by

$$n_{\text{on-axis}} = \left(\frac{1}{10}\right) \frac{7\,\text{torr}}{760\,\text{torr}} n_{Loschmidt's} = 2.5 \times 10^{16}\,\text{cm}^{-3} \tag{5.10}$$

This number gives a reference for comparison for the measured electron density and gives a guideline for estimating the undergone degree of ionization during the main bank

discharge. Regardless of which baseline we pick, it it certain that the degree of ionization is at least 90%.

5.2.4 Faraday Polarimetry

The intent of the Faraday polarimeter measurement is to determine the magnetic field magnitude and distribution in the main bank z-pinch channel. The results obtained are not definite and more study needs to be conducted. Nevertheless, some meaningful results are obtained. It is important to enumerate the hurdles encountered here in our attempts to conduct the magnetic field measurements.

The minimum measurement value that the instrument can make, according to the discussion in section 4.3, is of 0.002 radians, which is imposed by the electrical noise floor. This implies that the measurement of the channel's inner core is not possible to at most 1 mm from the center, but more important is the fact that the ± 0.002 radians in the measurement uncertainty limits our ability to determine the actual current distribution, since the difference between the rotation induced by a uniform current distribution and a current distribution totally contained in the outer radius of the channel, which are the two extreme cases that can occur, is of the same order as the uncertainty [46]. Perhaps as important is the limitation imposed by the accurate knowledge of the plasma electron density, since after all, the faraday rotation angle depends on the $N_e \vec{B}$ convolution and the errors introduced by both $\vec{B}$ and N_e are also convoluted in the measurement. A best approach can be taken by comparing rotation angles from simulations directly with the generated data, but this does not eliminate the need for an accurate knowledge of the electron density distribution. Another obstacle to contend with is the refraction of the

probe beam as it propagates through the plasma channel. Since the wavelength of the probe beam is $10\,\mu$m, the beam suffers a large deflection that introduces a shift in the detected signal. Compensating optics were placed just before the detectors to minimize the effect, nonetheless, a signal shift of about $100\,$mV remained. The approach used to eliminate the effect was to make two sets of measurements: one with the analyzing polarizers set at the predetermined half shadow angle in order to capture the faraday rotation; the second set of measurements was done with the the analyzing polarizers set with the same orientation such that the only measurable effect was the one produced by the beam deflection. The sets were subtracted and the results presented in the following section.

It is fair to mention that this particular measurement is one of the most challenging experiments in the field. Different techniques have been proposed to measure the magnetic field in plasmas and almost all of them rely on having present very strong magnetic fields ($> 1\,$T) and/or very high electron densities ($\gg 10^{17}\,$cm^{-3}) [65] [41] [38] [31]. There is a technique designed to measure smaller magnetic fields through the process called laser induced fluorescence (LIF) [47] that might produce better results, but is a technique that requires ample time and resources to set up.

5.2.5 Magnetic Field Data Analysis

The presentation that follows here is an attempt to make complete measurement of the magnetic field of the plasma channel. As said before, the accuracy of these measurements are hindered by many factors and the results should be approached with a qualitative mind set. They will give an order of magnitude estimate on the channel's magnetic field and it will hint at the possible current distribution within the channel.
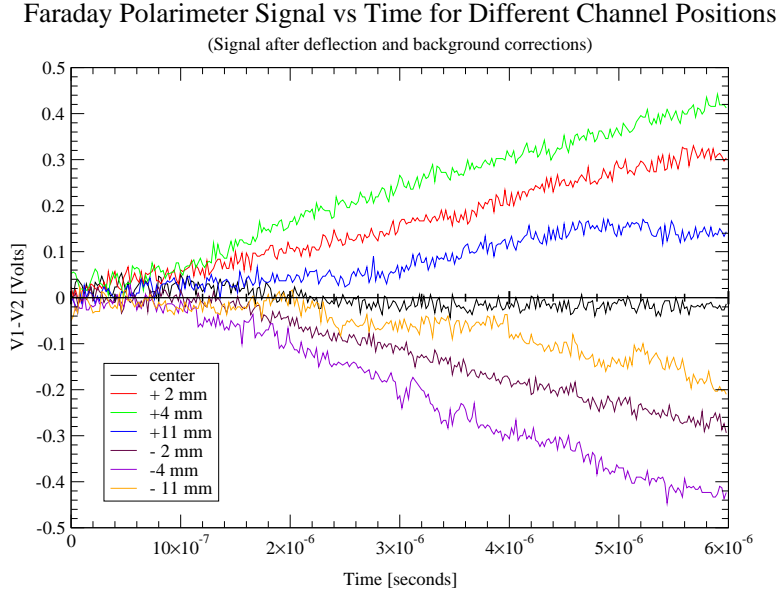
Figure 5.38: Faraday effect polarimeter signal V1-V2, for a 7 torr N2 discharge, 1 torr benzene. The conversion factor to angular measure is 2.822×10^{-2} radians per volt.

Figure 5.38 shows the data collected from the polarimeter. This data has been corrected for the deflection effects that the probe beam has suffered. The plot shows the detector signal difference as a function of time. Each trace represents an average of three main bank channel discharges with the probe beam looking at a particular radial position. Measurements were done at the center, ± 2 mm, ± 4 mm, and ± 11 mm. These seven traces represent a total of 63 channel shots all to accommodate the deflection effect corrections [1]. From this data we can generate a plot of rotation angle θ [2] as a function of radial position. This plot is shown in figure 5.39. I proceeded to fit the data set of figure 5.39 with an equation of the form $y = a_0 x e^{-a_1 x^2}$, which is the form of the resultant function in figure 4.9 when the faraday rotation is generated by the convolution of a directly proportional function with a gaussian function. This would correspond to a uniform current distribution

***

[1] The measurements for the shots performed fall into three categories: $(V_1 - V_2)$, $(V_1 + V_2)$, and null

[2] $(V_1 - V_2)$
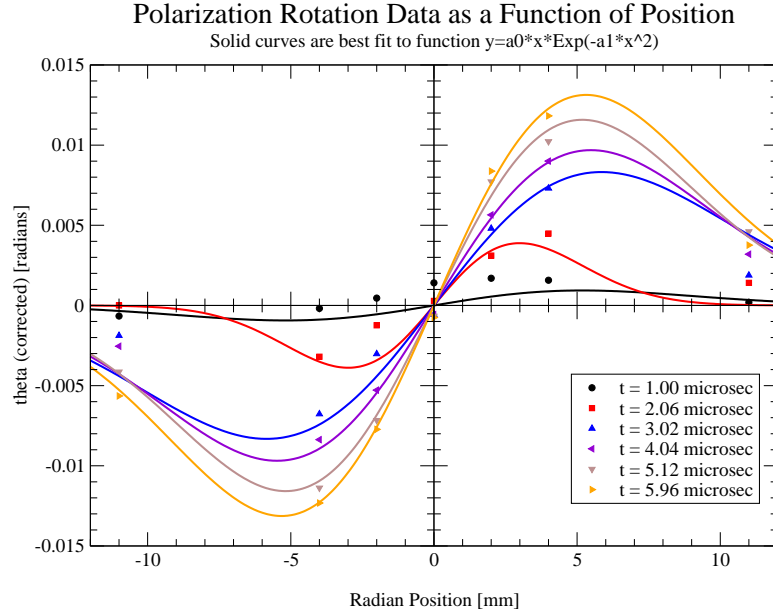
Figure 5.39: Faraday effect polarimeter signal V1-V2, for a 7 torr N2 discharge, 1 torr benzene fitted to $y = a_0 x e^{-a_1 x^2}$. The conversion factor to angular measure is 2.822×10^{-2} radians per volt.

within the channel and a gaussian electron density. This generates the coefficient values of table 5.7

From table 5.7 we compute the Θ function which is shown in figure 5.40. These are the functions that will undergo Abel inversion to generate the $F(r)$ function. The result of the Abel deconvolution is shown in table 5.8.

From the function $F(r)$ the values of $r\,B_\theta$ are evaluated for the discrete radial position points of 0 mm, ± 2 mm, ± 4 mm, and ± 11 mm. These values are presented in figure 5.41. The enclosed current values at $r = \infty$ were determined from the current waveforms for each particular time. A piecewise continuous function was fitted to the data points, where a quadratic function was used for values of r less than or equal to the channel radius as defined by the electron density interferograms. The fit is shown by the solid lines in figure

15 kV Main Bank Faraday Rotation Fit

Time [μs]	a_0 [mm^{-1}]	a_1 [mm^{-2}]
	Coefficients for $\theta = a_0 y e^{-a_1 y^2}$ [radians]	
1.00	2.974×10^{-4}	1.863×10^{-2}
2.06	2.137×10^{-3}	5.566×10^{-2}
3.02	2.345×10^{-3}	1.461×10^{-2}
4.04	2.913×10^{-3}	1.664×10^{-2}
5.12	3.684×10^{-3}	1.862×10^{-2}
5.96	4.072×10^{-3}	1.769×10^{-2}

Table 5.7: Values of a_0 and a_1 for the data fit in figure 5.39 for the 15 kV channel discharge. The fitted equation is of the form $y = a_0 x e^{-a_1 x^2}$. Radial coordinate y from 0 mm to 10.0 mm. The conversion factor to angular measure is 2.822×10^{-2} radians per volt.

Theta-over-y Function Generated from Rotation Data

theta/y = a0*Exp[-a1*x^2]
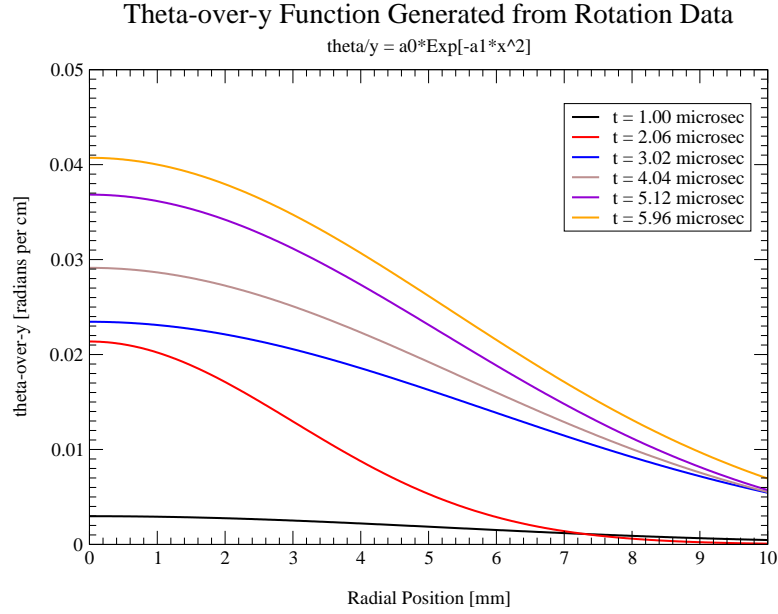
Figure 5.40: Θ function generated from the $y = a_0 x \exp(-a_1 x^2)$ fit of figure 5.39 data. Coefficients used are those of table 5.7

5.41. We can see from the figure that is very plausible to have $> 70\%$ of the channel current within the plasma channel as defined by the FWHM of the electron density distribution. While we cannot make a positive assessment of the current distribution within the channel, the data does suggest that a uniform distribution is very much possible. Also ion beam experiment results held at GSI in germany are consistent with a uniform current density distribution over such z-pinch discharges [45].

The fitted enclosed current curves then generate the magnetic field distribution shown in figures 5.42 and 5.43. From this plot a couple of interesting details need some attention. The magnetic field seems to be rather strong in the initial few microseconds of the channel discharge. Although the current is relatively small, the channel diameter is also small and the magnetic field does not diffuse appreciably outside of the plasma. In fact, the magnetic field stays frozen in the plasma and it expands at the same rate. Of course, this

15 kV Main Bank Function $F(r)$ generated by fit

	Coefficients for $F(r) = a_0 e^{-a_1 r^2}$ $[\,\mathrm{cm}^{-2}]$	
Time $[\,\mu s]$	a_0 $[\,\mathrm{cm}^{-2}]$	a_1 $[\,\mathrm{cm}^{-2}]$
1.00	2.29019×10^{-3}	1.863
2.06	2.84447×10^{-2}	5.566
3.02	1.59916×10^{-2}	1.461
4.04	2.12003×10^{-2}	1.664
5.12	2.83618×10^{-2}	1.862
5.96	3.05559×10^{-2}	1.769

Table 5.8: Coefficient values of a_0 and a_1 for the Abel inverted magnetic field function $F(r)$ as defined in equation (4.28). Radial coordinate r from $0\,\mathrm{cm}$ to $1.0\,\mathrm{cm}$. $F(r)$ is of the form $F(r) = a_0 \exp[-a_1 x^2]$.

Enclosed Current (rBtheta) for 15 kV Discharge

7 torr nitrogen, 0.5 torr benzene
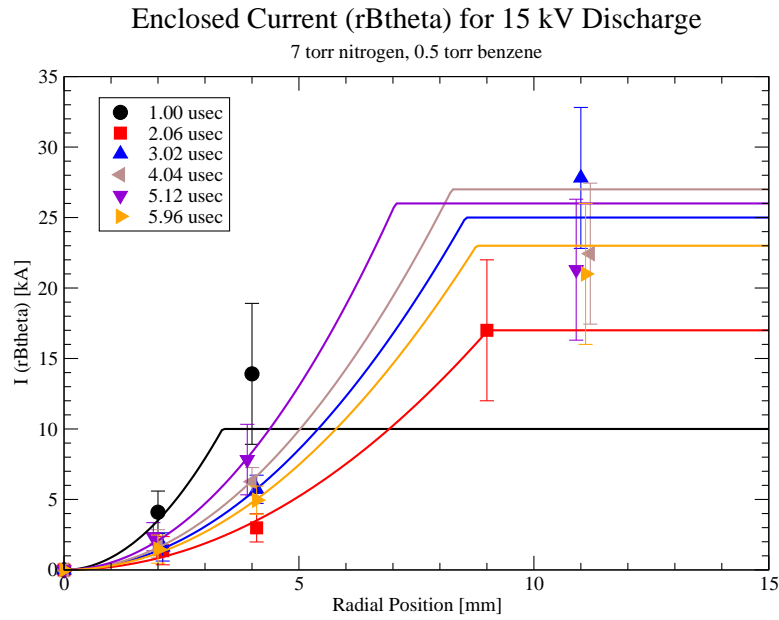
Figure 5.41: Enclosed channel current for a 15 kV discharge. Points are experimental that are best fit assuming uniform current density distribution inside the plasma channel.

Magnetic Field Distribution

Generated from Enclosed Current plot
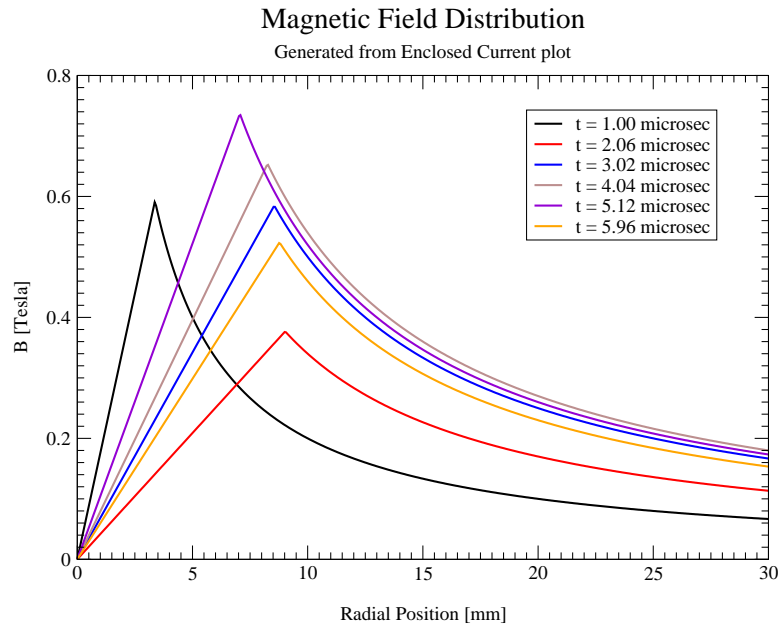
Figure 5.42: $B_\theta(r)$ function generated from enclosed current plot in figure 5.41.

15 kV Magnetic Field Evolution [T]
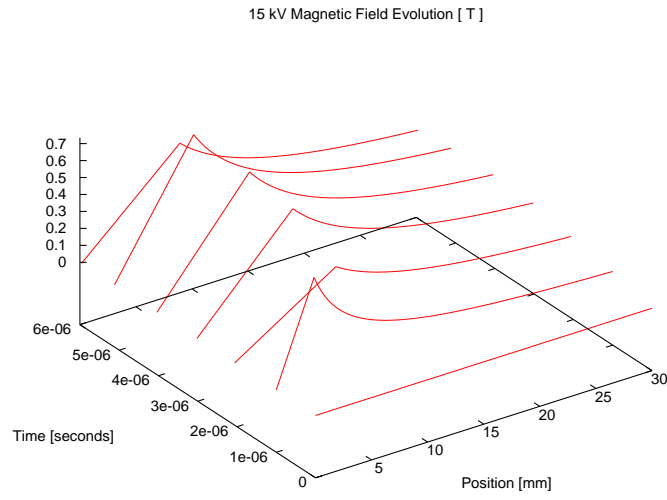
Figure 5.43: $B_\theta(r)$ time evolution generated from the experimental data.

might be an artifact introduced by the analysis and calculation, but it is interesting to see, as we shall see soon, the simulation runs predict the same behavior.

Chapter 6

Theory and Simulation

This chapter will serve for an initial comparison between the experimental data set and CYCLOPS. CYCLOPS is a computer code designed to simulate a plasma channel for use as a final focus element in a heavy ion fusion driver. The code is based on a one spatial dimension phenomenological model with initial conditions set to match the laser assisted pre-ionization process. The code itself solves hydrodynamic and atomic quantities as a function of time with a fifth order Runge-Kutta integrator and the field quantities are solved with a time centered implicit field solver. The main features of the code include single fluid Lagrangian hydrodynamics, electron dynamics done through a scalar conductivity model. Electromagnetic fields calculations are done using the implicitly solved magnetic diffusion equation. The code also features a simple avalanche model that includes recombination processes. The external electrical circuit is modeled through a bulk RLC model with a variable delay switching.

The main assumptions made are high collisionality, ideal gas equation of state,

and negligible displacement current. The initial version of the code also had negligible plasma recombination and negligible benzene effects on the gas chemistry and recombination quenching, but as we have seen through the experiments that these two assumptions need to be revised and the additional physics implemented accordingly into the code.

6.1 Equations used in CYCLOPS

Since CYCLOPS is a Lagrangian fluid code, the physical quantities are determined with respect to moving grid points. The code models a cylindrical chamber of radius R_{cell} and length l_{cell}. All quantities are only dependent on time and the radial distance r from the axis of the cell. The dynamical equations to be stepped forward in time are:

$$\frac{dr}{dt} = V_r \tag{6.1}$$

$$\rho \frac{dV_r}{dt} = \left(\vec{J} \times \vec{B} \right)_r - \frac{\partial P}{\partial r} - \frac{\partial q}{\partial r} \tag{6.2}$$

$$\rho \frac{d\epsilon}{dt} = \vec{J} \cdot \vec{E} - (P + q) \frac{1}{r} \frac{\partial (rV_r)}{\partial r} - 5.16\text{x}10^{-18}\alpha\eta_{\text{e}} - \frac{\sigma_{\text{sb}}T^4}{l^{\text{l}}} + \frac{1}{r} \frac{\partial}{\partial r} K_{\text{th}} \frac{\partial T}{\partial r} \tag{6.3}$$

$$\frac{1}{\eta_{\text{e}}} \frac{d\eta_{\text{e}}}{dt} = -\frac{1}{r} \frac{\partial (rV_r)}{\partial r} + \alpha - \alpha_{\text{r}}\eta_{\text{e}} \left(\frac{308}{T} \right)^{0.4} \tag{6.4}$$

$$\frac{dB_\theta}{dt} = \frac{1}{\mu_0} \frac{\partial}{\partial r} \frac{1}{r\sigma} \frac{\partial (rB_\theta)}{\partial r} - B_\theta \frac{\partial V}{\partial r} \tag{6.5}$$

SI units are used everywhere. Equation (6.1) merely states that the time derivative of a radial grid point is equal to the velocity V of that grid point. Equation (6.2) determines the acceleration of the grid points. ρ is the mass density of the gas, J is the current density, B is the magnetic field, P is the gas pressure, q is the artificial viscosity coefficient. Equation (6.3) is a gas energy balance equation, where ϵ is the specific energy of the gas and is proportional to the gas temperature divided by the mass of the molecules. The first term of equation (6.3) is the Joule heating term and the second term is due to convection. The third term is due to the creation of electrons through avalanching with α as the avalanche coefficient and η_e the electron number density. The fourth term is due to radiation. σ_{sb} is the Stephan-Boltzmann constant equal to 5.6703×10^{-8} ($JK^{-4}m^{-2}s^{-1}$) and l is the Plank mean length. The fifth term is thermal conduction and K_{th} is the thermal conduction coefficient.

Equation (6.4) describes the production of electrons. The first term is a convection term and the second term is due to avalanching. The third term is recombination appropriate for nitrogen molecules with α_r the recombination coefficient.

Equation (6.5) is the magnetic diffusion equation which is derived from Maxwell's equations ignoring the displacement current and charge sources. The solution of the five differential equations consists of two parts. Equations (6.1)-(6.4) are integrated with a Runge-Kutta algorithm. Equation (6.5) is then leap-frogged with the other four with a time centered implicit scheme.

CYCLOPS is a work-in-progress code and the code itself is still in a trial and verification stage. CYCLOPS is intended to support further channel experiments in beam

neutralization that have relevance at GSI and LBNL. For more details on the algorithms and the code itself the reader is referred to appendix D.

6.2   Pre-pulse

The initial comparisons made are between the *LRC* bulk component model of the code and the experimental pre-pulse current and voltage discharge waveforms. Figure 6.1 and figure 6.2 show these waveforms for a pre-pulse discharge in a neon gas fill and for a nitrogen gas fill respectively.

The simulation fit to the experiment is better for the neon pre-pulse than for nitrogen. From the simulation's perspective this can be attributed to the fact that the physics of neon is simpler and better understood than that for molecular nitrogen. Molecular dissociation seems to play a significant role since there is significant current damping for nitrogen as compared to that of neon. Simulation fails to reproduce this effect and it is more noticeable in the nitrogen run.

We can see this also from the energetics point of view. Figure 6.3 shows the instantaneous electrical discharge power on the top plot and the shock wave expansion in the bottom. Comparisons between experiment and simulation are included. Simulation predicts less power coupled to the channel than the experiments show. Also we see that the experiment exhibits negligible energy been stored in the produced magnetic field.

From the shock wave front expansion comparison plot we see that the expansion initiates very much the same, but the shock front slows down in the simulation, consequence of the smaller energy deposition.
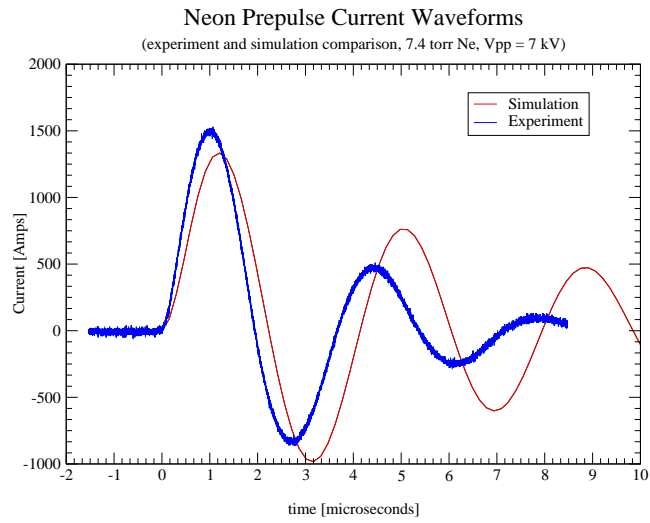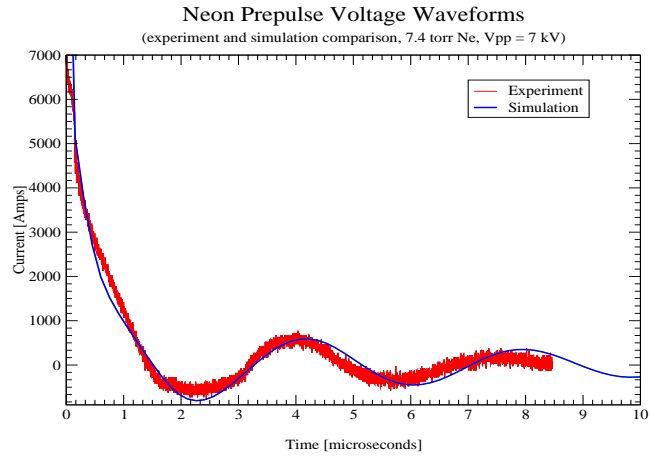
Figure 6.1: Simulation and experiment comparison: Pre-pulse neon waveforms.
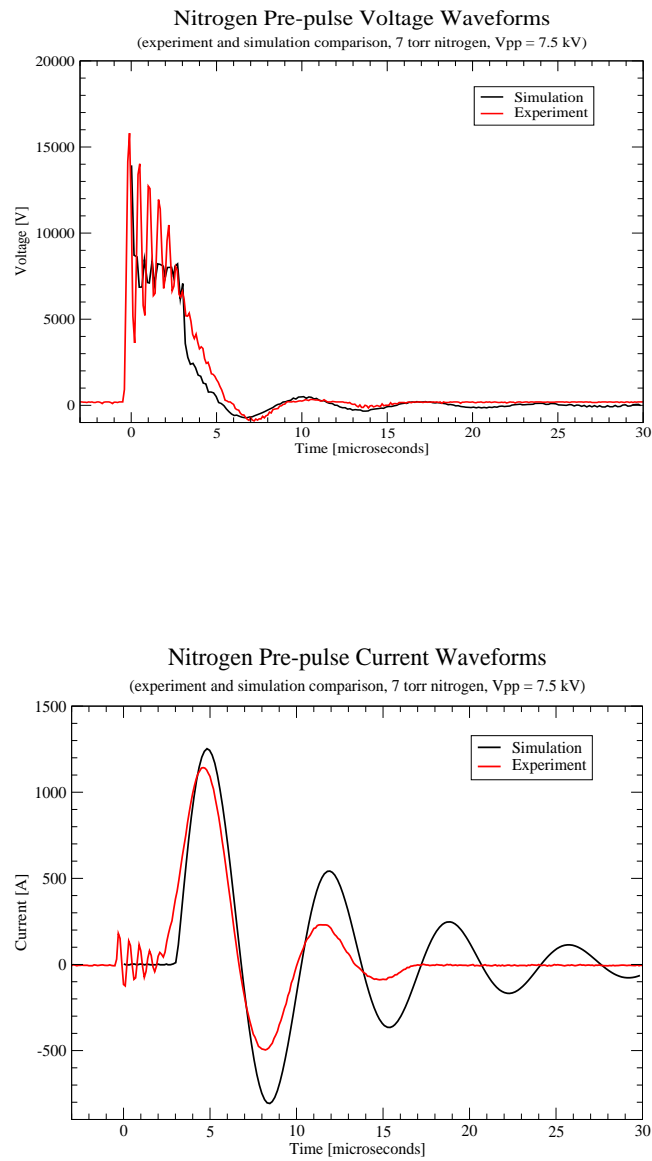
Figure 6.2: Simulation and experiment comparison: Pre-pulse nitrogen waveforms.
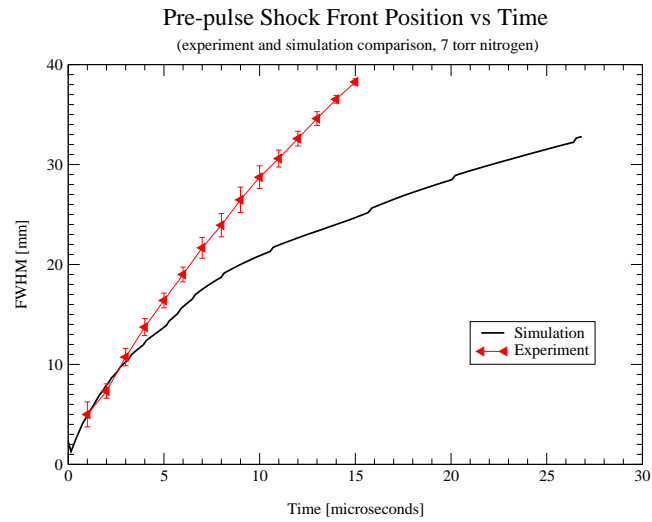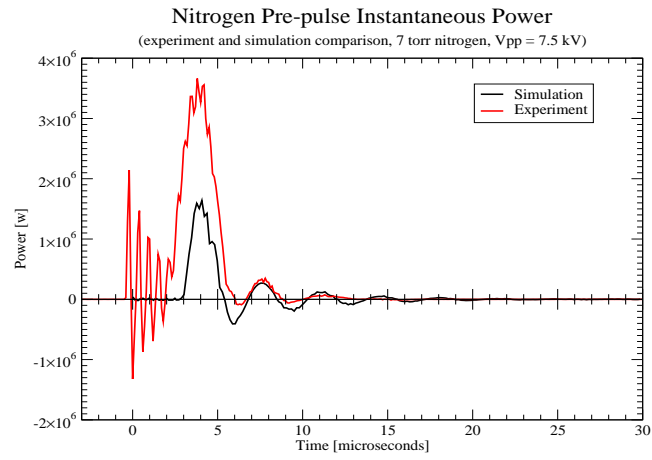
Figure 6.3: Simulation and experiment comparison: Pre-pulse discharge power and shock front.
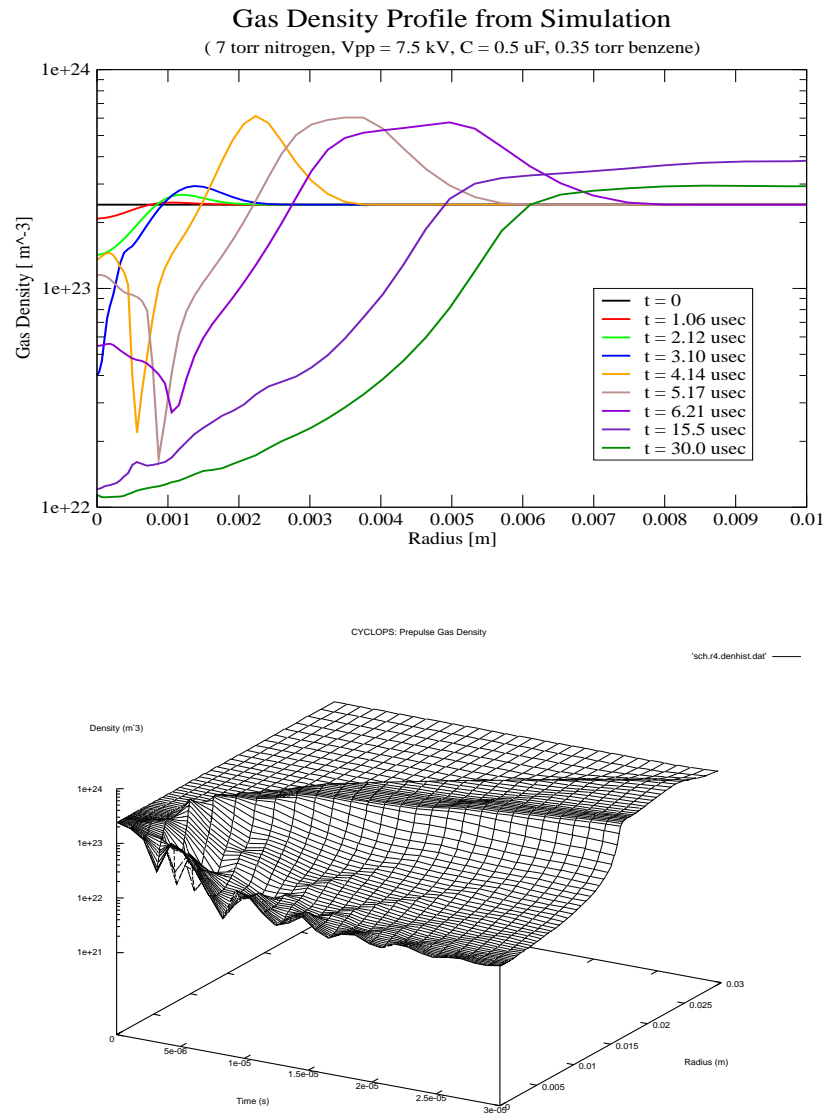
Figure 6.4: Simulation results for pre-pulse density depression in nitrogen.

All things considered, qualitative agreement is very good and it is expected that the results from the simulation underestimates the density depression left by the pre-pulse discharge. This result is shown in figure 6.4. Since the pre-pulse is hydrodynamically dominated the electromagnetic influence is negligible and this significantly simplifies the code's calculations and the results reflect better the experimental data.

6.3   Main Bank

Figure 6.5 show the voltage and current waveforms for the main bank and as far as qualitative agreement goes, it all looks good. Quantitatively, on the other hand, there are some discrepancies and more detail physics need to be incorporated, especially in the plasma conductivity model. Figure 6.6 shows the instantaneous power delivered by the main bank pulser with a net energy dissipation of $\sim 100\,\mathrm{J}$ over $8\,\mu\mathrm{s}$. Both the simulation and experiment agree well.

The major discrepancy found is in the generated electron density. This can be seen in figure 6.7. While the overall footprint of the electron density agrees between the experiment and the simulation ($\sim 1.2\,\mathrm{cm}$), the electron density distribution itself is very different. The overall total number of electrons is similar but it is obvious that the avalanching model needs revision.

Surprisingly enough the current distribution is similar between the experiment and the simulation, as it is seen by analyzing the magnetic field comparison in figure 6.8. This result is rather encouraging since the channel's utility to transport an ion beam relies on this distribution and proper predictions done by simulations is critical.
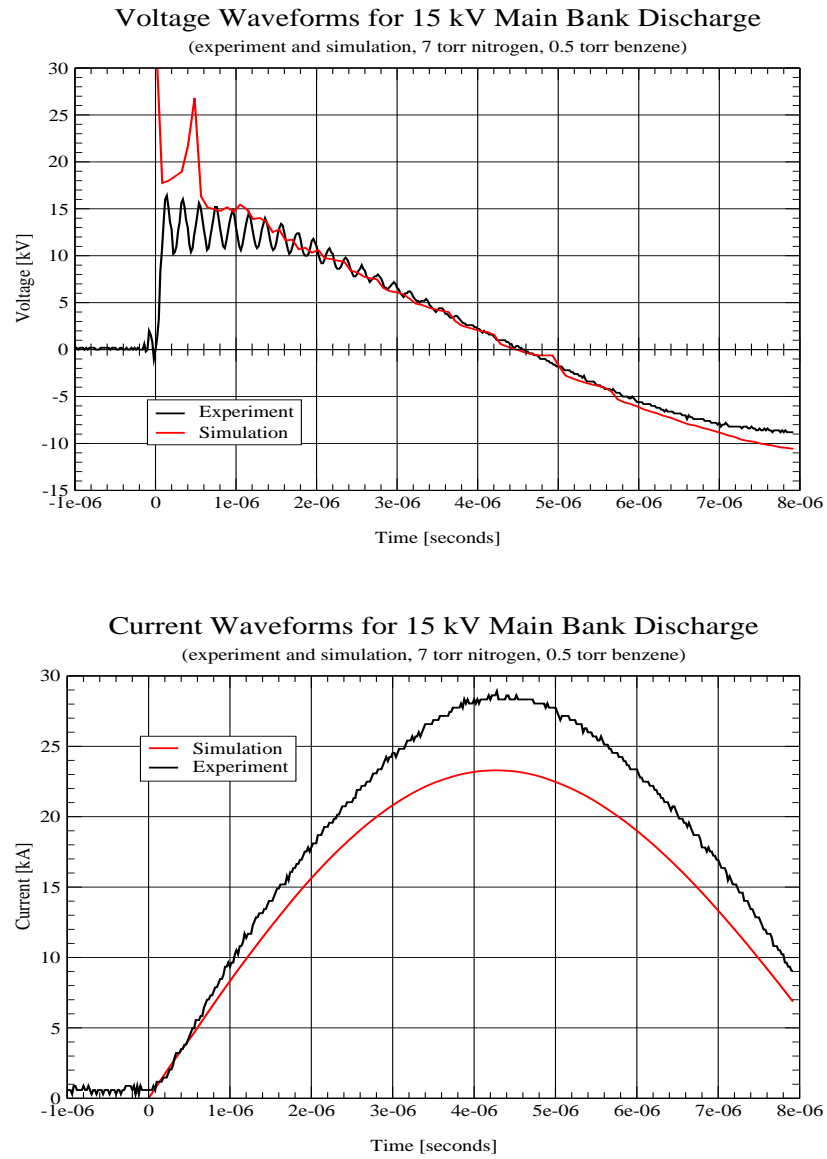
Figure 6.5: Simulation and experiment comparison: Nitrogen waveforms for the main bank discharge.
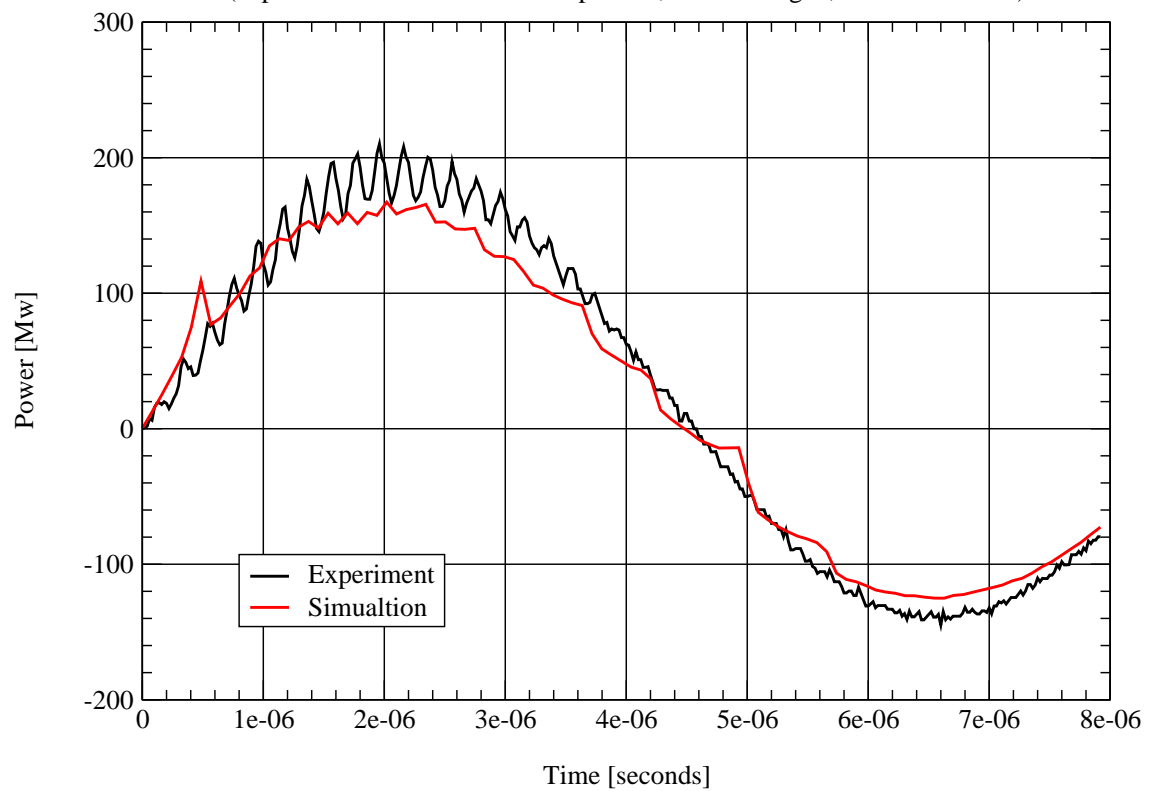
Figure 6.6: Simulation and experiment comparison: Electrical pulsed power.
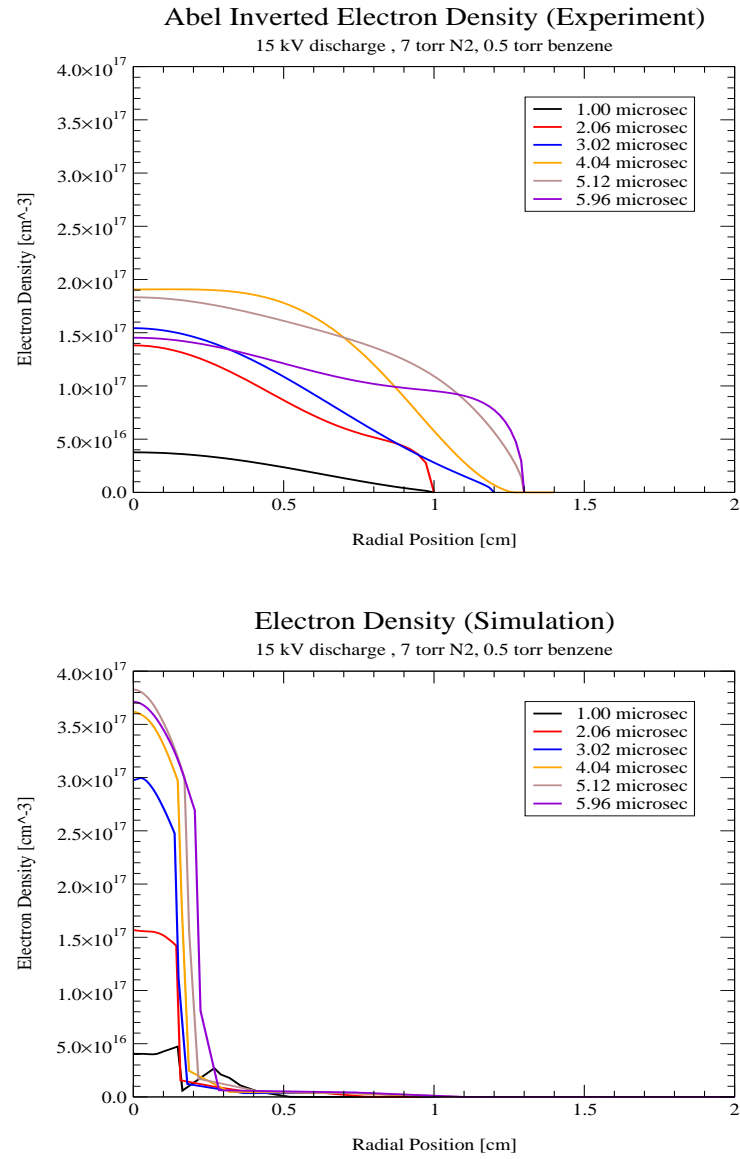
Figure 6.7: Simulation and experiment comparison: Electron density distribution.
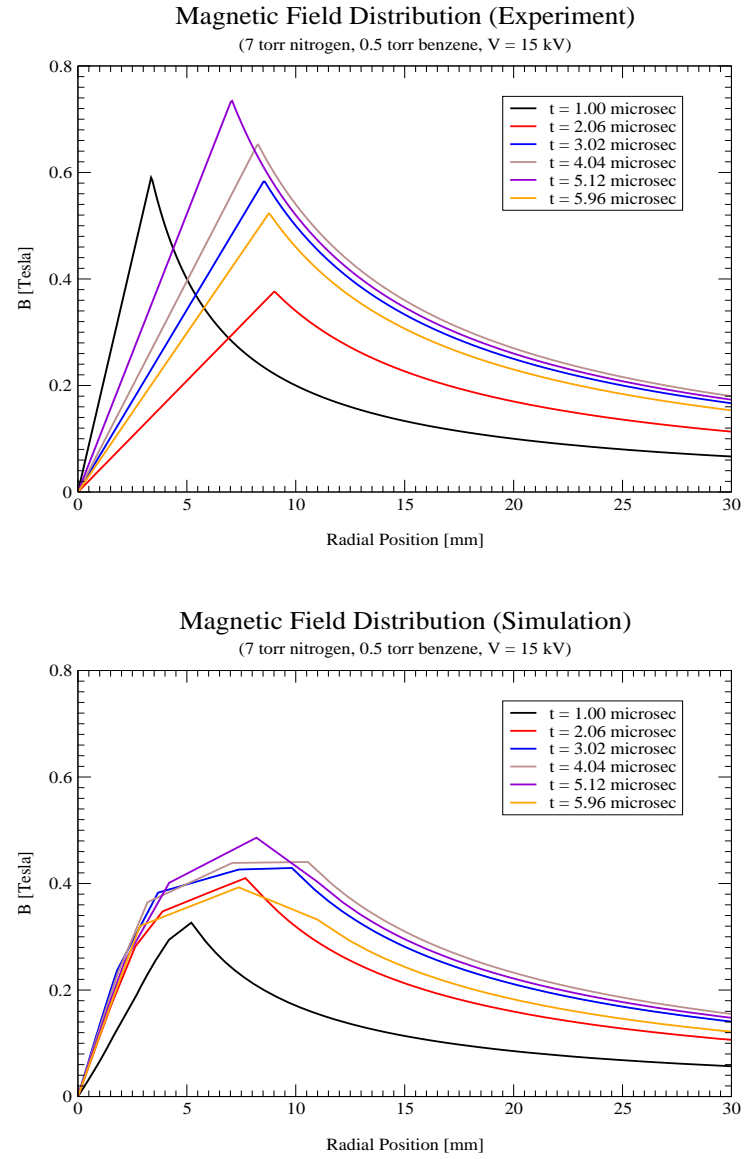
Figure 6.8: Simulation and experiment comparison: Magnetic field distribution.

It is clear that the CYCLOPS incorporates already the necessary physics to describe the mechanisms in which the channel forms and evolves, nevertheless the atomic physics models are still in their rudimentary stage. Although BUCKY might be a more robust code, the one advantage of CYCLOPS over BUCKY is the inclusion of an avalanche model. It might be worthwhile to cross-validate CYCLOPS with BUCKY.

Chapter 7

Summary and Conclusion

This study focused on the dynamics of a plasma channel z-pinch experiment at LBNL. The channel under study was laser initiated and produced in a 7 torr nitrogen gas fill with a 0.5 torr partial fill of benzene to enhance laser absorption for initial seed electron production. The original questions that needed answer are related to understanding the mechanisms that allowed for MHD stable z-pinch channels that carried currents in excess of 50 kA. Also of prime importance was to investigate the plasma conductivity and current distribution in the plasma channel since this is a critical parameter for effective ion beam transport.

Experiments conducted showed that the effect of the pre-pulse was to set-up the initial conditions for the main bank by creating a stabilizing wall through a gas density depression-ridge produced by the pre-pulse shockwave and hydrodynamic expansion. A gas temperature upper bound of $\sim 0.5\,\mathrm{eV}$ and an on axis gas density depression with a ratio of 10 to 1 referred to the undisturbed level are left as initial conditions for the main bank

discharge. This provides for outstanding reproducibility and for MHD stabilization during the first $8\,\mu$s of the channel's life providing enough time for ion beam transport.

Electron density measurements give an indication at the channel's conductivity and possible regions of current distribution. Magnetic field measurements showed that $> 70\%$ of the channel current is contained in the channel's core, although the experiments where unable to determine the exact current distribution inside the channel's core. On the other hand, both experiment and simulation indicate that the possibility of uniform current density is high.

As a secondary goal, the experiments conducted produced necessary data needed to validate the 1-d Lagrangian code CYCLOPS that is being developed at LBNL. Besides the results listed above, experiment that under the experimental conditions, z-pinch channel electron densities reach on-axis peak values of $1.5 \times 10^{17}\,\mathrm{cm}^{-3}$ for a $15\,\mathrm{kV}$ discharge and $3.2 \times 10^{17}\,\mathrm{cm}^{-3}$ for $22\,\mathrm{kV}$ discharge with pinch times around $2\,\mu$s.

Since benzene was used as an absorption medium for the ionizing laser radiation, a phenomenological study was done and has pointed at the importance of the inclusion of the benzene and related atomic physics into the simulation codes.

Overall, the mechanisms for the production of these stable channels are understood. This is shown through the results given by CYCLOPS. It is evident that more work needs to be done in the simulation arena.

Also of importance are the beam-channel interactions that need to be addressed to validate if indeed the plasma channel is a viable HIF transport. Favorable experimental data exists in which a beam has indeed been transported, but these beams don't fall in the

appropriate particle intensity-energy parameter space. As of the time of this writing, no appropriate beam exists. Hence one has to rely on simulations. Some simulation studies that focus on this issue are been done. One of them is the beam interaction study using IPROP 3-D code which is a particle in cell code. Preliminary results are encouraging in which an intense beam is propagated and there is no evidence of filamentation, hose, or axisymmetric transport. Nevertheless it is still necessary to do an experimental study.

I have realized, through the writing of this document, that I have only scratched the surface of this topic and that more needs to be done. As far as the HIF effort is concerned, a larger scale experiment needs to be done to determine the limitations that the increased channel induction will produce on the peak currents as well as studies on the channel-channel interaction to investigate the forces acting in the vicinity of the target region. Important beam-channel interactions need to be carried out to investigate two stream instability and filamentation issues as well as beam neutralization and plasma-beam-particle interactions. Of course, a suitable accelerator producing an intense beam with the right characteristics needs to come on line.

From the point of view of the z-pinch itself, a thorough core temperature study would complement nicely the data set. Present experiments at GSI offer a great opportunity to further the understanding of these plasma channels. A set of experiments should also be conducted in other noble gases such as argon and xenon.

It is hoped by the author that the present document serve as a stepping stone for others to continue on expanding on the topic.

Bibliography

[1] S. Alexiou and Y. Maron. Theoretically based closed form formulas for the collision operator for isolated ion lines in the standard Stark-broadening theory. *Journal of Quant. Spectrosc. Radiat. Transfer*, 53(1):109–124, 1995.

[2] R. A. Alpher and D. R. White. Optical refractivity of high temperature gases. I. Effects resulting from dissociation of diatomic gases. II. Effects resulting from ionization of monoatomic gases. *The Physics of Fluids*, 2(2):153–169, March-April 1959.

[3] G. Arfken. *Mathematical Methods for Physicists*. Academic Press, Inc., San Diego, CA., 1985.

[4] M. S. Armel. *Atomic Processes for Heavy Ion Inertial Fusion*. PhD thesis, University of California, Berkeley, 2000.

[5] R. O. Bangerter. Targets for heavy ion fusion. *Fusion Technology*, 13:348–355, 1988.

[6] R. O. Bangerter. Ion beam fusion. *Phil. Trans R. Soc. Lond. A*, 357:575–593, 1999.

[7] N. O. Barboza. *Heavy Ion Beam Propagation Through a Gas-Filled Chamber for Inertial Confinement Fusion*. PhD thesis, University of California, Berkeley, 1996.

[8] W. H. Bennett. Magnetically self-focussing streams. *Physical Review*, 45:890–897, 1933.

[9] E. Boggasch, J. Jacoby, H. Wahl, et al. z-pinch plasma lens focusing of a heavy-ion beam. *Physical Review Letters*, 66(13):1705–1708, April 1991.

[10] M. Born and E. Wolf. *Principles of Optics: Electromagnetic Theory of Propagation, Interference and Diffraction of Light.* Pergamon Press, Oxford, 1980.

[11] R. Bruzzese, A. Sasso, and S. Solimeno. Multiphoton excitation and ionization of atoms and molecules. *Rivista del Nuovo Cimento*, 12(7):1–105, 1989.

[12] H.L. Buchanan. Mathematical models for the EPIC code. Technical Report UCID 19055, Lawrence Livermore National Laboratory, June 1981.

[13] L. C. Burkhardt, R. E. Dunaway, J. W. Mather, et al. Pinch effect. *Journal of Applied Physics*, 28(5):519–521, May 1957.

[14] D. A. Callahan and M. Tabak. Target designs for an inertial fusion energy power plant driven by heavy ions. In *Proceedings of the 2nd International Conference on Inertial Fusion Sciences and Applications*, Kyoto, Japan, September 2001.

[15] F. F. Chen. *Introduction to Plasma Physics and Controlled Fusion*, volume 1. Plenum Press, New York, New York, second edition, 1984.

[16] E.Boggash, J. Jacoby, A. Tauschwitz, et al. Plasma lenses for heavy-ion-beam focusing. *Particle Accelerators*, 38-38:89–95, 1992.

[17] D. A. Edwards and M. J. Syphers. *An Introduction to the Physics of High Energy Accelerators.* John Wiley and Sons, New York, New York, 1993.

[18] I. S. Falconer and S. A. Ramsden. Measurement of the faraday rotation of a laser beam passing through a θ-pinch plasma. *Journal of Applied Physics*, 39(7):3449–3458, June 1968.

[19] W. M. Fawley and S. S. Yu. Neon channel chemistry parameters. Beam Physics Memo 45, Lawrence Livermore National Laboratory, November 1982.

[20] T. J. Fessenden and M. C. Vella. Plasma pinch for transport of HIF beams. Technical Report HIFAR-474, Lawrence Berkeley National Laboratory, June 1997.

[21] K. H. Finken, G. Bertschinger, and R. S. Hornady. Schlieren measurements of a high density z-pinch. *Z. Naturforsch*, 31:1318–1323, 1976.

[22] A.M. Frank, S.S. Yu, and J.A. Masamitsu. Inductive electric field effects on optical emissions from the interaction of an intense relativistic electron beam with nitrogen. draft, Lawrence Livermore National Laboratory, ca. 1980.

[23] C. A. Frost, J. R. Woodworth, J. N. Olsen, and T. A. Green. Plasma channel formation with ultraviolet lasers. *Applied Physics Letters*, 41(9):813–815, November 1982.

[24] R. D. Gill. *Plasma Physics and Nuclear Fusion Research.* Academic Press, London, England, 1981.

[25] N. Gottardi. Evaluation of electron density profiles in plasmas from integrated measurements. *Journal of Applied Physics*, 50(4):2647–2651, April 1979.

[26] R. Govil. *Return Current Effects in Passive Plasma Lenses for Relativistic Electron Beams.* PhD thesis, University of California, Berkeley, 1998.

[27] M. A. Heald and C. B. Wharton. *Plasma Diagnostics with Microwaves.* John Wiley and Sons Inc., New York, 1965.

[28] D. Hinshelwood. Development of wall-stabilized z discharges for intense ion-beam transport in inertial confinement fusion facilities. *Journal of Applied Physics*, 72(10):4581–4595, November 1992.

[29] D. W. Holder, R. J. North, and G. P. Wood. AGARDograph: Optical Methods for Examining the Flow in High-Speed Wind Tunnel. Technical Report 23, Advisory group for aeronautical research and development, Norht Atlantic Treaty Organization, November 1956.

[30] J.D. Huba, editor. *NRL Plasma formulary.* Number NRL/PU/6790–98-358 in Beam Physics Branch. Naval Research Laboratory, 1998.

[31] R. H. Huddlestone and S. L. Leonard. *Plasma Diagnostic Techniques.* Academic Press, New York, New York, 1965.

[32] J. D. Jackson. *Classical Electrodynamics.* John Wiley and Sons, New York, Ney York, second edition, 1975.

[33] L.D. Landau and E.M. Lifshitz. *Fluid Mechanics.* Pergamon Press, London, England, 1959.

[34] J. D. Lawson. *Proc. Phys. Soc. B*, 70:6, 1957.

[35] E. P. Lee. Technical Report UCID 18302, Lawrence Livermore National Laboratory, 1980.

[36] E. P. Lee and D. M. Cox. Beam head erosion. Technical Report UCID 17929, Lawrence Livermore National Laboratory, September 1978.

[37] C. S. Liu and V. K. Tripathi. *Interaction of Electromagnetic Waves with Electron Beams and Plasmas.* World Scientific, Singapore, 1994.

[38] R. H. Lovberg and H. R. Griem. *Methods of Experimental Physics, Plasma Physics*, volume 9, part B. Academic Press, New York, U.S.A., 1971.

[39] S. A. MacLaren. *A Scaled Final Focus Experiment for Heavy Ion Fusion.* PhD thesis, University of California, Berkeley, 2000.

[40] W. M. Manheimer, M. Lampe, and J. P. Boris. Effect of a surrounding gas on magnetohydrodynamic instabilities in z pinch. *The Physics of Fluids*, 16(7):1126–1134, July 1973.

[41] Y. Maron, E. Sarid, et al. Time-dependent spectroscopic observation of the magnetic field in a high-power-diode plasma. *Physical Review A*, 39(11):5856–5862, June 1989.

[42] R. W. Moir et al. HYLIFE-II Progress Report. Technical Report UCID-21816, Lawrence Livermore National Laboratory, 1991.

[43] J.M. Neri, P.F. Ottinger, et al. Intense ion-beam transport experiements using a z-discharge plasma channel. *Physics of Fluids B*, 5(1):176–189, January 1993.

[44] D. R. Nicholson. *Introduction to Plasma Theory.* Krieger, Malabar, Florida, 1983.

[45] C. Niemann. PhD thesis, Gesellschaft für Schwerionenforschung, Darmstadt Germany, 2001.

[46] C. Niemann, D.M. Ponce, S. S. Yu, et al. Development of a faraday polarimeter for magnetic field measurements in a discharge channel for ion beam transport. *Nuclear Instruments and Methods in Physics Research A*, 2000.

[47] W. A. Noonan, T. G. Jones, and P. F. Ottinger. Laser induced fluorescence diagnostic for measuring small magnetic fields. *Review of Scientific Instruments*, 68(1):1032–1035, January 1997.

[48] J.N. Olsen. Laser-initiated channels for ion transport:CO_2 laser absorption and heating of NH_3 and C_2H_4 gases. *Journal of Applied Physics*, 52(5):3279–3285, May 1981.

[49] J.N. Olsen and L. Baker. Laser-initiated channels for ion transport:breakdown and channel evolution. *Journal of Applied Physics*, 52(5):3286–3292, May 1981.

[50] J.N. Olsen, D.J. Johnson, and R.J. Leeper. Propagation of light ions in a plasma channel. *Applied Physics Letters*, 36(10):808–810, May 1980.

[51] J.N. Olsen and R.J. Leeper. Ion beam transport in laser initiated discharge channels. *Journal of Applied Physics*, 53(5):3397–3404, May 1982.

[52] Y. I. Ostrovsky, M. M. Butusov, and G. V. Ostrovskaya. *Interferometry by Holography*. Springer-Verlag, Berlin, Germany, 1980.

[53] P. Ottinger et al. HIF-Scaled Self-Pinched Ion Beam Transport Experiments on Gamble II at NRL. DPP APS Conference, New Orleans, LA, November 1998.

[54] P. F. Ottinger, F. C. Young, S. J. Stephanakis, et al. Self-pinched transport of an intense proton beam. *Physics of Plasmas*, 7(1):346–358, January 2000.

[55] P.F. Ottinger. Final report on self-pinched transport experiments for HIF on the Gamble II pulsed power accelerator at the Naval Research Laboratory. Technical Report 6670/004:PFO:lc, Naval Research Laboratory, Washington, DC 20375, January 1999.

[56] P.F. Ottinger et al. Self-pinched transport of an intense proton beam. *Physics of Plasmas*, 7(1):346–358, January 2000.

[57] P.F. Ottinger, D. Mosher, and S.A. Goldstein. Propagation of intense ion beams in straight and tapered z-discharge plasma channels. *Physics of Fluids*, 23(5):909–920, May 1980.

[58] H. K. Park. A new asymetric abel-inversion method for plasma interferometry in tokamaks. *Plasma Physics and Controlled Fusion*, 81(13):2035–2046, July 1989.

[59] R. R. Peterson and M. E. Sawan. Pre-formed plasma channels for heavy ion transport in IFE reactors:Final report for contract #46053410. Technical report, Fusion Technology Institute, University of Wisconsin-Madison, 1997.

[60] Art Phelps. private communication.

[61] D. M. Ponce, C. Niemann, S. S. Yu, et al. Diagnostics of plasma channel for HIF transport. *Nuclear Instruments and Methods in Physics Research A*, 2000.

[62] H. M. Presby and D. Finkelstein. Plasma phasography. *Review of Scientific Instruments*, 38(11):1563–1572, November 1967.

[63] R. D. Richtmyer and K. W. Morton. *Difference Methods For Initial-Value Problems*. Interscience Publishers, New York, 1967.

[64] D. V. Rose, P. F. Ottinger, D. R. Welch, et al. Numerical simulations of self-pinched transport of intense ion beams in low pressure gases. *Physics of Plasmas*, 6(10):4094, October 1999.

[65] G.S. Sarkisov, A.S. Shikanov, et al. Structure of the magnetic fields in z-pinches. *JETP*, 81(4):743–752, October 1995.

[66] W. Sharp, T.J. Fessenden, E.P. Lee, and S.S. Yu. Numerical Models in CYCLOPS. HIF weekly physics seminar, March 1998.

[67] Y. R. Shen. *The Principles of Nonlinear Optics*. Wiley Interscience. John Wiley and Sons, New York, 1984.

[68] F.H. Shu. *The Physics of Astrophysics*, volume II. University Science Books, Mill Valley, CA, 1992.

[69] E. Stambulchik and Y. Maron. The effect of Rydberg and continuum eigenstates on the Stark effect of resonance lines of atoms and ions. Draft of the faculty of physics, Weizmann Institute, Israel.

[70] A. Sullivan. *Propagation of High-Intensity, Ultrashort Laser Pulses in Plasmas*. PhD thesis, University of California, Berkeley, 1993.

[71] A. Tauschwitz. private communication.

[72] A. Tauschwitz, S. S. Yu, S. Eylon, et al. Plasma lens focusing and plasma channel transport for heavy ion fusion. In *Proceedings Seventh International Symposium on Heavy Ion Inertial Fusion*, page 493, 1995.

[73] A. Tauschwitz, S. S. Yu, S. Eylon, et al. Plasma lens focusing and plasma channel transport for heavy ion fusion. *Fusion Engineering and Design*, 32(33):493–502, 1996.

[74] L. Tonks and I. Langmuir. *Phys. Rev.*, 33:195, 1929.

[75] K. Vandersloot. Equations in CYCLOPS. LBNL internal notes on the CYCLOPS code.

[76] J.J. Watrous and P.F. Ottinger. Final focusing of intense ion beams with radially nonuniform current density z discharges. *Physics of Fluids B*, 1(12):2470–2478, December 1989.

[77] B. Weber, E. Featherstone, et al. Electron Density Measurements During Ion Transport on Gamble II: Preliminary Results. Pulsed Power Physics Technote 98-11, Naval Research Laboratory, Washington, D.C., November 1998.

[78] B. Weber and G. Peterson. Abel inversion and error analysis for gas-puff density measurements. Pulsed Power Physics Technote 95-05, Naval Research Laboratory, Washington, D.C., March 1995.

[79] B.V. Weber and S.F. Fulghum. A high sensitivity two-color interferometer for pulsed power plasmas. *Review of Scientific Instruments*, 68(2):1227–1232, February 1997.

[80] D. R. Welch and C. L. Olson. Self-pinched transport for ion-driven inertial confinement fusion. *Fusion Engineering and Design*, 32(33):477–483, 1996.

[81] J. R. Woodworth, T. A. Green, and C. A. Frost. Ionization of organic molecules with ultraviolet lasers: A technique for generating large, well defined ionized volumenes. *Journal of Applied Physics*, 57(5):1648–1655, March 1985.

[82] S. S. Yu et al. Plasma-channel-based reactor and final transport. In *XX International Heavy Ion Fusion Simposium*, pages 174–181, 1998.

Appendix A

Review of Gas and Plasma Optical Properties

It is important to quantify the effects that the neutral gas and the plasma have on the probing electromagnetic rays. This effect depends greatly on the frequency of the incident radiation, its intensity, and its coherence.

Electromagnetic waves propagating through any medium obey the wave equation

$$\nabla^2 \vec{E} - 4\pi \nabla \rho - \frac{4\pi}{c^2} \frac{\partial \vec{J}}{\partial t} - \frac{1}{c^2} \frac{\partial^2 \vec{E}}{\partial t^2} = 0 \qquad (A.1)$$

as well as an identical version for the magnetic field. Here $\vec{E}$ is the local electric field, ρ the local charge density distribution, and $\vec{J}$ the local current density. The wave equation is derived directly from Maxwell's equations, and in the case of equation (A.1), charge distributions and currents are allowed. One seeks to solve equation (A.1) for small amplitude plane waves from which one can form general solutions combining linearly these solutions.

The typical solution is of the form

$$\vec{E}(\vec{r}, t) = \vec{E}_0 \ e^{i(\vec{k} \cdot \vec{r} - \omega t)} \tag{A.2}$$

For the especial case of wave propagation in vacuum, $\rho = \vec{J} = 0$, insertion of equation (A.2) into equation (A.1) produces the know vacuum dispersion relation

$$k^2 = \frac{\omega^2}{c^2} \tag{A.3}$$

or

$$v_{phase} = c = \frac{\omega}{k} \tag{A.4}$$

which indicates that the phase velocity of electromagnetic waves in vacuum is independent of frequency. Also a characteristic of electromagnetic waves propagating in vacuum is that of satisfying the condition $\vec{k} \cdot \vec{E} = 0$ which is a consequence of Gauss' law in the absence of a charge distribution. Transverse electromagnetic waves are the norm, even for propagation through a plasma, although less important longitudinal modes can be excited as well. These longitudinal modes will be of no concern to us [38].

When an electromagnetic wave propagates through a medium, the medium's response to the excitation is that of slowing the wave. One can define the index of refraction n of a medium as

$$n \equiv \frac{k(\omega)}{k_{vacuum}} = c \ \frac{k(\omega)}{\omega} \tag{A.5}$$

where $k(\omega)$ is the so called dispersion relation of the wave in the particular medium. The dispersion of a wave in a medium is subject to the charge and current conditions that the medium allows. This property is what makes electromagnetic waves suitable for diagnostics.

The solution of equation (A.1) for a generic plasma leads to the general dispersion relation

$$k^2(\omega) = \left(\frac{\omega}{c}\right)^2 \left[1 - \frac{\omega_p^2}{\omega^2(1 \pm \omega_c/\omega)[1 + i(\nu/\omega)]}\right] \tag{A.6}$$

where ω is the electromagnetic exciting frequency, ω_p is the plasma frequency, ω_c is the cyclotron frequency, and ν the collision frequency. Both ω_p and ω_c will be defined in the following sections. The important thing to note is the fact that the larger ω is as compared to ν and ω_c, both collisions and magnetic gyration can be neglected as far as the index of refraction is concerned.

A.1 Electromagnetic Waves in Unmagnetized Plasmas

When the magnetic field in a plasma is negligible, it is easy to solve equation (A.1) to obtain the respective dispersion relation. Namely, one has to obtain a relation for $\frac{\partial \vec{J}}{\partial t}$ and $\vec{E}$. For this, one relies on the Lorentz force equation. Since $\vec{J} = -eN_e\vec{v}_e$ and $m_e d\vec{v}_e/dt = -e\vec{E}$ we have

$$\frac{\partial \vec{J}}{\partial t} = \frac{e^2 N_e}{m_e}\vec{E} \tag{A.7}$$

where e is the electronic charge, N_e the electron number density, m_e the electron's mass, and $\vec{v}_e$ the electron's velocity.

It is implicitly assumed that the plasma ions have infinite mass. Substituting equation (A.7) into equation (A.1) and using the solution (A.2) we obtain the dispersion relation

$$k^2 = \frac{\omega^2}{c^2} - \frac{1}{c^2}\frac{4\pi N_e e^2}{m_e} \tag{A.8}$$

from which the refraction index can be computed using its definition given in equation

(A.5). The electron plasma frequency, ω_p is defined as

$$\omega_p \equiv \left(\frac{4\pi N_e e^2}{m_e} \right)^{1/2} \tag{A.9}$$

as is equally derived from the plasma oscillatory equation of motion [44].

A.2 Electromagnetic Waves in Magnetized Plasmas

When there is a strong magnetic field in the plasma, or ω is only a few times larger than ω_c, then the electromagnetic wave forces the electrons to move around the magnetic lines of force. This effect breaks the symmetry that the electromagnetic wave sees and produces two distinct dispersion relations for a propagating wave. To see this, again we have to obtain a dispersion relation from equation (A.1). For the case of a magnetized plasma, the Lorentz force equation adds the additional magnetic force term $\vec{\beta} \times \vec{B}$ where $\vec{\beta} = \vec{v}_e/c$. For the purposes of this analysis, I will select the magnetic field to be oriented in the direction of the propagating wave, e.i., $\vec{k} \parallel \vec{B}$, which is the case of interest. Using a Cartesian coordinate system with $\vec{B} = B_0 \hat{z}$, and $\vec{k} = k\hat{z}$, for linear polarization $\vec{E} = E_x \hat{x} + E_y \hat{y}$, the Lorentz force equation yields

$$\frac{dv_x}{dt} = -\frac{e}{m_e} \left[E_x + \frac{v_y}{c} B_0 \right] \tag{A.10}$$

$$\frac{dv_y}{dt} = -\frac{e}{m_e} \left[E_y - \frac{v_x}{c} B_0 \right] \tag{A.11}$$

One can de-couple the equation system (A.10) and (A.11) by defining $v_\pm = v_x \pm iv_y$ and $E_\pm = E_x \pm iE_y$. The physical significance of $E_\pm$ is that of decomposing the linearly polarized electromagnetic wave into its two opposite rotating circularly polarized components, namely E_+ and E_-. Anticipating the result of this brief analysis, we will

see that one of the circular components will advance faster through the plasma than its counterpart.

Applying these new definitions to equations (A.10) and (A.11) we obtain

$$\frac{dv_\pm}{dt} = -\frac{e}{m_e} E_\pm \pm i\omega_c v_\pm \tag{A.12}$$

where we have defined the electron cyclotron frequency ω_c as

$$\omega_c \equiv \frac{eB_0}{m_e c} \tag{A.13}$$

The solution to equation (A.12) is

$$v_\pm = -i\,\frac{e}{m_e}\,\frac{E_\pm}{(\omega \pm \omega_c)} \tag{A.14}$$

since $v_\pm = v_0 e^{i(k_\pm z - \omega t)}$ and $dv_\pm/dt = -i\omega\, v_\pm$.

Therefore we have that $\vec{J}$ becomes $J_\pm$

$$J_\pm = -eN_e v_\pm \tag{A.15}$$

The term to be substituted into (A.1) is

$$\frac{4\pi}{c^2}\frac{\partial J_\pm}{\partial t} = -i\frac{4\pi N_e e^2}{m_e c^2}\frac{\partial E_\pm/\partial t}{(\omega \pm \omega_c)} = \frac{\omega_p^2}{c^2}\left(\frac{\omega}{\omega \pm \omega_c}\right)E_\pm \tag{A.16}$$

With a solution of the form $E_\pm = E_{0\pm}e^{i(k_\pm z - \omega t)}$ one obtains the following dispersion relation

$$k_\pm = \frac{\omega}{c}\left[1 - \frac{\omega_p^2}{\omega^2(1 \pm \omega_c/\omega)}\right]^{1/2} \tag{A.17}$$

The physics to note from this result is that the magnetic field causes one of the circularly polarized components to speed up with respect to the other as shown by the possible resonant condition in equation (A.17) when $\omega = \omega_c$. This property of the index of refraction

of the magnetized plasma will be exploited to attempt to measure the plasma azimuthal magnetic field in our experiment. It is important to note also that the sense of rotation is solely determined by the orientation of the magnetic field and is independent of the sense of the vector $\vec{k}$. This can be seen by the fact that the resonant condition is governed by the gyration of the electrons about the magnetic field, hence the independence on $\vec{k}$, but the sense of gyration will switch if $\vec{B}$ is reversed. The previous equations are used in section 4.4 to derive an expression for the polarization rotation when the electromagnetic wave passes through a magnetized plasma.

When $\vec{k} \perp \vec{B}$, two cases can be distinguished: case 1, $\vec{E} \parallel \vec{B}$; and case 2, $\vec{E} \perp \vec{B}$. For case 1 it is obvious that $\vec{\beta} \times \vec{B} = 0$ and the dispersion is that of an unmagnetized plasma. For case 2, a component of $\vec{E}$ is produced along the propagation direction generating a longitudinal mode. This longitudinal mode generates an elliptical polarization in the plane generated between $\vec{k}$ and the incident $\vec{E}$ field. The incorporation of the longitudinal $\vec{E}$ represents a second order correction which one can neglect [38] [15].

A.3   Different Contributions to the Index of Refraction

The bending of light is a direct consequence of interaction between the light rays and the electrons, bound or free, contained in the medium where the light is propagating. For this one has to account for all of the contributions to the change in the index of refraction. The total index of refraction is given by:

$$n_{total} = n_{molecules} + n_{atoms} + n_{electrons} \tag{A.18}$$

where n is the corresponding index of refraction. For the particular case of our plasma channel, the electron contribution will be large compared to the atoms and molecules during the initial stages of both the pre-pulse and the main bank discharges ($\sim 8\,\mu s$) but once the discharge current dies off, significant recombination has occurred and the contribution of neutrals will be significant in the subsequent time ($\sim 20\,\mu s$).

When the degree of ionization in a plasma is high, the free electrons dominate and almost entirely determine the value of the index of refraction. The index of refraction for free electrons is given by

$$n_{electrons} = \sqrt{1 - \frac{\omega_p^2}{\omega^2}} \tag{A.19}$$

with the known relation

$$\omega_p^2 = \frac{4\pi N_e e^2}{m_e} \tag{A.20}$$

For the case when $\omega >> \omega_p$ as is the case in the interaction of most plasmas and light in the optical frequency, we can approximate equation (A.19) as:

$$n_{electrons} - 1 = -\frac{\omega_p^2}{2\omega^2} = -\frac{e^2}{m_e c^2}\frac{\lambda^2}{2\pi}N_e = -r_e \frac{\lambda^2}{2\pi}N_e \tag{A.21}$$

where this equations show the strong dependence that the refractive index has with respect to the electromagnetic driving frequency.

For a neutral gas, containing both molecules and dissociated atoms, one can write the index of refraction using the Gladstone-Dale relation [2]:

$$n - 1 = K\rho \tag{A.22}$$

where K is the Gladstone-Dale constant for a particular gas, in cm^3/gr, and ρ is the gas density in gr/cm^3. An alternative way to write the refractive index for a dilute gas is by

using the expression for the polarizability α:

$$n - 1 = 2\pi N\alpha \tag{A.23}$$

where

$$\alpha = \frac{e^2}{4\pi m_e} \sum_i \frac{f_i}{\nu_i^2 - \nu^2} \tag{A.24}$$

Here the index i runs over all the interacting electrons in the molecule or atom, f_i is the bound electron oscillator strength, ν_i the dipole resonant frequency, ν the incident external electromagnetic wave frequency, and N the number density of the atomic or molecular species. To see the dependence of the atomic refractive index with wavelength when the excitation is far from resonance, one can re-write equation (A.24) by Taylor expanding about the quantity $\lambda_i/\lambda << 1$ and combining it with equation (A.23) to obtain

$$n_{atom} - 1 \approx 2\pi N_a \left[\frac{e^2}{4\pi m_e} \frac{f_i \lambda_i^2}{c^2} \left(1 + \frac{\lambda_i^2}{\lambda^2} \right) \right] = \frac{r_e f_i \lambda_i^2}{2} \left(1 + \frac{\lambda_i^2}{\lambda^2} \right) N_a \tag{A.25}$$

where r_e is the classical electron radius and we have used the relationship $c = \nu_i \lambda_i$. One can observe that the atomic (or molecular) refractive index is quite insensitive to wavelength in the optical region, since λ_i lies in the vacuum ultraviolet-soft X ray region of the spectrum. To clarify even more, we can take the analysis one step further by multiplying and dividing by the atomic mass the right hand side of equation (A.25) and identifying the resulting coefficient with the Gladstone-Dale constant K:

$$K \equiv \frac{r_e f_i \lambda_i^2}{2A} \left(1 + \frac{\lambda_i^2}{\lambda^2} \right) \tag{A.26}$$

A comment is in order here. To obtain theoretical values to the index of refraction for a gas using equation (A.25) one would have to resort to complex models such as Hartee-Fock to establish coupling among electrons and determine the relevant oscillator strength

Species	N_I	N_2
Polarizability α in [Å^3] ($\lambda \sim 480\,\text{nm}$)	1.13	1.75
Gladstone-Dale constant K in [cm^3/gr] ($412\,\text{nm} < \lambda < 544\,\text{nm}$)	0.31	0.25

Table A.1: Values of α and K for atomic and molecular nitrogen, after Alpher [2].

values. Hence we resort to empirical values for quantitative analysis. Values of α and K for nitrogen atom and nitrogen molecule are shown in table A.1 [2].

Comparing the index of refraction of neutrals with that of free electrons, i.e. comparing equations (A.21) and (A.25), neglecting higher order terms, and setting $N_{\text{molecule}} = 2N_a$ we obtain:

$$\frac{n_{molecules} - 1}{n_{electrons} - 1} = -\frac{r_e f_i \lambda_i^2 \left(1 + \frac{\lambda_i^2}{\lambda^2}\right) N_{molecules}}{r_e \frac{\lambda^2}{2\pi} N_{electrons}} = -2\pi f_i \frac{\lambda_i^2}{\lambda^2} \frac{N_{molecules}}{N_{electrons}} \qquad (A.27)$$

for $\lambda = 632.4\,\text{nm}$ and using the values of table A.1 we obtain:

$$\frac{n_{molecules} - 1}{n_{electrons} - 1} = -(6.0 \times 10^{-2}) \frac{N_{molecules}}{N_{electrons}} \qquad (A.28)$$

Figure (A.1) shows how the index of refraction varies with number density for different wavelengths. From the figure we can infer that in order to "see" the neutral gas density variations of the order of $10^{17}\,\text{cm}^{-3}$ the detection instrument should be able to detect changes of the index of refraction on the order of 10^{-6}, hence one benefits from using short wavelengths to minimize electron contribution. On the other hand, electron density probes are best suited in the near infrared. It is also necessary to see how good are the approximations made. Figure (A.2) shows the different electron densities for which cut-off occurs for the different laser wavelengths used in these experiments. It is clear from the

Index of Refraction vs Density
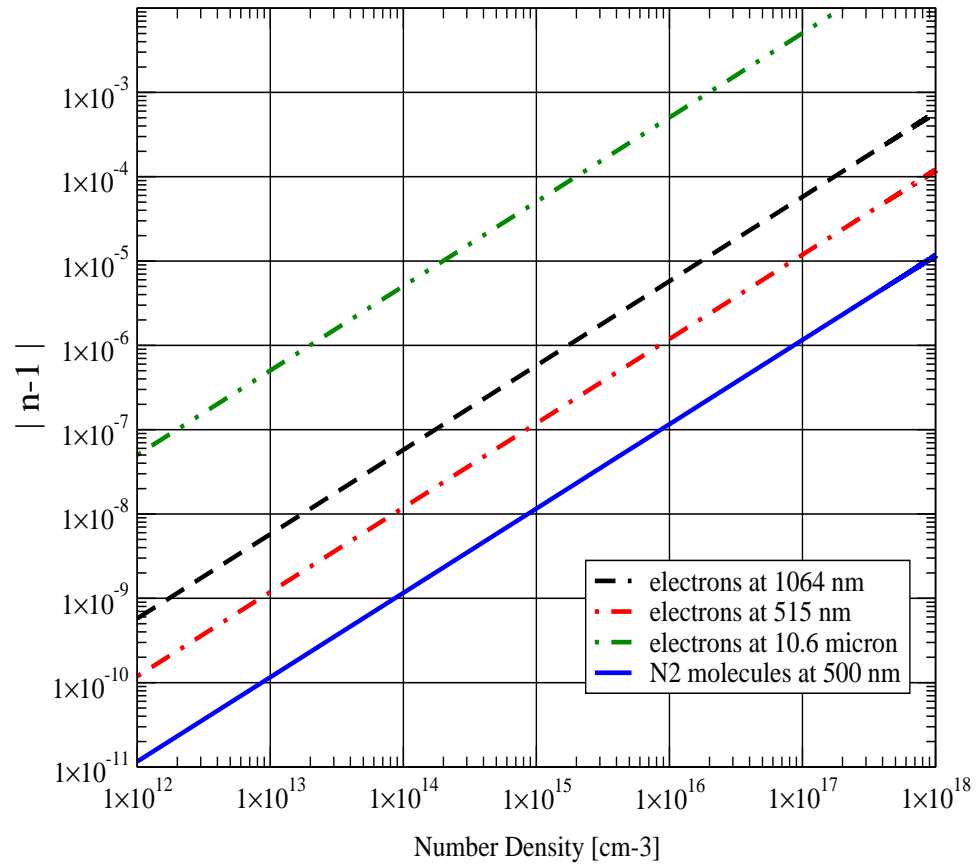
Figure A.1: Plot illustrating how the index of refraction varies as a function of number density for electrons and neutrals. Electrons are much more sensitive to wavelength as compared to neutrals. Note that the absolute value of $n - 1$ is plotted.
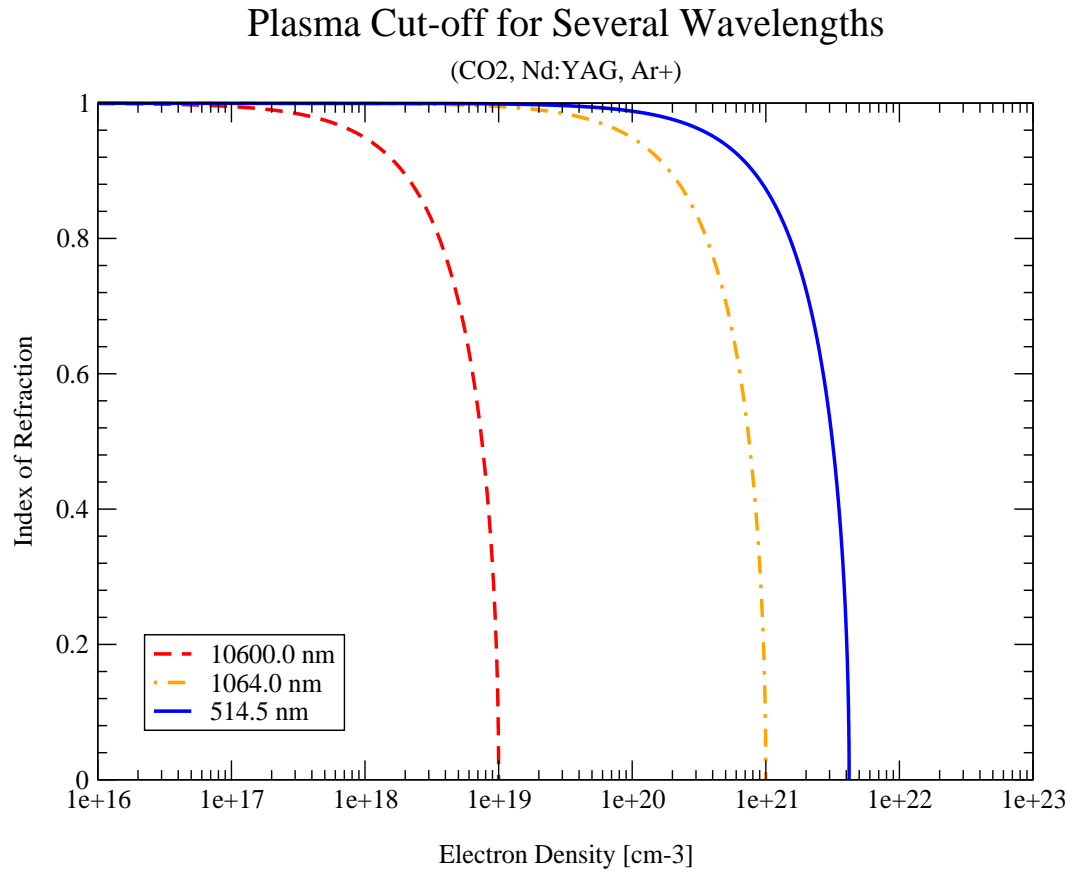
Figure A.2: Plot illustrates the cut-off density (as opposed to cut-off frequency) for the different wavelengths used as probes. The curves were calculated using equation (A.19).

figure that we are well within the linear regime, even for CO_2 laser beam wavelengths, so the previously made approximations are valid.

Appendix B

Geometrical Details of the Plasma Channel

The fact that the plasma channel has cylindrical symmetry adds a level of complication to the data analysis problem. It is advantageous to perform a coordinate transformation to address this problem.

One wishes to extract the functions $N_e(r)$ and $B(r)$, which are 3D functions with one symmetry, the azimuth. They need to be extracted from the two dimensional generated map produced by the channel diagnostics. From figure B.1, we can write down some relations that will turn out to be useful later in solving our problem. One thing to note in our particular case is that y is a *constant* while r is the *variable*. These relations form our coordiante trasformation rules.

$$\cos(\phi(r, y)) = \frac{y}{r} \tag{B.1}$$
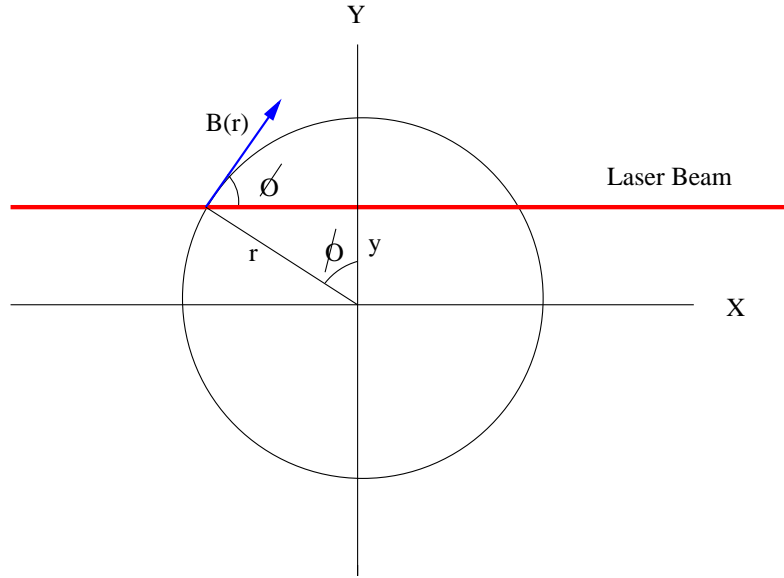
Figure B.1: Plasma channel cross section showing relevant geometry

and the rectangular to polar transformation for a constant y:

$$x = \sqrt{r^2 - y^2} \tag{B.2}$$

$$dx = \frac{r dr - y dy}{x} \tag{B.3}$$

or, since $dy = 0$

$$dx = \frac{r dr}{x} = \frac{r dr}{\sqrt{r^2 - y^2}} \tag{B.4}$$

the above transformations generated from figure B.1 are used to derive equation 4.18 from equation 4.19 and equation 4.24 from equation 4.25.

Appendix C

Abel's Equation and its Inversion

Abel's integral has the form:

$$f(x) = \int_x^\infty \frac{g(r)}{\sqrt{r^2 - x^2}} \, r dr \qquad (C.1)$$

where the function $f(x)$ is known and $g(r)$ is the function that needs to be solved for. Equation (C.1) can be solved for the function $g(r)$ with the famous inversion called abel's inversion:

$$g(r) = -\frac{1}{\pi} \int_R^\infty \frac{\frac{df(x)}{dx}}{\sqrt{x^2 - r^2}} \, dx \qquad (C.2)$$

There are many attempts and techniques to find practical solutions to specific problems where equation (C.1) appears, this dissertation being one of them. There are some practical constraints that abel's integral imposes. One, and perhaps the most notorious, is the requirement for the function $f(x)$ to be an even symmetric function. There are two immediate consequences of this imposition. One is that if $f(x)$ is odd, equation (C.2) diverges about the origin. The second consequence is that it makes the function $g(r)$ azimuthally symmetric. Algorithms and techniques have been developed when $g = g(r, \theta)$,

but discussion of this is left to the references. Therefore, solutions carried out in this work

have the assumption that the function $g(r)$ is even and cylindrically symmetric.

With this in mind, it is instructive to look at a couple of analytical examples. First

let us examine the function $f(x) = \exp(-x^2)$. Suppose that the output function from some

experiment is

$$f(x) = e^{-x^2} \tag{C.3}$$

that is generated from the line integral from an azimuthally symmetric function. Following

the geometrical argument from appendix B, we are led to

$$e^{-x^2} = \int_x^\infty \frac{g(r)}{\sqrt{r^2 - x^2}} \, r dr \tag{C.4}$$

where the domain of $f(x)$ is $\{x \mid 0 \le x < \infty\}$. Here $f(x) = e^{-x^2}$ represents half of the

mapped function.

Direct application of equation (C.2) leads to

$$g(r) = \frac{2}{\pi} \int_r^\infty \frac{x \, e^{-x^2}}{\sqrt{x^2 - r^2}} \, dx = \frac{\sqrt{\pi}}{\pi} e^{-r^2} \tag{C.5}$$

where the function $g(r) = \frac{\sqrt{\pi}}{\pi} e^{-r^2}$ is defined in the interval $\{r \mid 0 \le r < \infty\}$.

The most important thing to note from this example is the amplitude difference

between $f(x)$ and $g(x)$

$$\frac{g(0)}{f(0)} = \frac{\sqrt{\pi}}{\pi} \tag{C.6}$$

This effect can be misleading when observing experimental results solely on the basis of a

function such as $f(x)$.

The second example pertains to the situation when an experimental function can't

be cast in a closed form analytical expression. One can then resort to fitting or approximat-
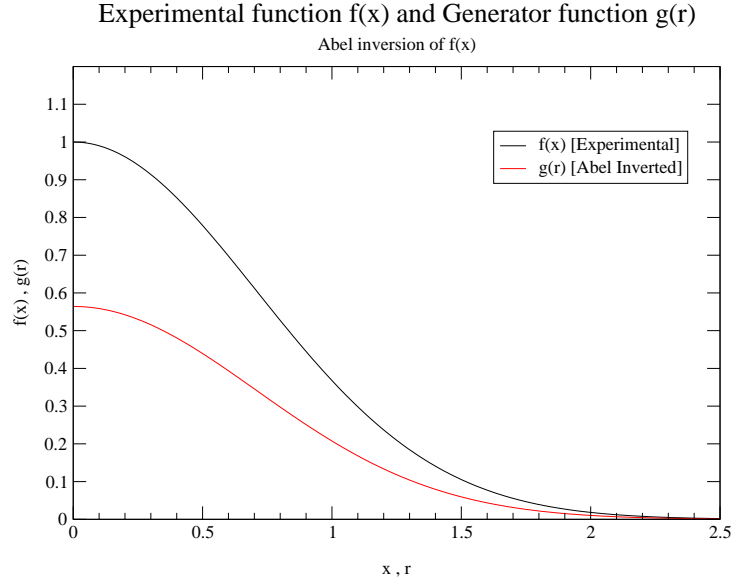
Figure C.1: Abel inversion of a Gaussian

ing the experimental function by regression techniques in terms of a power series expansion. Hence one can express $f(x)$ in terms of the the even powers of x (as the reader may recall, we assumed $f(x)$ even)

$$f(x) = a_0 + a_2 \ x^2 + a_4 \ x^4 + a_6 \ x^6 + \cdots \tag{C.7}$$

If one proceeds to invert $f(x)$, one does a term by term inversion. This leads to

$$g(r) = \frac{1}{\pi} \left\{ 2a_2 \ \sqrt{R^2 - r^2} + 4a_4 \ \left[r^2 \sqrt{R^2 - r^2} + \frac{1}{3} \left(R^2 - r^2 \right)^{3/2} \right] + \cdots \right\} \tag{C.8}$$

where the value R is determined by the condition $f(R) \approx 0$. This has to be done since now $f(x)$ is a series approximation and the term by term inversion cannot be carried out to infinity. This method provides for a more or less straight forward way to invert a rather difficult empirical function and is the technique used to deconvolve the electron density in this work. There is a technical note written by Weber of NRL on this particular subject

where he makes an analysis on the errors that this technique may introduce. He also looks at the effects and requirements of the odd power terms for a polynomial approximation [78] [79].

Appendix D

Details of CYCLOPS

These are notes adapted from Kevin Vandersloot's internal notes, with permission

[75].

D.1 Outline of Solution and Routines - ODEINT

D.1.1 DVAR

Get time derivatives; eqns. 6.1-6.4.

GET_GRID

Update grid positions and velocities.

GET_DEN

Calculate ρ, η_{g}, η_{e} .

GET_SIGMA

Calculate σ .

GET_PLASMA

Calculate T and P .

GET_AVALANCHE

Calculate α .

GET_VIS

Calculate q .

GET_DERIVS

Calculate $\frac{1}{r}\frac{\partial(rV)}{\partial r}$, $\frac{\partial P}{\partial r}$, $\frac{\partial q}{\partial r}$.

GET_THERM_COND

Calculate K_{th}, $\frac{1}{r}\frac{\partial}{\partial r}K_{\mathrm{th}}\frac{\partial T}{\partial r}$.

GET_RADIATION

Calculate $\frac{\sigma_{\mathrm{sb}}T^4}{l^1}$.

Evaluate RHS of eqns. 6.1-6.4

D.1.2 RKQS

Advance equations 6.1-6.4.

D.1.3 STEP_FIELD

Advance eqn. 6.5 with time centered implicit scheme.

GET_FIELD

Calculate J and E after update of B .

D.1.4 Iterate

D.2 DVAR

DVAR consists of calculating the right hand side of eqns 6.1-6.4 and all the necessary terms. The first routine called is UPDATE_PLASMA which is a wrapper for the routines GET_GRID, GET_DEN, GET_SIGMA, GET_PLASMA, GET_AVALANCHE, and GET_VIS.

GET_GRID updates the radial grid locations and velocities. Also calculated is the location of the grid midpoints.

GET_DEN calculates the mass density ρ and gas density η_g all of which are located on the cell midpoints. The gas density is calculated from mass conservation. For a parcel of gas the density multiplied by the volume is constant through time so $\rho(t)V(t) = \rho_0 V_0$

which leads to the following finite difference equation [1] [63]:

$$\rho_i = \rho_{0i} \frac{r^2_{0\ i+1} - r^2_{0\ i}}{r^2_{i+1} - r^2_i} \tag{D.1}$$

where the index i refers to the ith grid point. η_g is calculated from ρ and it is simply ρ divided by the mass of the ions.

GET_SIGMA calculates the conductivity using the updated value of η_e from the following equation:

$$\sigma = \frac{e^2 \eta_e}{m_e \nu_m} \tag{D.2}$$

where e is the charge of an electron, m_e is the mass of an electron, and ν_m is the momentum transfer collision frequency. ν_m is calculated in the routine GET_FREQ. For nitrogen molecules, ν_m is given by [35],

$$\nu_m = \nu_m^{[N_2]} + \nu_m^{[Benz]} \tag{D.3}$$

$$\nu_m^{[N_2]} = 2.02 \times 10^5 \ P_{eff} \ \frac{1 + 23.5 \ T_{eff}}{1 + 9.9 \text{x} 10^{-2} \ T_{eff}} \tag{D.4}$$

$$\nu_m^{[Benz]} = 10 \ \times \ 2.02 \times 10^5 \ \eta_{[Benz]} k_b T_0 \tag{D.5}$$

$$T_{eff} = S^2 + 1.55 \times 10^{-3} \ T \tag{D.6}$$

---

[1] pp. 318

$$S = \frac{E^2}{P_{\text{eff}}^2} \tag{D.7}$$

$$P_{\text{eff}} = \eta_{\text{g}} k_{\text{b}} T_0 \tag{D.8}$$

$$T_0 = 273.15 \text{ K} \tag{D.9}$$

where [Benz] refers to benzene. For neon, this is given by [2] [19],

$$\nu_{\text{m}} = 7\text{x}10^2 \ T_{\text{eff}}^{0.65} \ \frac{\rho}{\rho_0} \ \left(\frac{m^3}{s}\right) \tag{D.10}$$

with T_{eff} the same as that for N_2.

GET_PLASMA calculates the gas temperature T, and pressure P using the updated value of ϵ, the gas specific energy, The gas specific energy is given by $\epsilon = 3/2k_{\text{b}}(T/m)$ for a monoatomic gas and $\epsilon = 5/2k_{\text{b}}(T/m)$ for a diatomic gas. The pressure is then given by the ideal gas law $P = \eta_{\text{g}} k_{\text{b}} T$.

GET_AVALANCHE is next called in DVAR and calculates the avalanche coefficient α. For a nitrogen molecule, the equation is [36]

$$\alpha = \alpha^{N_2} + \alpha^{[\text{Benz}]} \tag{D.11}$$

$$\alpha^{N_2} = \frac{2.09\text{x}10^{-6} \ MAX[0, \ P_{\text{eff}} - n_{\text{e}} k_{\text{b}} T_0] \ S^3}{1 + 1.05\text{x}10^{-4} \ S + 3.46\text{x}10^{-8} \ S^2 + 4.19\text{x}10^{-14} \ S^3} \tag{D.12}$$

---

[2]pp. 3

$$\alpha^{[\text{Benz}]} = \alpha^{\text{N}_2}(P_{\text{eff}}^{[\text{Benz}]}, S^{[\text{Benz}]}) \tag{D.13}$$

$$P_{\text{eff}}^{[\text{Benz}]} = \nu_{[\text{Benz}]} k_{\text{b}} T_0 \tag{D.14}$$

$$s^{[\text{Benz}]} = 1.5 \ s \tag{D.15}$$

where P_{eff} and S are the same values used to calculate the collision frequency. The value of s is calculated in slightly different manner than that of the collision frequency to take into account avalanching due to high gas temperatures. A rough fit for a table of electron characteristic energies as a function of s is [60]

$$\epsilon_{\text{k}} = 1.6\text{x}10^-11 \ \sqrt{\frac{E}{\eta_{\text{g}}}} \tag{D.16}$$

thus $s \propto (E/\eta_{\text{g}})^2 \propto \epsilon^4$. S is then calculated in two manners. The first is to calculate it using E/η_{g} and the second is to calculate it by plugging in the gas energy for the electron characteristic energy. The maximum of the two is then used. For neon, the avalanche coefficient is given by [3] [19]

$$\alpha = \frac{5.165 \ \left(\frac{\rho}{\rho_0}\right) S^3}{1 + 1.5\text{x}10^{-4} \ S + 4.67\text{x}10^{-6} \ S^2 + 6.99\text{x}10^{-12} \ S^3} \tag{D.17}$$

GET_VIS calculates the artificial viscosity given by [4] [63]

---

[3] pp. 3
[4] pp. 313

$$q_i = \begin{cases} 2a^2 \rho_i (V_{i+1} - V_i)^2 & \text{if } V_{i+1} - V_i < 0 \\ \\ 0 & \text{otherwise} \end{cases} \qquad \text{(D.18)}$$

where V is the grid velocity here.

The thermal conduction coefficient K_{th} is next calculated in the routine

GET_THERM_COND. For nitrogen molecule a rough fit is given by [5] [12]

$$q_i = \begin{cases} 4.53\text{x}10^{-8} \ T^2 & \text{if } T \ < \ 8000 \text{ K} \\ \\ 3.37\text{x}10^{-8} \ (T - 15000)^2 + 1.25 & \text{if } T \ > \ 8000 \text{ K} \end{cases} \qquad \text{(D.19)}$$

Finally, the radiation term of equation 6.3 is calculated in the routine

GET_RADIATION. The plank mean length is roughly fitted from a plot as a function of

gas density and temperature. The fit for nitrogen molecule is [6] [12]

$$l^1 = \frac{0.02 \ e^{\left(\frac{1}{1.34\text{x}10^{-4} \ T}\right)}}{\rho} \qquad \text{(D.20)}$$

D.3   STEP_PLASMA

The algorithm for solving equations 6.1 - 6.4 is a fifth order variable step size

Runge-Kutta integrator. It is the algorithm that is presented in *Numerical Recipes* by

Press *et al* . However, the algorithm differs in that the dependent variable is a multi-

dimensional array of the dependent variables of equations 6.1 - 6.4. See *Numerical Recipes*

for a description of the algorithm beginning on page 708.

---

[5]pp. 14
[6]pp. 27

D.4 STEP_FIELD

STEP_FIELD integrates the magnetic diffusion equation 6.5 one time step dt. Starting with Maxwell's equations with no free charges, no displacement current, and Ohm's law

$$\nabla \cdot \vec{E} = 0 \tag{D.21}$$

$$\nabla \times \vec{E} = -\frac{\partial \vec{B}}{\partial t} \tag{D.22}$$

$$\nabla \times \vec{B} = \mu_0 \vec{J} \tag{D.23}$$

$$\vec{J} = \sigma \vec{E} \tag{D.24}$$

gives

$$\nabla \times \left(\frac{\nabla \times \vec{B}}{\sigma}\right) = \nabla \times (\mu_0 \vec{E}) = -\mu_0 \frac{\partial \vec{B}}{\partial t} \tag{D.25}$$

In cylindrical coordinates with $\vec{B}$ having only a $\hat{\theta}$ component we have that

$$\nabla \times \vec{B} = \frac{1}{r} \frac{\partial (r B_\theta)}{\partial r} \tag{D.26}$$

thus

$$\nabla \times \left(\frac{\nabla \times \vec{B}}{\sigma}\right) = -\frac{\partial}{\partial r} \left(\frac{1}{r\sigma} \frac{\partial (r B_\theta)}{\partial r}\right) \tag{D.27}$$

so, combining these two gives

$$\mu_0 \frac{\partial B_\theta}{\partial t} = -\frac{\partial}{\partial r}\left(\frac{1}{r\sigma}\frac{\partial(rB_\theta)}{\partial r}\right) \tag{D.28}$$

Since the code is Lagrangian, the partial derivative of a quantity is related to the total derivative by the following, in the case of the magnetic field $\vec{B}$

$$\frac{d\vec{B}}{dt} = \frac{\partial\vec{B}}{\partial t} + \left(\vec{V}\cdot\nabla\right)\vec{B} \tag{D.29}$$

from which follows equation 6.5

$$\frac{dB_\theta}{dt} = \frac{1}{\mu_0}\frac{\partial}{\partial r}\left(\frac{1}{r\sigma}\frac{\partial(rB_\theta)}{\partial r}\right) - B_\theta\frac{\partial V}{\partial r} \tag{D.30}$$

The algorithm to solve this equation is a first order time-centered implicit scheme. Equation 6.5 is then evaluated at the half time step in which dB/dt becomes

$$B_i^{n+\frac{1}{2}} = \frac{B_i^{n+1} + B_i^n}{2} \tag{D.31}$$

Note that this is not exact in that the radial position of the ith element is changing with time so that B_i^{n+1} is located at a different position than B_i^n thus the value of B at the half time step ignores the change in radial position. Now, equation 6.5 becomes

$$\mu_0 \frac{dB_i^{n+\frac{1}{2}}}{dt} = \frac{\partial}{\partial r_i}\frac{1}{r_i\sigma_i}\left(\frac{\partial\left(rB^{n+\frac{1}{2}}\right)}{\partial r}\right)_i - B_i^{n+\frac{1}{2}}\left(\frac{\partial V}{\partial r}\right)_i \tag{D.32}$$

To first order, the derivative of rB_θ with respect to r is given by

$$\left(\frac{\partial\left(rB^{n+\frac{1}{2}}\right)}{\partial r}\right)_i = \frac{r_{i+1}B_{i+1}^{n+\frac{1}{2}} - r_i B_i^{n+\frac{1}{2}}}{r_{i+1} - r_i} = \frac{r_{i+1}B_{i+1}^{n+\frac{1}{2}} - r_i B_i^{n+\frac{1}{2}}}{\Delta r_i} \tag{D.33}$$

This partial derivative is then located at the grid midpoints. Denoting the left side of D.33 by $\partial r B_i$, the first term of the right hand side of equation D.32 becomes

$$\frac{\partial}{\partial r_i}\left[\frac{1}{r_i\sigma_i}\left(\frac{\partial\left(rB^{n+\frac{1}{2}}\right)}{\partial r}\right)_i\right] = \left[\frac{\left(\frac{\partial(rB_i)}{r_{mi}\sigma_i} - \frac{\partial(rB_{i-1})}{r_{mi-1}\sigma_{i-1}}\right)}{r_{mi} - r_{mi-1}}\right] \tag{D.34}$$

where r_{mi} is the location of the ith grid midpoint. Note that this is not exactly centered in that the derivative is to be evaluated on the grid points but the right hand side of equation D.34 is centered on the midpoint of the grid midpoints. To first order, the second term of equation D.32 is

$$B_i^{n+\frac{1}{2}}\frac{\partial V}{\partial r_i} = B_i^{n+\frac{1}{2}}\frac{V_{i+1} - V_i}{r_{i+1} - r_i} \tag{D.35}$$

Using these difference equations gives a tridiagonal equation for the new B^{n+1} values in terms of the old B^n values. The tridiagonal equation is solved in the routine TRISOLVE.

Boundary conditions are needed at the edge of the cell and on the axis. B_θ is zero on axis. The external circuit determines the boundary condition for the value of B at the outer edge of the cell. The external circuit equation is given by

$$\frac{Q_{\text{ext}}}{C_{\text{ext}}} + L_{\text{ext}}\frac{dI}{dt} + R_{\text{ext}}I + V_{\text{cell}} = 0 \tag{D.36}$$

$$V_{\text{cell}} = l_{\text{cell}}E(r_{\text{max}}) \tag{D.37}$$

with Q_{ext} the charge on the external capacitor, C_{ext} the external capacitance, L_{ext} the external inductance, I the current, R_{ext} the external resistance, V_{cell} the voltage across

the cell, and l_{cell} the length of the cell. This equation is evaluated at the half time step also and the circuit variables are set in terms of the magnetic field. By Ampere's law, $I = (2\pi/\mu_0)R_{\text{cell}}B(r_{\max})$ and with $I = dQ/dt$ the following equations result

$$\dot{I}^{n+\frac{1}{2}} = 2\pi R_{\text{cell}}\frac{B_{\text{I}}^{n+1} - B_{\text{I}}^{n}}{dt} \tag{D.38}$$

$$Q_{\text{ext}}^{n+\frac{1}{2}} = Q_{\text{ext}}^{n} + \frac{1}{2}\left(I^{n+1} + I^{n}\right)dt = Q_{\text{ext}}^{n} \tag{D.39}$$

$$E\left(R_{\text{cell}}\right)^{n+\frac{1}{2}} = \frac{J\left(R_{\text{cell}}\right)^{n+\frac{1}{2}}}{\sigma\left(R_{\text{cell}}\right)} \tag{D.40}$$

$$= \frac{1}{r_{\max}\sigma(r_{\max})}\frac{\partial\left(rB^{n+\frac{1}{2}}\right)}{\partial r} \tag{D.41}$$

$$= \frac{1}{R_{\text{cell}}\sigma(R_{\text{cell}})}\frac{R_{\text{cell}}B^{n+\frac{1}{2}}_{\text{I}} - r_{\text{I}-1}B_{\text{I}-1}^{n+\frac{1}{2}}}{R_{\text{cell}} - r_{\text{I}-1}} \tag{D.42}$$

where here the index I refers to the quantity evaluated at R_{cell}. The circuit equation thus gives the value of B^{n+1} at the outer radius and the next to outer grid point $(r_{\text{I}-1})$ in terms of the old values B^{n} along with the charge on the capacitor at time $t_n(Q_{\text{ext}}^{n})$ to be solved by the tridiagonal solver. The initial charge across the capacitor is specified by the initial voltage across the capacitor.

Once the tridiagonal equation is solved and the values for B at $t+dt$ are obtained the circuit quantities are updated and J and E are calculated. The circuit quantities are updated as such

$$Q^{n+1} = Q^{n} + I^{n+\frac{1}{2}}dt = Q^{n} + \frac{1}{2}\frac{2\pi R_{\text{cell}}}{\mu_0}\left(B_{rmI}^{n+1} + B_{\text{I}}^{n}\right) \tag{D.43}$$

$$I^{n+1} = \frac{2\pi R_{\text{cell}}}{\mu_0} B_{\text{I}}^{n+1} \tag{D.44}$$

J and E are calculated in the routine GET_FIELD and are both located at the grid midpoints. Equations D.22 and D.23 are used. J and E are first evaluated at the half time step since both σ and r are previously updated to the half time step in STEP_PLASMA. The current density is

$$J_i = \frac{1}{\mu_0} \; \nabla \times \vec{B} = \frac{1}{\mu_0 r_{mi}} \; \frac{r_{i+1} B_{i+1}^{n+\frac{1}{2}} - r_i B_i^{n+\frac{1}{2}}}{r_{i+1} - r_i} \tag{D.45}$$

The electric field is calculated as such

$$-\frac{\partial B}{\partial r} = \nabla \times \vec{E} = -\frac{\partial E}{\partial r} \tag{D.46}$$

$$\Rightarrow \; E = \int \frac{\partial B}{\partial r} dr \tag{D.47}$$

$$\Rightarrow \; E_i = E_1 + \sum_{j=2}^{i} \left(\frac{\partial B^{n+\frac{1}{2}}}{\partial r} \right)_j (r_{mj} - r_{mj-1}) \tag{D.48}$$

where the derivative of B is calculated in the same fashion as when setting up the tridiagonal equations. E_1 is the value of E at the first midpoint (between $r = 0$ and r_1) and is just J_1/σ_1. J and E are extrapolated to the full time step using the old values from the previous half time step so

$$E_i^{n+1} = E_i^{n+\frac{1}{2}} + \frac{1}{2} \left(E_i^{n+\frac{1}{2}} - E_i^{n-\frac{1}{2}} \right) \tag{D.49}$$

where the $1/2$ is replaced by 1 the first time step since E is then known at $t = 0$ and at the half time step $t = dt/2$ and J is calculated in a similar fashion.

Das Ende.

Ω